Max-Planck Institut für Kolloid and Grenzflächenforschung

Nonaqueous Syntheses of Metal Oxide and Metal Nitride Nanoparticles

Dissertation

zur Erlangung des akademischen Grades
“doctor rerum naturalium”
(Dr. rer. nat.)
in der Wissenschaftsdisziplin “Kolloidchemie”

eingereicht an der
Mathematisch-Naturwissenschaftlichen Fakultät
Universität Potsdam

von
Jelena Buha

Potsdam, im Januar 2008

Elektronisch veröffentlicht auf dem
Publikationsserver der Universität Potsdam:
http://opus.kobv.de/ubp/volltexte/2008/1836/
urn:nbn:de:kobv:517-opus-18368
[http://nbn-resolving.de/urn:nbn:de:kobv:517-opus-18368]

С’ вером у Бога

Abstract

Nanostructured materials are materials consisting of nanoparticulate building blocks on the scale of nanometers (i.e. 10^{-9} m). Composition, crystallinity and morphology can enhance or even induce new properties of the materials, which are desirable for todays and future technological applications. In this work, we have shown new strategies to synthesise metal oxide and metal nitride nanomaterials.

The first part of the work deals with the study of nonaqueous synthesis of metal oxide nanoparticles. We succeeded in the synthesis of In_2O_3 nanopartcles where we could clearly influence the morphology by varying the type of the precursors and the solvents; of ZnO mesocrystals by using acetonitrile as a solvent; of transition metal oxides (Nb_2O_5, Ta_2O_5 and HfO_2) that are particularly hard to obtain on the nanoscale and other technologically important materials.

Solvothermal synthesis however is not restricted to formation of oxide materials only. In the second part we show examples of nonaqueous, solvothermal reactions of metal nitrides, but the main focus lies on the investigation of the influence of different morphologies of metal oxide precursors on the formation of the metal nitride nanoparticles. In spite of various reports, the number and variety of nanocrystalline metal nitrides is marginally small by comparison to metal oxides; hence preformed metal oxides as precursors for the preparation of metal nitrides are a logical choice. By reacting oxide nanoparticles with cyanamide, urea or melamine, at temperatures of 800 to 900 °C under nitrogen flow metal nitrides could be obtained. We studied in detail the influence of the starting material and realized that size, crystallinity, type of nitrogen source and temperature play the most important role. We have managed to propose and verify a dissolution-recrystallisation model as the formation mechanism. Furthermore we could show that the initial morphology of the oxides could be retained when ammonia flow was used instead.

Table of Contents

1 Introduction

Nanoscience and nanotechnology encompass a range of techniques rather than a single discipline, and stretch across the whole spectrum of science, touching medicine, physics, engineering and chemistry. The prefix "nano" originates from the Greek word for dwarf, and thus refers to something small. As a prefix for a unit of time or length, it means one billionth of that unit. Thus, a nanometer (nm) is 10^{-9} meter. Many water molecules can easily occupy a sphere 1 nm in diameter; the DNA double helix is approximately 2 nm wide; a single human hair is around 80,000 nanometres in width; the dot over this letter "i" is approximately one million nanometers in diameter.[1]

One of the main objectives of nanochemistry is the development of general pathways towards synthesis of nanoparticles or, being only a few nm in size in all three dimensions, quantum dots.[2] Additionally the control over particle size and shape is of great interest with regard to specific applications of these materials as nanodevices. The synthesis approach must fulfill good yields and high crystallinity as the main requirements.

Although noble metal nanoparticles have been used by Roman glassmakers already in the fourth century A. D. to fabricate colored glasses,[3] and their scientific investigation is started by Faraday,[4] the synthesis of nanoparticles has not experienced tremendous development until the last decades. Metal oxides constitute an especially important class of materials and their unique characteristics are making them the most diverse class of materials, with properties covering almost all aspects of materials science and solid state physics.[5] In particular, metal oxides are used in the fabrication of microelectronic circuits, sensors, piezoelectric devices, fuel cells,

coatings for the passivation of surfaces against corrosion, and as catalysts. On the other hand, since the discovery of spinel nitrides in 1999 there has been a lot of effort towards further development of advanced nitrides and electronic nitrides. Metal nitrides are expected to show interesting optoelectronic properties, leading to application in light-emitting diodes (based on nitrides of Group III elements) and because of the combination of wide band gap and high melting temperature as components in short-wavelength optoelectronic devices such as blue light emitting diodes; because of their high thermal stability and hardness, applications in cutting tools are suggested; low thermal expansion and electric conductivity are proposing eventual use in turbocharger rotors, valves, turbine wheels, fuel elements for nuclear reactors, tool materials in machining; good wettability and adhesion are making them good refractory coatings.[6]

There has been an explosive growth of nanoscience and nanotechnology in the last decade, primarily because of the availability of new methods of synthesizing nanomaterials, as well as tools for characterization and manipulation.[7] For the synthesis of nanoscale materials, two basic approaches are available. The first, so called *Top-down* approach, is more physical and engineering approach, trying to reduce size of structures with improved techniques such as particle-, ion-, electron-beam or scanning-probe-based lithography today being able to manufacture materials at the 50 nm-level.[8] Most results originate from the downscaling of lithographic techniques in semiconductor research. On the other hand, the *Bottom-up* approach, influenced by (bio)chemical principles, involves assembly of atomic or molecular units to molecular structures ranging from atomic dimensions present in nature, utilizing noncovalent molecular interactions, up to supramolecular structures. Even though bottom-up techniques are having their disadvantages, since beside size and structure, control over direction and position is required, recently a movement away from top-down techniques towards bottom-up strategies was observed within the international research community.[9]

Nowadays, a variety of methods is known to generate metal oxide and metal nitride nanoparticles with a reasonable control of the particle size. Physical strategies include gas/vapor condensation, spray pyrolysis, and thermochemical methods, also referred to as chemical vapor deposition. Chemical methods, on the other hand, offer

potential routes to obtain better materials in terms of chemical homogeneity (especially for mixed oxides) and morphological control. There is variety of methods available to synthesize both organic and inorganic nanoparticles. Liquid-phase techniques, including coprecipitation from both aqueous and nonaqueous solutions, followed by the thermal decomposition of the products towards oxide formation, simultaneously occurring with nucleation, growth, coarsening and unavoidable agglomeration process and little chance of the particles being monodispersed. For the researchers involved in these reported synthesis of metal oxides, monodispersity was neither a requirement nor a priority. Besides that, sol-gel chemistry, microemulsion, hydrothermal-solvothermal processing, templating and biomimetic synthesis are opening access to many others still not completely examined and developed methods.

The research on the sol-gel synthesis of metal oxide nanoparticles was long focused on aqueous techniques, where the precursor is hydrolyzed. In an initiation step, the metal alkoxide or metal halide is hydrolyzed and M-OH specie is generated according to:

$$\equiv M\text{–}OR + H_2O \longrightarrow \equiv M\text{–}OH + ROH \qquad (1.1)$$

or

$$\equiv M\text{–}Cl + H_2O \longrightarrow \equiv M\text{–}OH + HCl \qquad (1.2)$$

After hydroxy groups' formation, they react with each other or with other metal alkoxide/chalide and a 3D M-O-M network is formed. This propagation occurs through a polycondensation process.[10] Oxygen bridges form through the elimination of H_2O, ROH or HCl:

$$\equiv M\text{–}OH + \equiv M\text{–}OX \longrightarrow \equiv M\text{–}O\text{–}M\equiv + XOH \qquad (1.3,\ X = H \text{ or } R)$$

or

$$\equiv M\text{–}OH + \equiv M\text{–}Cl \longrightarrow \equiv M\text{–}O\text{–}M\equiv + HCl \qquad (1.4)$$

The mechanism is rather simple as shown above, but aqueous synthesis techniques have several disadvantages, which basically all result from the high reactivity of the precursor towards hydrolysis.[11] Usually, the resulting products are amorphous and

need to be crystallized in a subsequent calcination treatment which coincidentally changes the particle morphology, usually by particle growth. For the production of ternary metal oxides, the large differences in hydrolysis rates of different precursors can lead to undesirable inhomogeneities in the products.[12] Moreover, the synthesis conditions, such as temperature, method of mixing, pH and especially the nature and concentration of anions need to be controlled precisely to achieve the desired products and reproducibility.[13]

Therefore, several strategies have been developed to achieve a more controlled synthesis. The metal precursor can be modified by stable ligands such as acetate or acetylacetonate, thereby decreasing its reactivity.[14]-[15] On the other hand, chemical or physical processes can be utilized to promote the slow, controlled hydrolysis of alkoxide precursors. Another possibility as the alternative and complete avoidance of water in the reaction medium at the same time is the nonaqueous synthesis of metal oxides. First reports on the formation of silica in the absence of water were already published in the 1950s, when Gerrard et al. studied the reaction of various alcohols with silicon tetrachloride.[16] Many years later, Vioux et al. started systematic studies on the nonaqueous formation of monolithic silica[17] and metal oxide gels[18] by reacting the metal halides with alcohols, ethers or metal alkoxides, leading to metal-oxygen-metal bonds termed as *alkyl halide elimination*:

$$\equiv M\text{–}Cl + ROX \longrightarrow \equiv M\text{–}OR + XCl \qquad (1.5,\ X = H \text{ or } R)$$

and/or

$$\equiv M\text{–}OR + \equiv M\text{–}Cl \longrightarrow \equiv M\text{–}O\text{–}M\equiv + RCl \qquad (1.6)$$

In past ten year this process was getting more and more popular. Instead of water, organic solvents such as ketones, aldehydes or amines are used as liquid phase reactants, and variety of chemicals such as organometallic complexes or metal alkoxides, halides and acetylacetonates as precursors. The main advantages of such processes is better control over size and shape because of the possibility of combinations and well understood organic reaction processes, high crystallinity at relatively moderate temperatures, homogeneity of the obtained particles, robust synthesis parameters and ability to control the crystal growth without the use of the

surfactants. The reaction mechanism is more complex than for aqueous sol-gel chemistry, and a lot of studies are still going on.[19]

Aqueous or non-aqueous solution chemistry has proven to be a powerful tool to produce nanoparticles and nanomaterials with finely tuned morphological, compositional and structural characteristics. Control of size, shape, surface and assembly properties of nanoscale materials are fundamental steps towards their study in fundamental research and their implementation in technological devices. In spite of the immense progress in nanoparticle research, the reported synthesis strategies are often isolated efforts without offering any underlying physical or chemical principles that would allow either the generalization of the processes involved for any kind of nanomaterial or the development of a mechanistic understanding of nanoparticle formation. The development of expeditious and inexpensive production routes to metal oxide and nitride nanoparticles is of high importance for many reasons. Powders consisting of nano sized particles are highly suitable for the fabrication of thin films, which are needed e.g. for applications in electronics with the advantage of enhanced sintering properties. Alongside the general trend to further miniaturization of functional devices in emerging technologies such as energy storage, pigmentation, sensing, and conversion demands for the production of materials in particle sizes already approaching the lower nanoscale.[20]

This work is focused on chemical methods that make it possible to tune the particle size and/or morphology on the nanoscale. Special attention is being given to works combining original syntheses and characterization of synthesized materials. Due to their rich chemistry and the variety of possible applications, metal oxides are the key -but not exclusive- materials of the work, they are complimented with metal nitride materials. All metal oxides presented herein are synthesized via nonaqueous sol-gel chemistry, and once more is proved that their morphology is highly influenced by precursors as well as by organic media used. One can see that size of the particles could be tuned by varying some of many possible combinations. In some of the synthesis benzyl alcohol was used as solvent, as it has been found to be a versatile medium allowing the synthesis of high-purity metal oxides.[21] In the others, acetonitrile was used, as it was not the case so far, proving once more the generality of this approach. To avoid the formation of hydrochalogenic acids which would

constitute a potential hazard and rule out the work in a glove box, to obtain higher purity of the final materials, to have less reactive and easier to handle materials, in most of the procedures alkoxides and acetylacetonates were used. However, due to their lower reactivity as in case when solvents with low boiling points were used, the reaction could not be performed under ambient pressure and had to be carried out in a sealed autoclave, i.e. under solvothermal conditions. In recent years, the concepts embodied in hydrothermal process have been extrapolated to nonaqueous system, therefore, its counterpart so-called “solvothermal process” emerges, in which organic solvents were used as reaction media instead of water as reaction media.[22] The syntheses are performed in this way because of several reasons:

- Technological interest in the design of solid-state phases with tailor-made properties at moderate temperatures, including solubilization of inorganic starting materials,
- Conventional hydrothermal method is confined under conditions that some reactants will decompose in the existence of water, or there are precursors very sensitive to water as reaction media, resulting in the failure in synthesis of the desired compounds,
- Process is simple and easy to control with several changeable parameters such as solvents, temperature and reaction time,
- Sealed system prevents the contamination in case of the hazardous side products and air sensitive precursors,
- Polar and non-polar solvents can be widely extended to prepare various kinds of non-oxide crystalline materials whose precursors are sensitive to water etc.

Besides metal oxides, metal nitride nanoparticles were investigated, with an emphasis on the ones gained via thermal transformation of metal oxides, synthesized via nonaqueous sol-gel chemistry, transformed under N_2 flow and using cyanamide, urea and melamine as nitrogen sources. Apart from aforementioned, some attempts of applying nonaquoeous sol-gel chemistry approach towards synthesis of metal nitride nanoparticles is shown, where unfortunately no pure nitride was observed. There is also small part in Chapter 4 where transformation of In_2O_3 into InN under ammonia flow is presented in order to transform the morphology of the starting material which was not the case when nitrogen sources and N_2 flow were used.

References

[1] http://www.royalsoc.ac.uk/landing.asp?id=1210.

[2] W. J. Parak, L. Manna, F. C. Simmel, D. Gerion, A. P. Alivisatos, *in: Nanoparticles: From Theory to Application (Ed.: G. Schmid)* **2004**, Wiley.

[3] C. P. Poole Jr., F. J. Owens, **2003**, *Introduction to Nanotechnology*, J. Wiley & Sons.

[4] M. Faraday, *Philos. Trans. Roy. Soc. London* **1857**, *147*, 145.

[5] C. N. R. Rao, B. Raveau, *Transition metal oxides* **1995**, *New York*, VCH Publishers.

[6] N. B. Dahotre, P. Kadolkar, S. Shah, *Surf. Interface Anal.* **2001**, *31*, 659.

[7] C. N. R. Rao, A. K. Cheetham, *J. Mater. Chem.* **2001**, *11*, 2887.

[8] U. S. Schubert, D. Wouters, *Angew. Chem. Int. Ed.* **2004**, *43*, 2480.

[9] J. M. Taylor, *"New Dimensions for Manufacturing - A UK Strategy for Nanotechnology"* **2002**, Report for the UK Advisory Group for Nanotechnology Applications.

[10] J. N. Hay, H. M. Raval, *J. Mater. Chem.* **1998**, *8*, 1233.

[11] E. Matijevic, *Chem. Mater.* **1993**, *5*, 412.

[12] S. Doeuff, M. Henry, C. Sanchez, F. Babonneau, *J. Non-Cryst. Solids* **1987**, *89*, 206.

[13] J. C. Debsikdar, *J. Non-Cryst. Solids* **1986**, *86*, 231.

[14] M. Jansen, E. Guenther, *Chem. Mater.* **1995**, *7*, 2110.

[15] M. Ivanda, S. Music, S. Popovic, M. Gotic, *J. Mol. Struct.* **1999**, *481*, 645.

[16] R. J. P. Corriu, D. Leclercq, P. Lefevre, P. H. Mutin, A. Vioux, *J. Non-Cryst. Solids* **1992**, *146*, 301.

[17] A. Vioux, *Chem. Mater.* **1997**, *9*, 2292.

[18] J. N. Hay, H. M. Raval, *J. Sol-Gel Sci. Tech.* **1998**, *13*, 109.

[19] M. Niederberger, G. Garnweitner, *Chem.--Eur. J.* **2006**, *12*, 7282.

[20] M. Fernández-García, A. Martínez-Arias, J. C. Hanson, J. A. Rodriguez, *Chem. Rev.* **2004**, *104*, 4063.

[21] M. Niederberger, M. H. Bartl, G. D. Stucky, *J. Am. Chem. Soc.* **2002**, *124*, 13642.

[22] S.-H. Yu, *Journal of the Ceramic Society of Japan* **2001**, *109*, S65.

2 Analysis and Characterization

2.1 Methods

2.1.1 Wide Angle X-ray Scattering (WAXS)

Crystalline materials consist of a periodic arrangement of repeating units of atoms in space. The simplest portion of the structure is defined as the unit cell. The basic unit cell is a parallelepiped made of side lengths and angles as defined in Figure 2.1. The angles and lengths used to define the geometry and the size of the unit cell are known as the unit cell parameters (lattice parameters), whereas the shape of the unit cells is described by the lattice symmetry. Depending on the symmetry of the unit cell, which is in turn defined by lattice parameters, seven crystal systems are identified. These are isometric (cubic), hexagonal, rhombohedric (trigonal), tetragonal, orthorhombic, monoclinic and triclinic. These crystal systems are further sub-divided into thirty-two crystal classes depending on the position of atoms in the space. Repeating unit cells form a crystal lattice in which each atom represents a lattice point. Planes or set of planes parallel to each other can be drawn using the lattice points. These planes are labeled using Miller indices, *h, k* and *l*, which are integers given by the reciprocals of the fractional intercepts along each of the cell directions.[1]

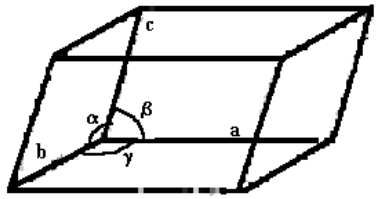

Figure 2.1 Schematic unit cell

X-rays are defined as short-wavelength electromagnetic radiation produced by the deceleration of high-energy electrons or by electronic transitions involving electrons in the inner orbitals of atoms. The X-rays are produced in a vacuum X-ray tube that contains essentially two electrodes: an anode commonly made of copper, and a

cathode, usually a tungsten filament, as electron source. The cathode is heated to emit electrons and when a high voltage is applied between the electrodes, streams of electrons (cathode rays) are accelerated from the cathode to the anode and induce the emission of X-ray radiation from the anode. When X-ray interacts with electrons of an atom, they act as secondary source and emit X-rays of the same frequency. This phenomenon is called as Thomson scattering (In physics, **Thomson scattering** is the scattering of electromagnetic radiation by a charged particle. The electric and magnetic components of the incident wave accelerate the particle. As it accelerates, it in turn emits radiation and thus, the wave is scattered. Thomson scattering is an important phenomenon in plasma physics and was first explained by the physicist J.J. Thomson). The extent of scattering depends on the number of electrons possessed by the atom. The emitted wave travels in all the directions as a spherical wave front. If there are two or more sources in vicinity, the secondary waves interfere with each other to give increase or decrease in intensity due to constructive or destructive interference respectively, depending on the phase difference at the point of interference. If the secondary sources are periodically arranged, the interference between the secondary waves gives high intensity due constructive interferences only at certain angles while, at other angles, destructive interference leads to the loss of intensity.

Bragg's approach was to consider the crystals as being built in layers, or planes, such that each acts as a semi-transparent mirror. The planes allow some of the X-ray beams to be reflected at the same angle as the angle of incidence (Figure 2.2).

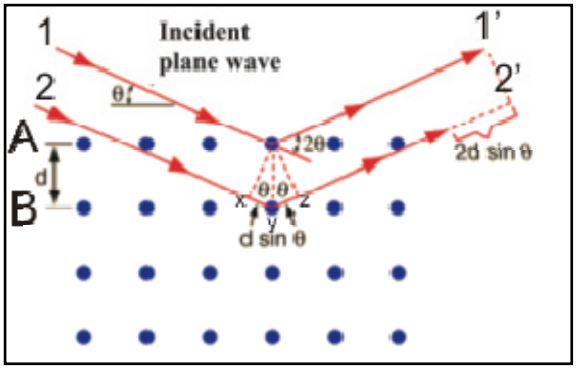

Figure 2.2 Schematic diagram for determining Bragg's Law.

Planes A and B reflect the incident beams 1 and 2 to form beams 1' and 2'. The condition under which these beams are in phase with each other is approached as follows. Beam 2 2', shown in Figure 2.2, has to travel a further distance, xyz, as compared to beam 1 1'. For 1'and 2' to be in phase with each other, xyz must equal

n, where *n* is an integer determined by the order given. The perpendicular spacing, *d*, and angle of incidence, *θ*, called the Bragg angle, are related by:

$$xy = yz = d \sin\theta$$
$$\Rightarrow \quad xyz = 2\, d \sin\theta$$
$$\text{Since} \quad xyz = n\lambda$$
$$\Rightarrow \quad n\lambda = 2\, d \sin\theta \qquad (2.1)$$

When Bragg's Law (2.1) is satisfied, the reflected beams are in phase and thus constructively interfere. If the angle is not correct then destructive interferences will occur. It can be observed that many solutions are possible, i.e., *n* = 1,2,3, which result in peaks of higher order. An ideal inorganic crystal is constructed by the infinite repetition of identical structural units in space. In the simplest crystals, the structural unit is a single atom, such as in copper, silver or gold, but usually the smallest structural unit comprises many atoms or molecules.[2] For the investigation of crystal structures by X-ray diffaction, Bragg's law is the most basic and important principle (Fig. 2.2). Positive interference only occurs if the phase shift of the two rays is a multiple of λ. As the phase shift calculates *2 d sin θ* (determined by simple geometry), the Bragg equation[3] is: $n\lambda = 2\, d \sin\theta$.

2.1.1.1 The Powder X-ray Diffraction Method

The basic principle of the powder method is shown in Figure 2.3. A monochromatic beam of X-rays strikes a powdered sample made of randomly assembled crystallites such that every orientation is possible. As a result, there are some crystals correctly oriented at the Bragg angle for every diffraction plane and hence some diffraction occurs.

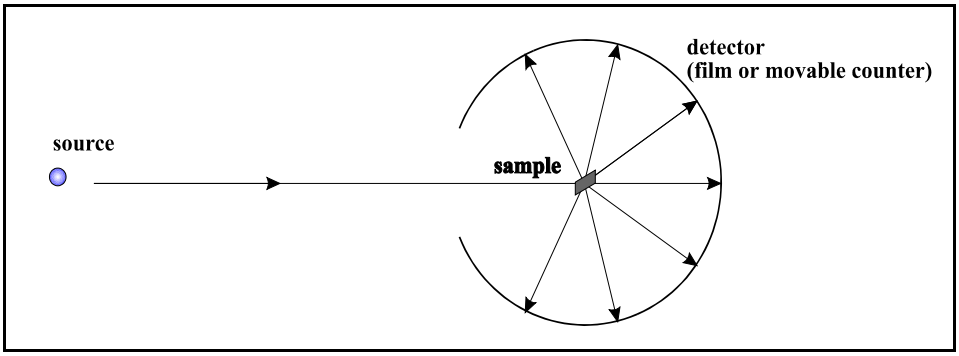

Figure 2.3 Schematic representation of the powder method.

The diffracted beam can be detected by one of the two means, a photographic plate surrounding the sample, or a movable detector, connected to a computer. The original photographic method, called the Debye-Scherrer method, is not used so much in modern X-ray diffraction practices. An actual diffractometer can accurately collect data about the position and the intensity. This enables the determination of the phase composition of a crystalline sample in less than an hour, with the recorded pattern being matched against standard patterns.

The collection of X-ray powder diffraction data is routinely carried out on a diffractometer, such as shown in Figure 2.4:

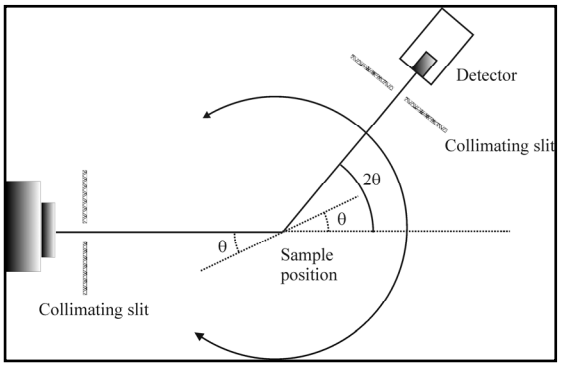

Figure 2.4 Schematic representation of a standard X-ray diffractometer.

The X-rays are generated in an X-ray tube, where electrons bombard a metal target, which is usually copper. This bombardment results in the emission of X-rays. The X-rays are then collimated into a pencil like beam. The beam then goes through the sample, which is rotating around a central axis, and is diffracted. This diffracted beam is then passed through a further set of collimation slits to remove X-ray scattering. The X-rays are then counted in a detector moving around the central axis at an angle of rotation twice that of the sample.

2.1.1.2 Distinctive Aspects of Nanoparticles' Diffraction

The very small grain size of clusters in nanophase materials gives their diffraction pattern sometimes the appearance of an amorphous material, but of course they are not. The difficulty in determining their structure by X-ray diffraction, however, is imposed at a fundamental level by two features of these systems: the small size of structural domains that characterize the diffraction pattern; and the occurrence of highly symmetric, but non-crystalline structures. In short, the common assumption that there exists some kind of underlying long-range order in the system under study does not always apply to nanophase materials. Size-dependent and structure-

specific features in diffraction patterns can be quite striking in nanometer-sized particles. Small particles have fairly distinct diffraction patterns, both as a function of size and as a function of structure type. In general, regardless of structure, there is a steady evolution in the aspect of diffraction profiles: as particles become larger, abrupt changes do not occur, features grow continuously from the diffraction profile and more detail is resolved. These observations form the basis for a direct technique of diffraction pattern analysis that can be used to obtain structural information from experimental diffraction data.

Single crystal nanoparticles exhibit features in diffraction that are size-dependent, including slight shifts in the position of Bragg peaks, anomalous peak heights and widths.[4] Figure 2.5 shows the diffraction patterns for three sizes of face-centered-cubic (fcc) particles, spanning a diameter range of 1.6 ± 2.8 nm, and containing from 147 to 561 atoms. The intensities have been normalized, so that the first maximum in each profile has the same height, and shifted vertically, so that the features of each can be clearly seen. Also shown are the positions of the bulk (Bragg) diffraction lines for gold, indexed at the top.

It should be immediately apparent from Figure 2.5 that there is considerable overlap in the peaks of the particle profiles. In fact, the familiar concept of a diffraction peak begins to loose meaning when considering diffraction from such small particles. This actually has several important consequences, which have been known for some time:[4]

- not all peaks associated with a particular structure are resolved in small crystalline particles,
- those peaks that are resolved may have maxima that do not align with expected bulk peak positions,
- peak shapes, peak intensities and peak widths may differ from extrapolated bulk estimates,
- few minima in intensity between peaks actually reach zero,
- small, size-related, features appear in the diffraction pattern.

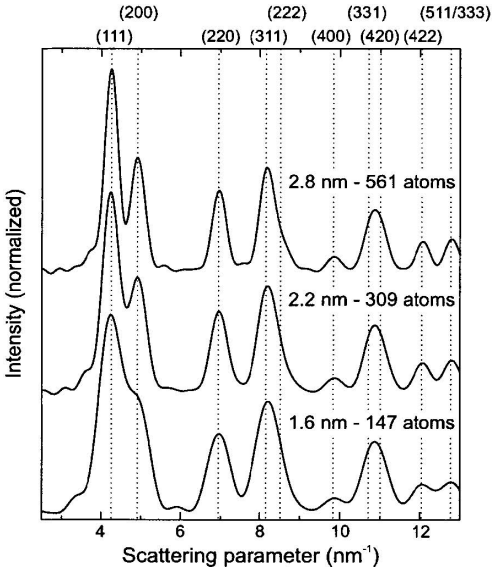

Figure 2.5 Calculated diffraction pattern of three successive sizes of cuboctahedral (fcc) particles. The intensities of the main (111) peak have been normalized to the same value for display, in reality their intensity increases rapidly with size. The baselines of the profiles have also been shifted vertically. At the top of the figure the indices for the Bragg diffraction peaks are shown. The number of atoms per model and the approximate diameters are inset.

Clearly, to extract quantitative information based on size-limited bulk structure formulae is complicated. It means, for example, that an apparent lattice contraction, or expansion, due to a single peak shift may be size related. Also, the familiar Scherrer formula,[5] relating particle-size to peak-width, will be difficult to apply accurately.

2.1.2 Transmission Electron Microscopy

Electron Microscopes were developed due to the limitations of light microscopes and they use a beam of highly energetic electrons to examine objects on a very fine scale. One of the typical characters of nanophase materials is the small particle size. Although some structural features can be revealed by X-ray and neutron diffraction, direct imaging of nanoparticles is only possible using transmission electron microscopy (TEM) and scanning probe microscopy. TEM is unique because it can provide a real space image on the atom distribution in the nanocrystal and on its surface.[6] Today's TEM is a versatile tool that provides not only atomic-resolution lattice images, but also chemical information at a spatial resolution of 1 nm or better, allowing direct identification of the chemistry of a single nanocrystal. With a finely focused electron probe, the structural characteristics of a single nanoparticle can be fully characterized.

2.1.2.1 Basics about the Transmission Electron Microscope

Resolving limit of a microscope is the minimum detectable distance, Δ*x* between two points, so that they are recognized as separate objects. In 1900 E. Abbe showed that the wavelength of electromagnetic radiation (λ), the angle of the incident beam with the objective (α) and the refractive index of the medium (*n*) between the objective and the sample are related to the resolution limit as shown in the following equation:

$$\Delta x = \frac{\lambda}{n \sin \alpha} \tag{2.2}$$

The refractive index of the used medium is generally below 2 and the maximum value for sinα= 1. So the maximum resolution that a microscope can achieve by using visible light (λ_{vis} > 400 nm) is around 200 nm. Therefore, in order to achieve a better resolution, radiation sources with a smaller wavelength must be used.

Around 1930 in Berlin, E. Ruska developed the electron microscope based on de Broglie's principle of wave-particle duality. It states that associated with every particle there is a wave, wavelength of which is given by the:

$$\lambda = \frac{h}{mv} \tag{2.3}$$

h = Planck's constant

m = rest mass of the particle. In the case of electrons $m_e = 9.109 \times 10^{-31}$ kg

v = velocity of the particle

The speed of electron *v*, accelerated by an electric field U is given as:

$$\frac{1}{2} m_e v^2 = eU \qquad v = \sqrt{\frac{2eU}{m_e}} \tag{2.4}$$

e = charge on electron = 1.602×10^{-19} C

For an acceleration voltage of *U* = 100 kV, the wavelength of the electrons is estimated to 0.0037 nm. Accordingly, the theoretical resolution of electron microscopes is of three orders of magnitude higher than that of light microscopes. Considering the fact that electrons can get scattered by any particle in their way, electron microscopes are operated at high vacuum.

A TEM is composed of an illumination system, a specimen stage, an objective lens system, the magnification system, the data recording system, and the chemical analysis system. The electron gun consists of heated cathode, used as electron source and produces a stream of monochromatic electrons. Electrons are produced either by thermoionic emission using a heated filament (e.g., LaB_6) or in a field emission gun from a fine tungsten tip, and are accelerated towards an anode.[7] Field emission source is unique for performing high coherence lattice imaging, electron holography and high spatial resolution microanalysis.

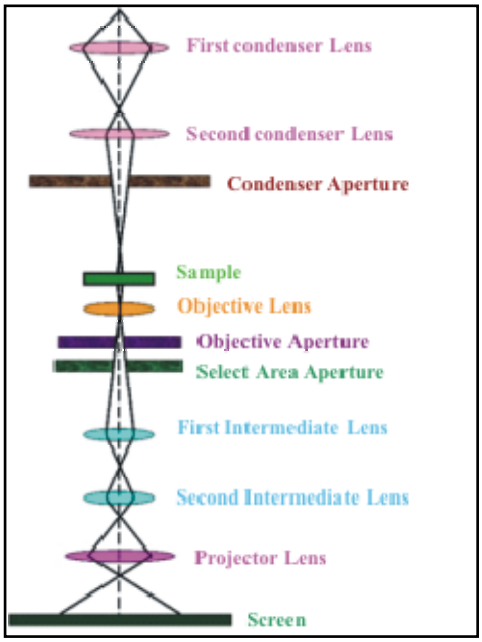

Figure 2.6 Schematic description of TEM imaging and selected area diffraction pattern processing set-up.

As shown in the Figure 2.6 the illumination system also includes the condenser lenses that are vitally important for forming a fine electron probe. The resulting beam is focused to a small, thin, coherent beam by the use of them and strikes the specimen. Specimen stage is a key for carrying out structure analysis, because it can be used to perform *in-situ* observations of phenomena induced by annealing, electric field, or mechanical stress, giving the possibility to characterize the physical properties of individual nanostructures. The electrons may undergo several kinds of interaction with the solid material, namely absorption, diffraction, and elastic or inelastic scattering. Scattering processes result from interaction of the electrons with nuclei of the sample. Heavy elements therefore lead to higher scattering, which results in fewer electrons reaching the image plate. Hence, sample regions containing these elements appear dark. Conversely, areas only containing light elements, such as in organic compounds, result in limited scattering of electrons and appear bright. The objective lens is the heart of a TEM, which determines the limit of image resolution. The transmitted portion of the beam is focused by the objective lens into an image. Optional objective and selected area metal apertures can restrict the beam; the objective aperture enhancing contrast by blocking out high-angle diffracted electrons, the selected area aperture enabling the

examination of the periodic diffraction of electrons by ordered arrangements of atoms in the sample. The electron beam then passes further magnetic lenses for magnification and finally hits a fluorescent screen coated with CdS and ZnS. The resulting irradiation is recorded by a CCD camera. The magnification system consists of intermediate lenses and projection lenses, and it gives a magnification up to 1.5 million. The data recording system tends to be digital with the use of a charge coupled device (CCD), allowing quantitative data processing and quantification. Finally, the chemical analysis system is the energy dispersive x-ray spectroscopy (EDX) and electron energy-loss spectroscopy (EELS), both can be used complimentary to quantify the chemical composition of the specimen. EELS can also provide information about the electronic structure of the specimen.

2.1.2.2 High-Resolution TEM Lattice Imaging

Image formation

An explanation of the mechanism by which the microscope image is formed is based on the necessity for the light rays diffracted by the specimen to be collected by the objective and allowed to contribute to the image; if these diffracted rays are not included, the fine details which give rise to them cannot be resolved.

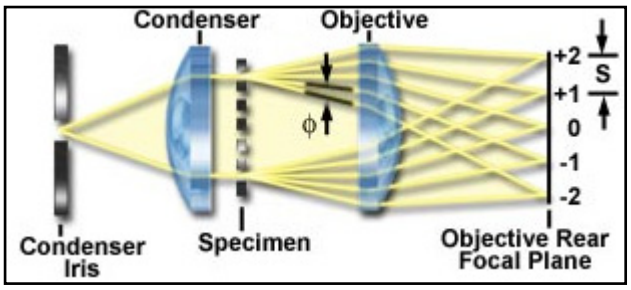

Figure 2.7 Abbe´s theory of image formation.

Ernst Abbe demonstrated that if a grating is employed for a specimen and its conoscopic image is examined at the rear aperture of the objective lens with the condenser aperture closed to a minimum, an orderly series of images of the condenser iris opening is observed. These images are arranged in a row at right angles to the periodic line grating. For gratings with broad spacings, several condenser iris images appear within the aperture of the objective lens, perhaps overlapping each other depending on the side of the iris diaphragm opening. Gratings having narrowing spacings display a greater degree of separation between the iris diaphragm images, and fewer become visible. Thus, there is a reciprocal relationship

between the line spacings in the specimen and the separation of the conoscopic image at the aperture plane. What is actually observed is the diffraction pattern from the specimen, or the image of the condenser iris diffracted by the periodic spacing of the line grating.

Figure 2.7 illustrates a schematic drawing of a microscope optical system consisting of a condenser iris diaphragm, condenser, and objective with a periodic grating representing the specimen. The periodic specimen diffracts a collimated beam (arising from each point of the condenser aperture), giving rise to first-order, second-order, and higher order diffracted rays on both sides of the undeviated zeroth-order beam. The diffracted rays occur by constructive interference at a specific angle (Φ). Each diffracted-order ray (including the zeroth) is focused at the rear focal plane of the objective. The period (s) between the focused diffraction orders is proportional to the numerical aperture of the ray entering the objective. The situation is governed by the equation**:**

$$s/f \cong \lambda/d = \sin(\Phi) \tag{2.5}$$

Where f is the focal length of the aberration-free objective that fulfills the sine condition, λ is the wavelength of light in the specimen plane, and Φ is the angle between the lens axis and the diffracted wave.

The most surprising fact about Abbe's experiments is that when the first-order diffraction pattern is masked at the objective rear aperture, so that only the zero- and second-order diffraction patterns are transmitted, the image of the specimen appears with twice the spatial frequency**,** or with only half the spacing between the lines. In the absence of what is really the first-order diffraction pattern, the image is now generated by interference between the zero- and second-order diffraction patterns, the latter of which is masquerading as the first-order pattern. The observation proves that the waves making up the diffraction pattern at the aperture plane converge and interfere with each other in the image plane and generate the orthoscopic image.

In order to explain the image formation with the mathematical background, once more a simplified illustration of a TEM[8] to a single lens microscope is given in Figure 2.8, in which only a single objective lens is considered for imaging and the intermediate lenses and projection lenses are omitted. This is because the resolution

of the TEM is mainly determined by the objective lens. The entrance surface of a thin foil specimen is illuminated by a parallel or nearly parallel electron beam. The electron beam is diffracted by the lattices of the crystal, forming the diffracted beams, which are propagating along different directions. The electron-specimen interaction results in phase and amplitude changes in the electron wave that are determined by quantum mechanical diffraction theory. For a thin specimen and high-energy electrons, the transmitted wave function $\psi(x, y)$ at the exit face of the specimen can be assumed to be composed of a forward-scattered wave. The diffracted beams will be focused in the back-focal plane, where an objective aperture could be applied. An ideal thin lens brings the parallel-transmitted waves to a focus on the axis in the back focal plane.

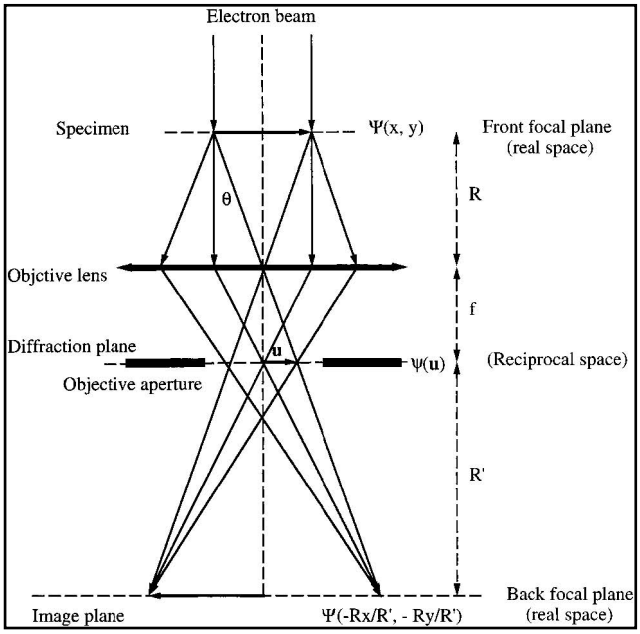

Figure 2.8 Abbe´s theory of image formation in a one-lens transmission electron microscope. This theory is for a general optical system in TEM (for a lens to produce a true image, it must be large enough to transmit the entire diffraction pattern of the object).

Waves leaving the specimen in the same direction (or angle θ with the optic axis) are brought together at a point on the back focal plane, forming a diffraction pattern. The electrons scattered to angle θ experience a phase shift introduced by the chromatic and spherical aberrations of the lens, and this phase shift is a function of the scattering angle, thus, the diffraction amplitude at the back-focal plane is modified by:

$$\psi'(u) = \psi(u) \exp[i\chi(u)] \quad (2.6)$$

where $\psi(u)$ is the Fourier transform of the wave $\psi(r)$ at the exit face of the specimen, u is the reciprocal space vector that is related to the scattering angle by $u = 2 \sin\theta / \lambda$, and $\chi(u)$ is determined by the spherical abberation coefficient C_s of the objective lens and the lens defocus Δf[9] as shown in:

$$\chi(u) = \pi/2\, C_s \lambda^3 u^4 - \pi\, \Delta f\, \lambda\, u^2 \quad (2.7)$$

where λ is the electron wavelength. The aberration and defocus of the lens is to modulate the phases of the Bragg beams distributed in reciprocal space.

The electron image is the interference result of the beams scattered to different angles, and this interference pattern is affected by the phase modulation introduced by the aberration of the objective lens. The image is calculated according to

$$I(x,y) = |\psi(r) \otimes t_{obj}(x,y)|^2 \quad (2.8)$$

where $\otimes$ indicates a convolution calculation of (x, y), $t_{obj}(x,y)$ is the inverse Fourier transform of the phase function $exp[i\chi(u)]$.

Contrast mechanisms

Three types of contrast usually dominate images in TEM. First, diffraction contrast,[10] which is produced due to a local distortion in the orientation of the crystal (by dislocations, for example), so that the diffracted intensity of the incident electron beam is perturbed, leading to contrast observed in bright-field image. The nanocrystals oriented with their low-index zone-axis parallel or nearly parallel to the incident beam direction usually exhibit dark contrast in the bright field image, that is formed by selecting the central transmitted beam. Since the diffraction intensities of the Bragg reflected beams are strongly related to the crystal orientations, this type of image is ideally suited for imaging defects and dislocations. For nanocrystals, most of the grains are defect-free in volume, while a high density of defects are localized at the surface or grain boundary, diffraction contrast can be useful for capturing strain distribution in nanocrystals whose sizes are larger than 15 nm. For smaller size nanocrystals, since the resolution of diffraction contrast is in the order of 1 ± 2 nm, its application is limited.

Secondly, phase contrast is produced by the phase modulation of the incident electron wave when transmitting through a crystal potential.[6] This type of contrast is sensitive to the atom distribution in the specimen and it is the basis of high-resolution TEM. To illustrate the physics of phase contrast, we consider the modulation of a crystal potential to the electron wavelength. From the de Broglie relation (equation 2.3), the wavelength λ of an electron is related to its momentum $p = mv$. When the electron goes through a crystal potential field, its kinetic energy is perturbed by the variation of the potential field, resulting in a phase shift with respect to the electron

wave that travels in a space free of potential field. This is known to be the phase object approximation (POA), in which the crystal acts as a phase grating filter. If the incident beam travels along a low-index zone-axis, the variation of the thickness-projected potential of a crystal across atom rows is a sharp function because an atom can be approximated by a narrow potential well and its width is in the order of 0.2-0.3Å. This sharp phase variation is the basis of phase contrast, the fundamental of atomic-resolution imaging in TEM.

Finally, mass-thickness or atomic number produces contrast. Atoms with different atomic numbers exhibit different powers of scattering. If the image is formed by collecting the electrons scattered to high-angles, the image contrast would be sensitive to the average atomic number along the beam direction. This type of imaging is usually performed in STEM.

2.1.3 Scanning Electron Microscopy (SEM)

The schematic presentation of a SEM set-up can be seen in Figure 2.8. Scanning electron microscope generates a beam of electrons in a vacuum. That beam is collimated by electromagnetic condensor lenses, focussed by an objective lens, and scanned across the surface of the sample by electromagnetic deflection coils. The secodary electrons are released from the sample.

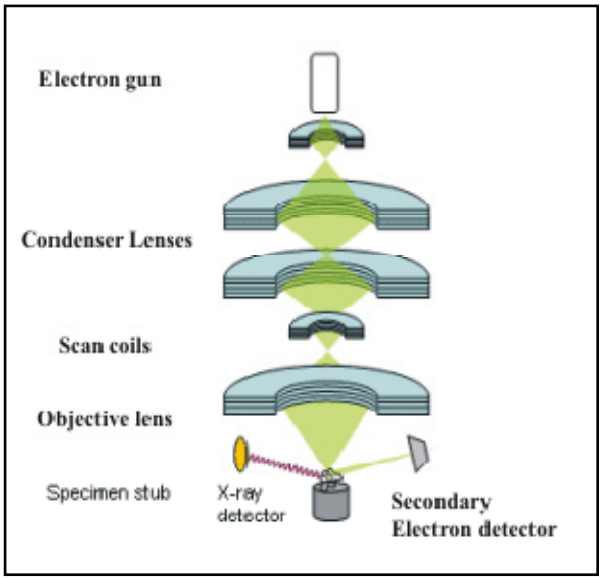

Figure 2.8 Schematic description of SEM set-up.

The secondary electrons are selectively attracted towards to detector through a grid held at a low positive potential with respect to the specimen. The electron detector counts the number of secondary electrons that arrive per unit time and translates this count rate into an electrical signal. The final image is built up from the information on the number of electrons collected from each point. The number of secondary electrons reaching the detector depends upon surface topology. Based on

geometrical considerations, secondary electrons generated at the edges and at convex surfaces have higher probability to escape from surface and reach the detector, while secondary electrons from shallow surfaces have the least probability to escape from surface and reach the detector. The area from where more secondary electrons are collected appears brighter, while the area giving a low secondary electron count appears dark. Through this contrast mechanism, a magnified image of the sample with topological details of the sample surface can be obtained. There should be a significant amount of secondary electrons generated from the sample surface in order to get good contrast in the image. During the bombardment of the sample with electrons, charge is built on the surface and in case of a non-conducting sample, it can not be dissipated. As a result of this, the image appears bright throughout the sample. To avoid charge effects in case of a non-conducting sample, suputtering of the sample with a very thin layer of metals such as gold or gold/palladium alloy is a part of sample preparation.

2.2 Characterization

2.2.1 Powder X-ray Diffraction (XRD) Measurements

An Enraf-Nonius PDS-120 powder diffractometer in reflection mode, using an FR-590 generator as the source of Cu Kα radiation was used for wide angle X-ray (WAXS) measurements. A Nonius CPS-120 curved position sensitive detector, showing a resolution of 2θ = 0.018°, was employed to record the scattered radiation. Alternatively, the X-ray powder diffraction (XRD) diagrams of the samples were measured in *θ–θ* reflection mode (CuK_α radiation) on a Bruker D8 diffractometer equipped with a scintillation counter. XRD patterns were obtained by step scanning with a step size of 0.01º.

2.2.2 Transmission Electron Microscopy (TEM)

TEM images of samples were obtained by using a Zeiss EM-912 Omega instrument operating at acceleration voltage of 100 kV. For powders the samples were dispersed in a suitable solvent and a drop of this suspension was laid on the carbon-coated copper grid. The solvent was allowed to evaporate to form a thin layer of sample on the copper grid (400 mesh).

2.2.3 High-Resolution Transmission Electron Microscopy (HRTEM)

A CM200FEG (Philips) microscope, operated at 200kV, equipped with a field emission gun was used for high-resolution transmission electron microscopy (HRTEM) and selected area electron diffraction (SAED) and energy dispersive x-ray spectroscopy (EDX).

2.2.4 Scanning Electron Microscopy (SEM)

A Gemini Leo-1550 instrument was used for obtaining SEM images of the samples. The samples were loaded on carbon-coated stubs and sputter coated with Au/Pd alloy prior to analysis.

2.2.5 Elemental Analysis (EA)

Elemental analyses were carried out on a Vario EL Elementar (Elementar Analysensysteme, Germany) in order to quantify the carbon, hydrogen, nitrogen and sulfur contents in our sample.

2.3 References

[1] H. P. a. A. Klug, *X-ray Diffraction Procedures for Polycrystalline and Amorphous Materials*, Wiley Interscience, New York, **1974**.

[2] C. Kittel, *Introduction to Solid State Physics*, J. Wiley & Sons, New York, **1986**.

[3] W. L. Bragg, *Nature* **1912**, *90*, 410.

[4] C. W. B. Grigson, E. Barton, *Brit. J. Appl. Phys* **1967**, *18*, 175.

[5] A. Guinier, *X-ray diffraction in crystals, imperfect crystals, and amorphous bodies*, Dover, New York, **1994**.

[6] P. Buseck, J. M. Cowley, L. Eyring, *High Resolution Transmission Electron Microscopy and Associated Techniques*, Oxford University Press, New York, London, Amsterdam, **1988**.

[7] L. Reimer, *Scaning Electron Microscopy*, Springer Verlag, Berlin, **1985**.

[8] J. M. Cowley, *Diffraction Physics*, Elsvier Science B.V., New York, London, Amsterdam, **1995**.

[9] Z. L. Wang, Z. C. Kang, *Functional and Smart Materials - Structural Evolution and Structure Analysis, Vol. Chap 6*, Plenum Press, New York, **1998**.

[10] P. B. Hirsch, A. Howie, R. B. Nicholson, D. W. Pashley, M. J. Whelan, *Electron Microscopy of Thin Crystals*, Roberts E. Krieger Publishing Company, New York, **1977**.

3 Nonaqueous Syntheses of Metal Oxide Nanoparticles

3.1 Introduction

Compared to the traditional synthesis of bulk metal oxides involving the direct reaction of powder mixtures at high temperatures, sol-gel routes provide advantages such as access to metastable materials, superior compositional homogeneity, and control over particle size and shape during the chemical transformation of the molecular precursors to the final oxidic network.[1, 2] In addition to the well-known aqueous sol-gel chemistry, which was highly successful in the synthesis of bulk metal oxides,[3] in the last few years nonaqueous or non-hydrolytic processes have proven to be particularly effective for the preparation of oxidic nanoparticles.[4-6] The advantages of nonaqueous sol-gel processes in organic solvents, typically without the addition of water, are closely related to the manifold role of the organic components in the synthesis mixture. On the one hand, they supply the oxygen for the metal oxide and influence particle size, shape, and surface properties. On the other hand, the slow reaction rates in combination with the stabilizing effect of the organic species yields products that are in many cases characterized by uniform particle morphologies, high crystallinity and small crystallite sizes.[7]

Nowadays nonaqueous synthesis approaches are being employed as valuable alternatives to aqueous systems. And the family of metal oxide nanoparticles synthesized by nonhydrolytic reaction routes is rapidly growing.[8] Several nonaqueous methods have been reported leading to nanocrystalline binary metal oxides, especially titania,[9-13] zirconia,[14] and iron oxide.[15-17] Some of these procedures can be straightforwardly scaled-up to yield tens of gram quantities.[18]

More advanced processes make use of solvents which act as reactant as well as control agent for particle growth, and thus, allow the synthesis of high-purity nanomaterials. In this work, the synthesis of binary metal oxide nanoparticles is studied in order to investigate the influence of various solvents on different precursors, enabling control over the size and shape (In_2O_3 is shown as a case study). In most cases, benzyl alcohol is used as solvent, as it has been found to be a versatile medium allowing the synthesis of high-purity nanocrystalline metal oxides.[19, 20] Herein we, report a continuation of this work, by reacting metal chlorides with benzyl alcohol, which makes this simple approach even more general and applicable towards the synthesis of three important metal oxides that are particularly hard to obtain on the nanoscale via soft-chemistry routes, namely Nb_2O_5, Ta_2O_5 and HfO_2. In addition to metal halides, also metal alkoxides and acetylacetonates were used as precursors, as they possess significant advantages over metal halides, leading to higher purity of the final materials. Moreover, the formation of hydrochloric or hydrobromic acid is avoided, which constitutes a potential hazard and rule out the necessity to work in an ultra-pure, closed environment, such as in a glove box. Also, alkoxides and acetylacetonates are usually less reactive, facilitating handling and storage. Due to their lower reactivity, the synthesis must be performed under solvothermal conditions. The solvothermal method is a powerful route for preparing nanomaterials. It is similar to the hydrothermal method except that organic solvents are used instead of water.[21] The reaction mixture is transferred into a vessel which is sealed and heated in an oven, thereby leading to pressure buildup. Even though this autogenous pressure was calculated to be minute in the most cases, analogous treatments in open vessels do not result in nanocrystalline species. Additionally, an oxygen-free solvent (acetonitrile) and ”solid” solvents (benzamide and benzoylacetone) were employed to produce In_2O_3, ZnO and TiO_2 nanoparticles, proving once again the generality and flexibility in the nonaqueous synthesis approach.

3.2 Synthesis of Indium Oxide as a Case Study for the Dependence of Particle Morphology on Precursors and Solvents

3.2.1 Introduction

Cubic indium oxide is a promising candidate for gas sensing applications[22] and it is found that nanoscale indium oxide shows superior sensing properties.[23, 24] For many applications, particle size might be considered the most important parameter, because it has a tremendous effect on the mechanical, electronic, magnetic, and optical properties and thus, plays a fundamental role in determining the performance of a material. Although size control is one of the major challenges in nanoparticle synthesis, general principles are not available and examples where the size of nanoparticles can be tailored within the same reaction system are scarce. One of the most prominent example is the control of the size of iron oxide nanoparticles in the range of 6 to 13 nm in one-nanometer steps.[25] The synthesis of anatase nanoparticles involving the reaction between titanium tetrachloride and benzyl alcohol allows good control of particle size by adjusting the temperature and/or the precursor-to-solvent ratio.[20] Here we present a study on the influence of particle precursor and solvent on the size of nanocrystalline indium oxide particles.

3.2.2 Experimental

All experiments were started in the glovebox (O_2 and H_2O < 0.1 ppm). 0.68 mmol of the precursor [0.2 g indium(III) isopropoxide or 0.28 g indium(III) acetylacetonate] were added to 10 ml solvent, the reaction mixture transferred into a Teflon cup of 45 ml inner volume and slid into a steel autoclave. After heating in a furnace at 200 °C for 2 days, the precipitate was centrifuged off, washed with ethanol and dried at 80 °C. We investigated the following reaction systems: (i)indium(III) isopropoxide in benzyl alcohol, (ii) indium(III) isopropoxide in acetophenone, (iii) indium(III) acetylacetonate in 2-butanone, (iv) indium(III) acetylacetonate in acetophenone and (v) indium(III) acetylacetonate in benzylamine.

3.2.3 Results and Discussion

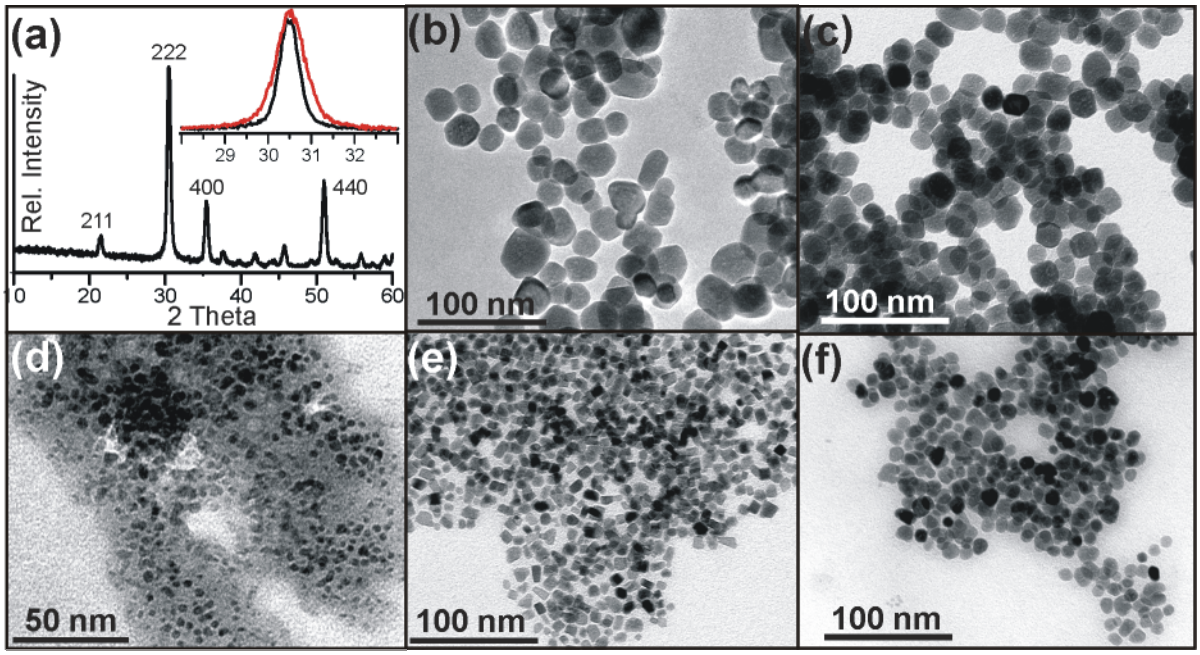

Figure 3.1 a) XRD powder pattern of indium oxide nanoparticles obtained from indium isopropoxide in acetophenone (inset: comparison of 222 reflections of the indium isopropoxide-acetophenone (black curve and indium acetylacetonate-2-butanone (red curve) systems). TEM images of indium oxide nanoparticles obtained in b) indium ispropoxide-benzyl alcohol, c) indium isopropoxide-acetophenone, d) indium acetylacetonate-2-butanone, e) indium acetylacetonate-benzylamine and f) indium acetylacetonate-acetophenone.

According to XRD measurements, all the precipitates consist of cubic indium oxide (ICDD PDF No. 6-416) without indication of other crystalline by-products (Fig. 3.1a). First approximations of the respective particle size were obtained by the Scherrer formula from the (222) reflections, pointing to highly different particle sizes of the various reaction products. Magnification of the (222) reflections of the samples prepared in indium isopropoxide-acetophenone (black curve) and indium acetylacetonate-2-butanone (red curve) nicely illustrates the difference in peak broadening (Fig. 3.1a, inset). These findings are confirmed by TEM investigations. In the systems indium isopropoxide-benzyl alcohol (Fig. 3.1b) and indium isopropoxide-acetophenone (Fig. 3.1c), the obtained indium oxide nanoparticles exhibit basically the same size and shape. The particles are mostly spherical with diameters in the range of 15–30 nm. However, by changing the precursor to indium acetylacetonate, the results change drastically and the particles are much smaller, which can be explained by the much better complexation and stabilization by acetylacetonate ligands as compared to alkoxides. Comparison of Fig. 3.1c (indium isopropoxide-

acetophenone) with Fig. 3.1f (indium acetylacetonate-acetophenone) proves that using the same solvent, however with different precursors, the particle size decreases to about 5–15 nm, but the spherical morphology is preserved. Switching from acetophenone to benzylamine indium oxide nanoparticles with still smaller sizes can be fabricated. However, more striking is the difference in morphology. The particles lost their spherical shape and turned into highly faceted crystals, nevertheless with a rather narrow size distribution (Fig. 3.1e). The reaction of indium acetylacetonate with 2-butanone leads to particle sizes in the range of just a few nanometers (Fig. 3.1d), which is somewhat surprising, as studies for the similar synthesis of titania nanoparticles from $Ti(OiPr)_4$ in various ketone solvents revealed that aromatic species such as acetophenone bind more strongly to the particle surface, resulting in smaller particles than when using aliphatic solvents.[26] It thus appears that these solvent effects are intrinsic to the reaction system and cannot be generalized, but further studies of the growth mechanism and surface functionalization of the resulting In_2O_3 nanoparticles will be required to explain this phenomenon.

3.2.4 Conclusions

The morphology of the final indium oxide nanoparticles depends strongly on the precursor-solvent system, i.e., nanoparticles with the same composition. However when obtained from different precursors in different solvents different sizes and shapes are characterized. This further means, that the organic role in the process is crucial during the formation of the inorganic material. The complete absence of any surfactants, and thus easily accessible surfaces, represents an important advantage with respect to potential applications in gas sensing.

3.3 Nonaqueous synthesis of Nanocrystaline Indium and Zinc Oxide in the Oxygen-Free Solvent Acetonitrile

3.3.1 Introduction

Indium and zinc oxide are among the most investigated metal oxides. Whereas indium oxide is particularly attractive for gas sensing applications[22, 24] and, doped with SnO_2, for transparent conducting films,[27, 28] zinc oxide was studied mainly due to the optical properties.[29] Aqueous as well as nonaqueous sol-gel methods have widely been applied for the synthesis of indium oxide nanoparticles.[23, 30-36] In the case of ZnO, particularly mild synthesis routes have been reported,[37] including biomimetic approaches,[38-41] precipitation methods,[42, 43] or room-temperature organometallic synthesis.[44]

Here we present an alternative process to indium and zinc oxide nanoparticles involving the solvothermal treatment of metal acetylacetonates in acetonitrile. In spite of the moderate reaction temperature of 100 °C, the as-synthesized metal oxides are highly crystalline. As acetonitrile is an oxygen-free solvent, the acetylacetonate ligand obviously acts as oxygen source for the oxide formation. Although both oxides are characterized by small crystallite sizes in the range of just a few nanometers, in the case of ZnO the nanoparticles frequently arrange into mesocrystals with hexagonal habit.

3.3.2 Experimental

In a typical synthesis procedure 0.685 mmol of indium(III) acetylacetonate (0.2823 g) or zinc(II) acetylacetonate (0.1802 g) were added to 20 ml of anhydrous acetonitrile. The reaction mixture was transferred into a Teflon cup of 45 ml inner volume, slid into a steel autoclave, and carefully sealed. The autoclave was heated in a furnace at 100 °C for 2 days. The resulting cloudy suspensions were centrifuged to retrieve the product. Possible organic impurities were removed by repeated washing steps with ethanol. The product was subsequently dried in air at 70 °C. The color of the samples ranged from brownish yellow (In_2O_3) to off-white (ZnO).

3.3.3 Results and Discussion

The synthesis of indium and zinc oxide involved the solvothermal treatment of the respective metal acetylacetonate in acetonitrile without the use of any additional surfactants. Although the reaction temperature of 100 °C is moderate, both samples are characterized by high crystallinity. Figure 3.2 displays the experimental X-ray powder patterns together with the calculated patterns obtained from Rietveld refinement and the difference profiles. In the case of indium oxide, the reflections can be indexed according to the cubic bixbyite structure (ICDD PDF No. 6-416), whereas in the case of ZnO the hexagonal zincite structure is formed (ICDD PDF No. 36-1451). Both diffractograms give no indication for any crystalline by-products.

Rietveld refinement provides further details of the structural characteristics of the indium and zinc oxide samples. The structural parameters from the Rietveld profile refinement for both oxides are presented in Table 3.1. A closer look at the difference curve between the experimental and the calculated XRD patterns proves a good agreement, which supports the chosen structural model. The numerical values of the weighted residual error (R_{wp}) equals to 6.1 % for In_2O_3, 15.1% for ZnO, and the values of goodness-of-fit indicator (GoF) is 1.2 and 1.8, respectively, corroborating the high quality of the fit.

The In_2O_3 crystallizes in the bixbyite structure, similar to the C-type, rare-earth sesquioxide structure, and exhibits a fluoride-related superstructure, where one-fourth of the anions are missing. Indium cations are located at two different six-fold-coordinated sites. One-fourth of the cations are located in trigonally compressed octahedra [*b*-site, symmetry 3, denoted as In(1)], and the remaining three-fourths are located in highly distorted octahedra [*d*-site, symmetry 2, denoted as In(2)]. Each cationic site can be described as a cube, where two anion sites are empty at opposite vertices for In(1) sites and along one diagonal of a face for In(2) sites. The structural oxygen vacancies are located along the four ⟨111⟩ axes. In(1) cation site has six equidistant oxygen anion neighbors at 2.18 Å, while In(2) is also coordinated to six oxygen anions but at three different distances: 2.13, 2.19 and 2.23 Å.[45] The lattice parameters of the In_2O_3 nanoparticles deduced from the refinement equals to 10.114 Å, which is in a good agreement with database value (ICDD PDF No. 6-416). Although the anionic sites of interstitial oxygen vacancy (denoted as O(2) in Table

3.1) in pure In_2O_3 should be empty, we found the presence of interstitial oxygen in the amount of 17.3 %. These oxygen interstitial anions influence the ion-ion distance distorting the In-O octahedron. According to Table 3.1, the interstitial oxygen ions are more strongly bound to the In(1) cations and to the structural oxygen anions O(1) than to the In(2) cations. Furthermore, the length of the In(2)-O(1) bond (2.15 Å) in the nanocrystalline sample is closer to its corresponding value in bulk In_2O_3 (2.13 Å) than the length of the shortest In(1)-O(1) bond (2.08 Å) with the bulk value of 2.18 Å.[46] This observation points out to a more distorted octahedron for In(1)-O than for In(2)-O in the nanocrystallites. The volume-weighted average crystallite size of the In_2O_3 sample was calculated as 6.4 nm. Anisotropy in line broadening (*hkl* directional broadening) was not observed, so that the particle morphology is expected to be spherical.

For the ZnO sample the volume-weighted average grain size is 10.9 nm, while the lattice parameters equal to a = 3.2459 Å, c = 5.1999 Å, which is consistent with the standard values of bulk ZnO (ICDD PDF No. 36-1451). All the peaks are indexed according to hexagonal wurtzite ZnO (Figure 3.2b). Each zinc cation in zincite is in tetrahedral coordination with oxygen, and each oxygen anion is in tetrahedral coordianation to four Zn cations. The calculated Zn-O interatomic distances in coordination tetrahedron are 1.98(1) Å (3x) and 1.95(1) Å (1x along *c*-axis). Other details can be found in Table 3.1.

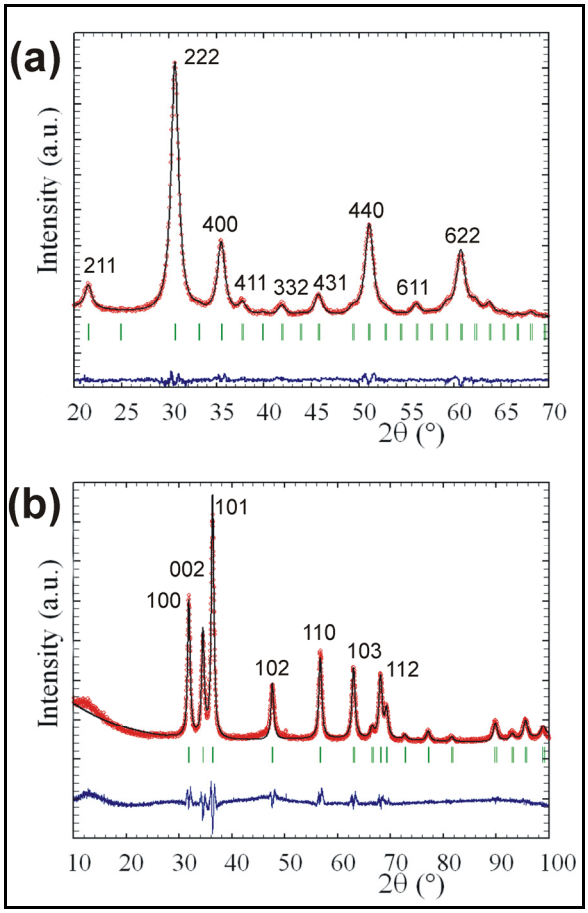

Figure 3.2 Experimental XRD patterns (red), calculated patterns (black) and difference curves (blue) of a) In_2O_3 and b) ZnO. The green short vertical bars correspond to the calculated values of the positions of the Bragg reflections.

Table 3.1 Structural data and refinement parameters for In_2O_3 and ZnO calculated by Rietveld refinement of the XRD powder patters.

	In_2O_3	***ZnO***
Space group	*Ia*-3 (206)	*P*6$_3$mc (186)
Crystal system	Cubic	hexagonal
Lattice parameter (Å)	10.114(1)	a=3.2459(2) c=5.1999(4)
M(1)	In(1)	Zn(1)
X	*x*=*y*=*z*=0.25	*x*=0.333
Y	*x*=*y*=*z*=0.25	*y*=0.666
Z	*x*=*y*=*z*=0.25	*z*=0.387(1)
M(2)	In(2)	
X	0.4677(2)	
Y	0	
Z	0.25	
O(1)		
X	0.384(1)	0.333
Y	0.161(1)	0.666
Z	0.379(2)	0
O(2)		
x=*y*=*z*	0.125	
In(1)-In(2) (Å)	3.353(2)	
In(1)-O(1) (Å)	2.08(1)	
In(2)-O(1) (Å)	2.146(1)	
In(2)-O(2) (Å)	2.393(1)	
In(1)-O(2) (Å)	2.189(1)	
O(1)-O(2) (Å)	2.168(5)	
O(2)-O(2) (Å)	3.576(4)	
Volume-weighted average grain size (nm)	6.4	10.9
Occ. (%)	17.3	
R_{wp} (%)	6.1	15.1
R_B(%)	1.5	8.1
GoF- index	1.2	1.8

Figure 3.3a provides a representative TEM overview image of the In_2O_3 nanoparticles. Although the particles are slightly agglomerated, due to the lack of any stabilizing surfactants, they are clearly distinguishable from each other. They exhibit nearly spherical and rather uniform particle morphology with an average diameter of about 5 nm, agreeing well with the Rietveld data. The HRTEM image in Figure 3.3b shows well-developed lattice fringes often randomly oriented with respect to each other. However, in some cases lattice fringes that are oriented in a parallel way are clearly visible, too. This observation proves the high crystallinity of the nanoparticles as well as a tendency to coalesce in a crystallographically controlled way. The SAED pattern is characterized by Debye-Scherrer rings that are typical of a polycrystalline powder and that can be indexed according to the bixbyite structure (Figure 3.3c). The EDX spectrum of the In_2O_3 sample is presented in Figure 3.3d. In addition to indium and oxygen, also carbon and copper (from the TEM grid) are detected.

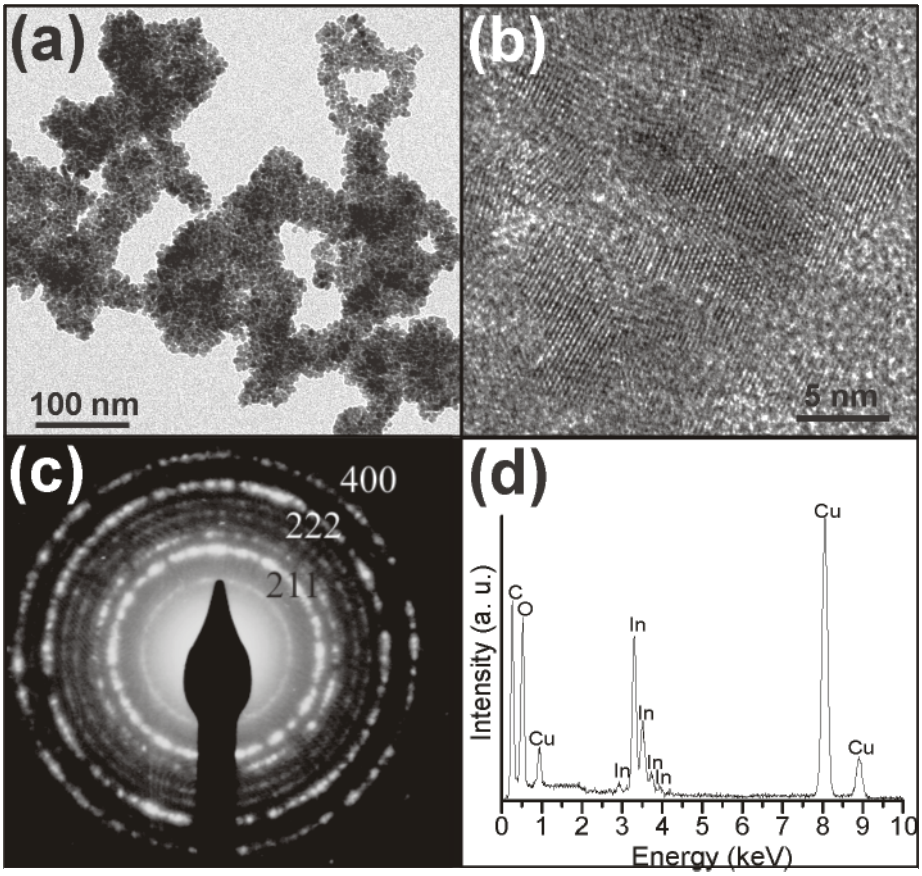

Figure 3.3 a) TEM overview image, b) HRTEM micrograph, c) SAED pattern and d) EDX spectrum of indium oxide nanoparticles.

In comparison with In_2O_3, the ZnO sample has completely different characteristics. The TEM overview image in Figure 3.4a shows individual, hardly agglomerated nanoparticles with a broad size distribution in the range of 15 to 85 nm. The particle morphology seems to be rather irregular, including spherical as well as well faceted shapes. One of these latter, exceptionally large particles with a pronounced hexagonal crystal habit is displayed in the TEM image in Figure 3.4b. The crystal is bounded by {001} upper surface and by ±{100}, ±{010}, ±{1-10} side surfaces (Figure 3.4b, inset). The diameter of the hexagon is 86 nm, which is much larger than the crystallite size obtained by Rietveld data. The presence of two kinds of particles, i.e., with less defined as well as with faceted morphologies, is additionally proven by SEM studies. Figure 3.4c clearly illustrates the rough surface of every particle, pointing to a composite structure, where nanoparticulate units build up these larger structures. This observation is confirmed by HRTEM investigations. A HRTEM image of a part of such a hexagon demonstrates the internal composite structure, which means that the particle is formed by fusion of a large number of small crystallites, just a few nanometers in size (Figure 3.4d). The inner structure becomes visible in form of

differences in contrast, revealing defects and pores. Nevertheless, the lattice fringes of the nanoparticulate building blocks are perfectly aligned, giving rise to sharp spots in the power spectrum (Figure 3.4d, inset). It is interesting to note that the hexagonal crystal structure of the zincite building units is directly reflected in the shape of the mesocrystal.

Similarly shaped mesocrystal hexagons were reported for fluoroapatite synthesized in gelatin gel.[47] The number of reports on mesocrystals consisting of smaller crystallites, however behaving like single crystals is rapidly increasing[48, 49] and includes tungsten and iron oxide platelets,[50, 51] calcium carbonate,[52, 53] copper oxide,[54] strontium titanate,[55] zinc oxide,[56] various other biomaterials.[57-59]

The SAED pattern recorded from a hexagon is composed of dark Laue spots proving that the particle as a matter of fact structurally behaves like a single crystal (Figure 3.4e). By measuring distances and angles between first-order diffraction spots and the central spot, the d-values of Laue spots were calculated, and the corresponding Miller indices were assigned to the first-order reflections. They are displayed in Figure 3.4e. From the geometry of Laue spots and indices of first-order reflections, the zone-axis is determined as [001]. The EDX spectrum clearly proves the presence of zinc and oxygen in the sample (Figure 3.4f).

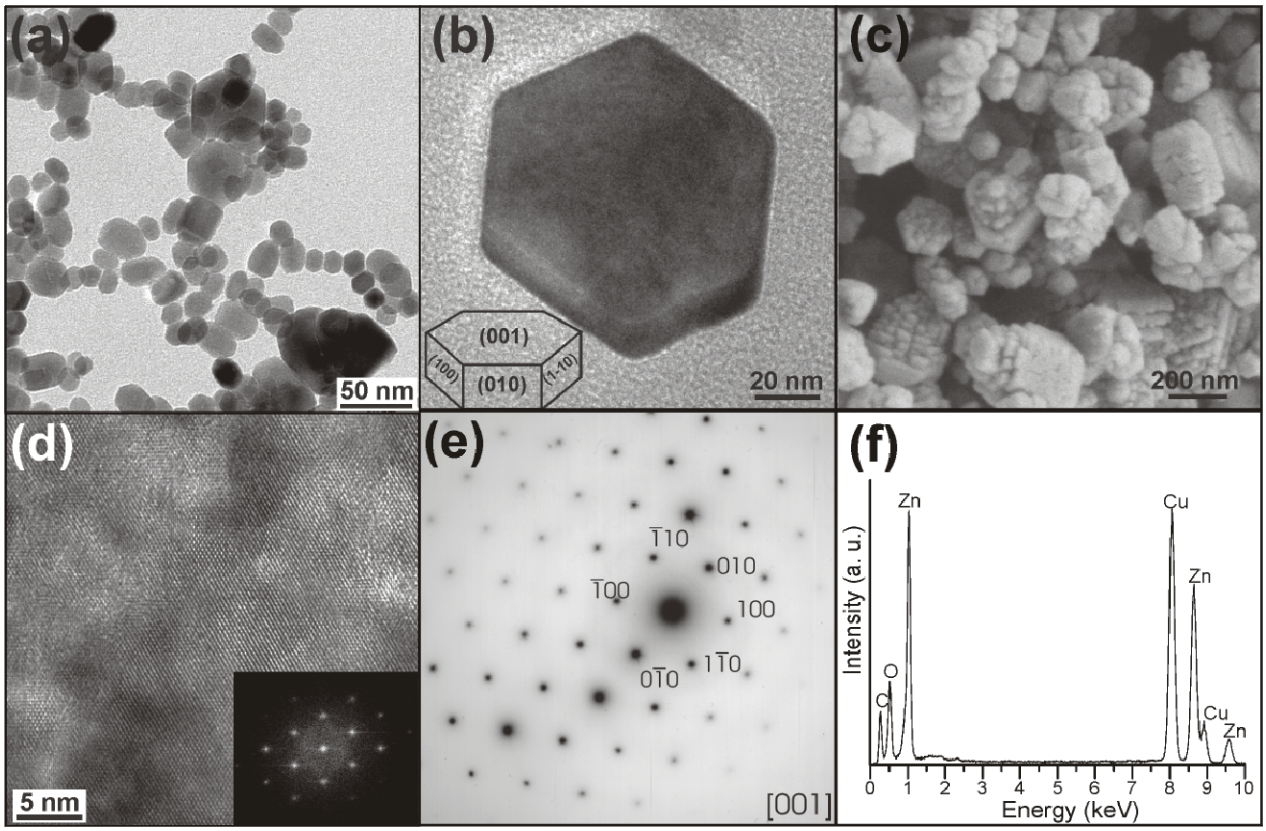

Figure 3.4 a) TEM overview image, b) TEM image of one single well faceted ZnO particle, c) SEM overview image, d) HRTEM image of a part of the ZnO particle in panel b, e) SAED pattern the ZnO particle in panel b, and f) EDX spectrum of the ZnO sample.

The synthesis approach reported here involves the use of an oxygen-containing precursor and an oxygen-free solvent. Accordingly, the oxygen for the oxide formation is provided by the acetylacetonate ligand of the precursor, which is chemically transformed during the solvothermal treatment. Analogous synthesis strategies have been reported for various other metal oxide nanoparticles, where metal acetylacetonates were reacted with amines.[31, 34, 60] In these cases, the formation mechanism can easily be explained by aminolysis of the acetylacetonate ligand, followed by ketimine-like condensation steps.[34] However, using acetonitrile as solvent makes the elucidation of the condensation mechanism much more complicated. After removal of the In_2O_3 nanoparticles, the composition of the final reaction mixture was studied by NMR and GC-MS. The mixture was highly complex and impossible to resolve completely. The main species found were 2,4,6-trimethyl-1,3,5-triazine, acetylpyrazine, allyl-trimethylpyrazine and propenyl-trimethylpyrazine. Obviously, even in such a simple system like indium acetylacetonate and acetonitrile many organic reactions occur in parallel, leading to a large number of organic products. The lack of any species present in large excess makes it impossible to

correlate the organic side of the reaction with the formation of the inorganic nanoparticles.

3.3.4 Conclusions

An extension of the nonaqueous routes to metal oxide nanoparticles is presented, based on the reaction of metal acetylacetonates with acetonitriles at the moderate temperature of 100 °C. The indium as well as zinc oxide reaction system leads to the formation of homogeneous nanocrystallites in the size range of 5-10 nm. However, whereas the indium oxide sample consists of individual nanocrystallites, the zinc oxide nanocrystallites frequently arrange into mesocrystals with a well-faceted hexagonal shape. In this context, it is remarkable that the hexagonal crystal structure of the zincite nanobuilding blocks is reflected in the final shape of the mesocrystal assembly. It is intriguing to see that such simple reaction systems like zinc acetylacetonate and acetonitrile are able to induce the formation of rather complex structures without any additional structure-direction agents. On the other hand, the large number of organic species detected in the final reaction point to complex reaction pathways. All these findings prove that the study of the role of the organic components during nanoparticle formation is a prerequisite on the way to understand and control the nonaqueous synthesis of metal oxides.

3.4 Synthesis of Titania Nanoparticles in Aromatic Solvents

3.4.1 Introduction

Titanium dioxide (TiO_2) is one of the most widely found oxides in the mineral form. With respect to its outstanding chemical and physical properties and variety of different applications in photocatalysis,[61] photovoltaics,[62, 63] photochemical water splitting,[64] and sensing,[65] the synthesis of titanium oxide nanomaterials remains an attractive objective. Among the various nanostructures, especially the large surface-to-volume ratio of anisotropic nanoparticles results in a favorable combination of high specific surface areas with improved conduction paths, having significant implications for solar energy conversion and photocatalysis.[66] The two main modifications of TiO_2 are anatase and rutile. These two structures differ by the distortion of each octahedron and by the assembly pattern of the chains.[67] Although the transformation

rate is influenced by the particle size and the presence of impurities, upon heating, anatase phase is anyhow transformed into rutile between 600 °C and 1100 °C.[68] On the other hand, physical and chemical characteristics, that are the most important aspect towards applications, are influenced not only by its crystalline phase but also by its particle size and morphology.[69] Because of its unusual electrical, optical and catalytic properties, the synthesis of TiO_2 is a well-established process. Most groups have focused on aqueous sol-gel synthesis, where a titania precursor is hydrolyzed to induce the condensation.[69] Recent work has shown that nonaqueous synthesis methods provide a generally applicable tool to obtain surface-functionalized nanoparticles[14, 70] with excellent control over particle size,[20] shape,[19] crystallinity and surface functionalization.[71]

A detailed study on the influence of different types of solvents showed that highly crystalline anatase nanoparticles of 5–20 nm in size were obtained by reacting titanium tetraisopropoxide with common ketones and aldehydes under solvothermal conditions.[26] Following this work, titanium tetraisopropoxide was solvothermally reacted with aromatic solvents such as benzamide and benzoylacetone, in order to prove the generality and versatility of the nonaqueous sol-gel approach and to study their influence on the morphology of the final product.

3.4.2 Experimental

In a typical synthesis procedure, samples were prepared in a rather concentrated fashion in a molar ratio of 1:10. 4 mmol of the titanium tetraisopropoxide (1.136g) was mixed with 40 mmol of the respective solvent (4.846g of benzamide and 6.488g of benzoylacetone). The reaction mixture was transferred into a Teflon cup of 45 ml inner volume, slid into a steel autoclave, and carefully sealed. The autoclave was heated in a furnace at 200 °C for 3 days. The precipitate became yellow upon washing with tetrahydrofurane, and was subsequently dried in air at 70 °C.

3.4.3 Results and Discussion

Figure 3.5 shows the XRD patterns measured for the TiO_2 nanoparticles prepared in a) benzoylacetone and b) benzamide. Both solvents are solid at room temperature, but since the melting points are 60 °C and 127 °C, respectively, the reaction temperature is chosen to be above these temperatures. The patterns are very similar

and the reflections (101, 004, 200, 105, 211 and 204) correspond to the anatase crystalline phase (ICDD PDF No. 21-1272). The peaks are rather sharp, also compared to the ones obtained from $TiCl_4$ in benzylalcohol[20] (Figure 3.5.c). The particle size was calculated from the XRD patterns using the Scherrer equation and the (101) reflection.

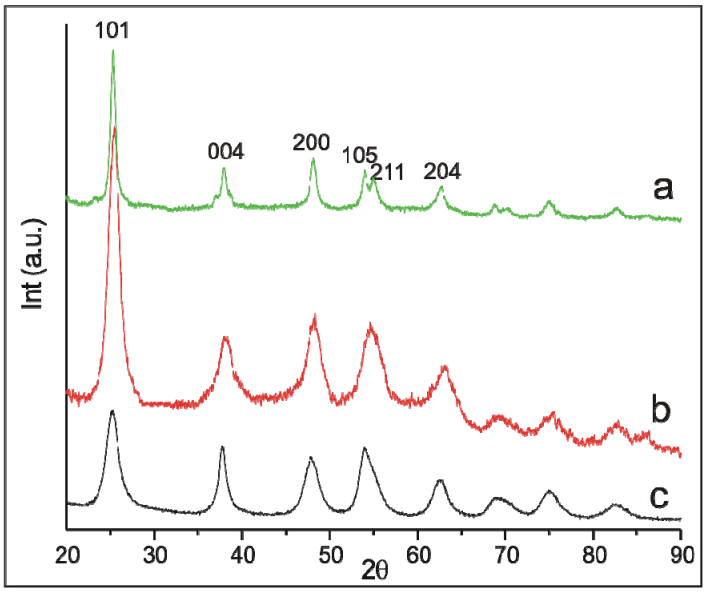

Figure 3.5 XRD patterns of the obtained titania particles a) from $Ti(OiPr)_4$ and benzoylacetone, b) from $Ti(OiPr)_4$ and benzamide, c) from $TiCl_4$ and benzylalcohol (reference pattern)

Additional experiments were done by increasing the reaction time or temperature. In both cases, as expected, the crystallite sizes of the samples were considerably enlarged. It is also noteworthy that the solvent-to-precursor ratio plays a significant role as well. When less concentrated reaction systems were exploited, the final nanopowders were either not pure phase samples according to XRD, or the yield and the crystallinity were not as high.

The particles were studied also by TEM, SAED and SEM. Figure 3.6 displays the obtained particles after washing for both systems. In case of benzamide, the sample does not contain any larger species but consists entirely of slightly elongated particles. This overview TEM image shows that their size ranges from 5 nm to 9 nm, which is in good agreement with the data obtained from XRD peak broadening calculated to be 7 nm. The electron diffraction pattern is presented in Figure 3.6a, inset, and proves that the material is highly crystalline with the reflections 101, 004 and 200 pointing to the anatase TiO_2 (ICDD PDF No. 21-1272). In the case of

benzoylacetone, the sample was quite agglomerated, so SEM measurements were done instead. It can be stated that the particles are quite uniform in size and shape, although it is rather difficult to see distinct boundaries. Based on this image (Figure 3.6b), the estimated particle size is about 20 nm, which is in good correspondence with the average crystallite size of 17 nm calculated from the (101) diffraction peak (Figure 3.5b).

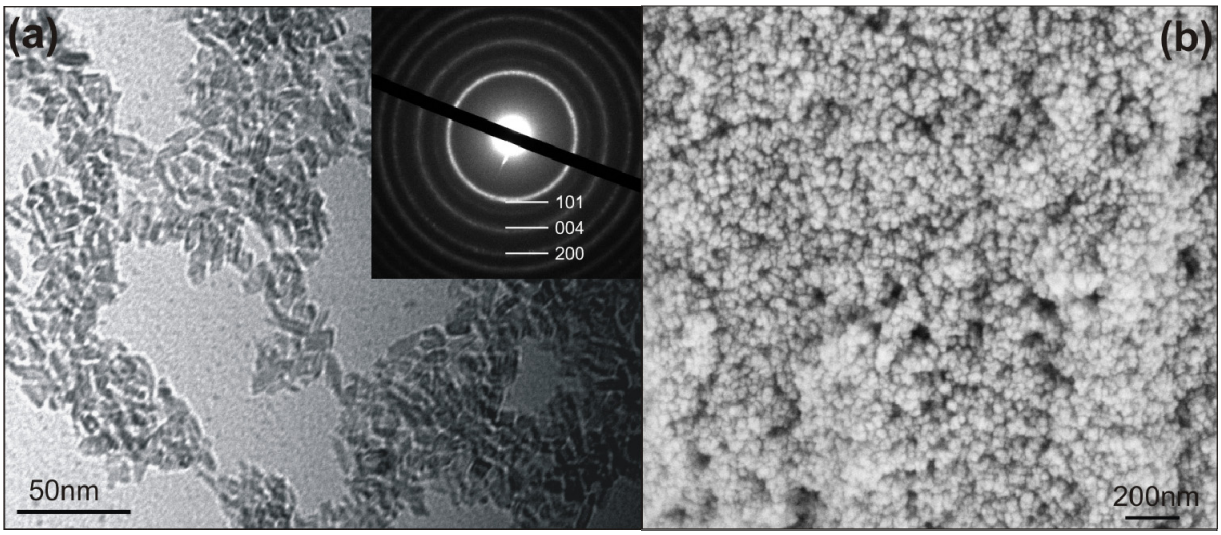

Figure 3.6 a) TEM image of titania nanoparticles synthesized in benzamide, and its electron diffraction pattern (inset), b) SEM image of titania nanoparticles synthesized in benzoylacetone.

In order to evaluate the formation mechanism, the obtained reaction solutions should be filtered to remove any remaining particles, and then subjected to NMR and GC-MS analysis to investigate the side products of the reactions. However, by starting from “solid solvents” “solid reaction mixtures” were the end products, and thus it is not possible to get an insight into side products of these reactions. However, it is expected that the anatase nanoparticles are a result of an ether elimination process.[72]

3.4.4 Conclusions

We proved that the nonaqueous synthesis of highly crystalline titania nanoparticles can be extended to organic solvents other than alcohols, ethers, ketones and aldehydes, also providing the essential Ti-O-Ti bridges for oxide formation. Moreover it can be extended to uncommon solvents that would never be suspected to be suitable, because they are solid at room temperature. In general, the high concentration of the precursor and the excellent yields are promising aspects.

However, there are so many systems available with a less complicated washing procedure, so that these synthesis systems will find applications only in selected and special cases. Nevertheless, the results prove the generality as well as the robustness of these approaches, adding some new systems to the growing library of precursor-solvent-combinations for the synthesis of metal oxide nanoparticles.

3.5 Solvothermal and Surfactant Free Synthesis of Crystalline Niobium Oxide, Hafnium Oxide and Tantalum Oxide Nanoparticles

3.5.1 Introduction

Nonhydrolitic sol-gel routes using halides and alcohols have been reported for the synthesis of silica gels[73] and monolithic titania.[74] The $TiCl_4$ and benzyl alcohol reaction system provides a preparation route to spherical, “quasi” zero-dimensional titania nanoparticles with excellent control over particle size, shape and crystallinity by choosing the appropriate thermal conditions and relative amounts of the solvent.[20] Furthermore, it has been applied as a general route to nanosized, low-dimensional transition metal oxides such as vanadium oxide nanorods and tungsten oxide nanoplatelets.[19] In contrast to most of the sol-gel processes that lead to amorphous materials, the as-synthesized nanoparticles were crystalline already at moderate temperatures.

Following this direction, we extended the transition metal halide – benzyl alcohol reaction system to three important metal oxides that are particularly hard to obtain on the nanoscale via soft-chemistry routes, namely Nb_2O_5, Ta_2O_5 and HfO_2.

The preparation of Nb_2O_5 is quite a difficult task and only few reports were published so far. The polyol-mediated synthesis at 300 °C with particles ranging from 30-200 nm,[75] crystalline 4.5 nm sized nanoparticles starting from a niobic acid precipitate[76] and square-like platelets ranging from 50 to 80 nm were synthesized via nonaqueous sol-gel approach, starting from niobium ethoxide as a precursor.[77] Since the niobium oxide exhibits a high dielectric constant and a good thermal stability, it is used as thin film capacitor.[78] Because of its outstanding chemical and physical properties the whole group V oxides, including niobium and tantalum oxides, constitutes promising

candidates for applications in electrochemistry[79, 80] and electrochromic device technology,[79, 81, 82] whereas hafnium oxide thin films with nanometer dimensions have been crystallographically analyzed[83] and even found some magnetic applications.[84]

3.5.2 Experimental

In a typical synthesis procedure the transition metal chloride (either 200 mg of $NbCl_5$, $HfCl_4$ or $TaCl_5$) was added to 20 ml of anhydrous benzyl alcohol. The reaction mixture was transferred into a Teflon cup of 45 ml inner volume, slid into a steel autoclave, and carefully sealed. The autoclave was heated in a furnace at 220 °C (250 °C in case of Nb_2O_5) for 3 days. The resulting cloudy suspensions were centrifuged to retrieve the product and thoroughly washed with either ethanol or tetrahydrofurane in order to remove possible organic impurities. The products were subsequently dried in air at 70 °C.

3.5.3 Results and Discussion

Usually the samples synthesized via sol-gel processes have the general drawback that subsequent heat treatment is necessary to induce crystallization. Our samples are already as-synthesized highly crystalline. Powder X-ray diffraction (XRD) patterns of the obtained materials are shown in Figure 3.7.

Powder X-ray diffraction pattern of the obtained niobium oxide (Figure 3.7a) confirms the formation of phase-pure hexagonal TT-Nb_2O_5 (ICDD PDF No. 28-317). In this procedure, also phase- pure monoclinic HfO_2 (ICDD PDF No. 43-1017), s. g. $P2_1c$ and phase-pure orthorhombic Ta_2O_5 (ICDD PDF No. 25-922), s. g. $P2_12_12$ were established. To confirm the structure of the poorly crystalline as-synthesized Ta_2O_5 additional calcination was applied at 600 °C for 4h. Below this temperature the crystallinity was not higher then in the as-prepared sample. Obviously the temperature of at least 600 °C is necessary to improve the crystallization towards larger species (Figure 3.7d). The sharp reflections can without any doubts be assigned to the orthorhombic structure of Ta_2O_5.

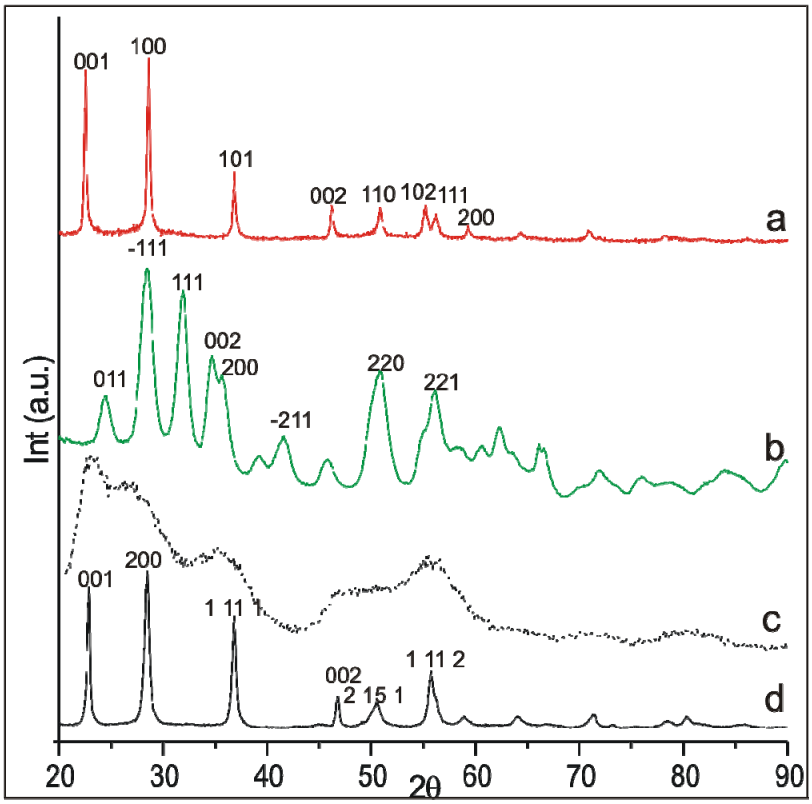

Figure 3.7 X-ray powder diffraction patterns of the as-synthesized a) niobium oxide, b) hafnium oxide and c) as synthesized (dashed line) and d) calcined sample of tantalum oxide.

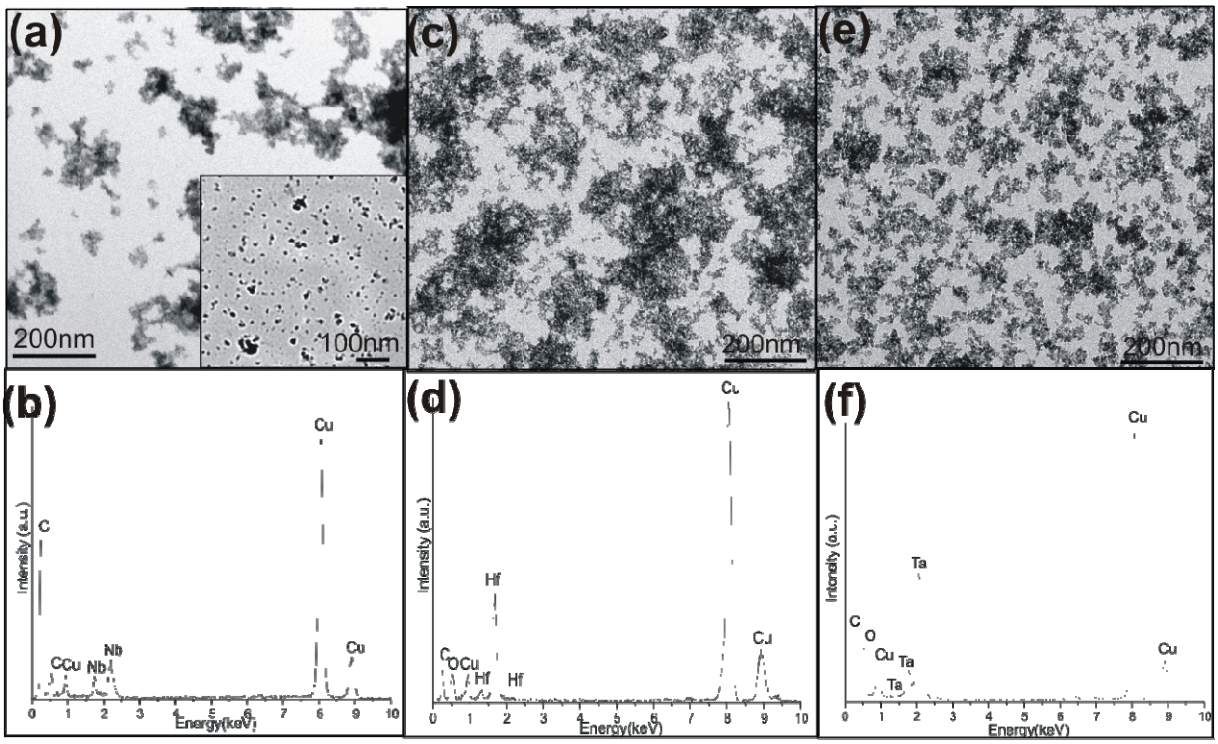

Figure 3.8 TEM overview images of as prepared metal oxide nanoparticles obtained from halide precursors in benzyl alcohol a) Nb_2O_5 (inset: closer view TEM picture), c) HfO_2, e) Ta_2O_5. EDX spectrums of b) niobium oxide, d) hafnium oxide and e) tantalum oxide.

Representative transmission electron microscopy (TEM) images reveal the unique morphology differences of the oxidic particles. Although the samples are slightly agglomerated, due to the lack of any stabilizing surfactant, it is possible to distinguish grain boundaries and estimate the size range of nanoparticles from the TEM pictures. The nanoparticles exhibit a spherical morphology with uniform shapes and relatively small particle size distributions. According to EDX measurements, only the respective metals and oxygen are present, confirming the purity of the samples.

In the case of Nb_2O_5, slightly agglomerated spherical particles were observed, ranging from 18 to 35 nm (Figure 3.8a), which is in good correlation with the average crystallite size of 27.2 nm, calculated by using Scherrer equation[85] from the line broadening of the (100) diffraction peak (Figure 3.7a). From EDX measurments (Figure 3.8b) it is obvious that there are no other elements then Nb and O present in the sample, besides Cu and C, which are expected from carbon coated copper (TEM) grid. A TEM overview image of the hafnia nanoparticles synthesized at 220 °C is displayed in Figure 3.8c, whereas Figure 3.8e shows a TEM image of the as-synthesized Ta_2O_5 nanoparticles. These overview images demonstrate that in addition to individual particles, also some agglomerates are present. EDX spectra of both HfO_2 (Figure 3.8d) and Ta_2O_5 (Figure 3.8f) are confirming the purities of these samples.

Further characterization techniques, HRTEM, SAED and PS were applied for each of the synthesized nanopowders. High-resolution TEM investigations give further insight into the structural features of the nanoparticles. The well defined lattice planes prove the high crystallinity of the particles, and the power spectrum of these images proves well oriented nanocrystallites along below discussed directions. On the other hand selected area electron diffraction measurement are showing well developed Debye-Scherrer rings, that are after calculating the d spacing, confirming the reflections identified in the X-ray patterns in Figure 3.7 for all of the samples.

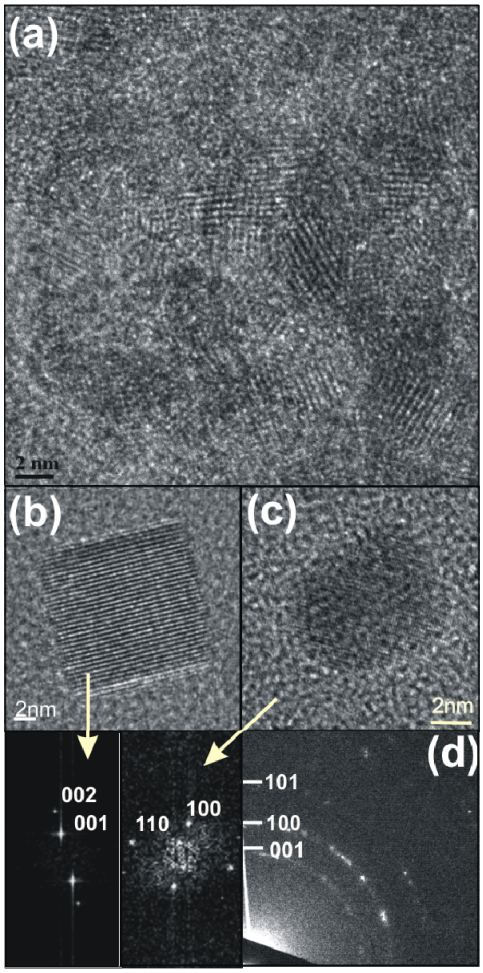

Figure 3.9 a) HRTEM image of as-prepared Nb_2O_5 sample, b) and c) HRTEM of isolated nanoparticles and their respective PS, pointed out with the arrows, d) selected area electron diffraction.

The HRTEM image of the niobium oxide sample reveals well-developed lattice fringes (Figure 3.9a), and additional HRTEM images of separate particles (Figure 3.9b and Figure 3.9c) show several lattice planes, further proving the high crystallinity. The sharp reflections of the power spectra, (Figure 3.9, marked by arrows), coincide with the hexagonal Nb_2O_5 (ICDD PDF No. 28-317). The lattice distances measured from the selected area electron diffraction (SAED) pattern (Figure 3.9d) match with the suggested structure.

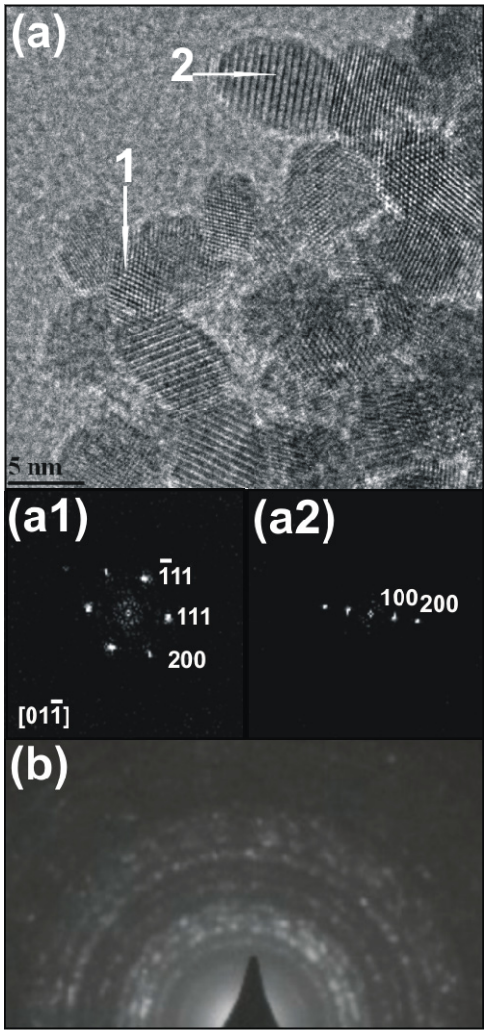

Figure 3.10 a) HRTEM image of as-prepared HfO_2 sample, a1) and a2) PS of with the arrows pointed out particles, marked as 1 and 2, respectively and b) respective SAED pattern.

The discrete, spherical particles are in the range from 4 to 9 nm, according to TEM and HRTEM (Figure 3.8c and Figure 3.10a) measurements, and in good correspondence with the average crystallite size calculated from the (-111) diffraction peak (Figure 3.7b). The sharp reflections of the Fourier transform (power spectrum) of the particle marked with the number 1 (Figure 3.10a1) is oriented along the [01-1] direction. The other particle, marked with number 2, gives rise to two pairs of sharp spots, which can be attributed to the 100 and 200 reflections and match with the monoclinic HfO_2 structure although the particle itself is not oriented (Figure 3.10a2). The Debye-Scherrer rings of the whole sample are clearly indicating the polycrystalline nature of the powder, and once more confirming the proposed HfO_2 structure.

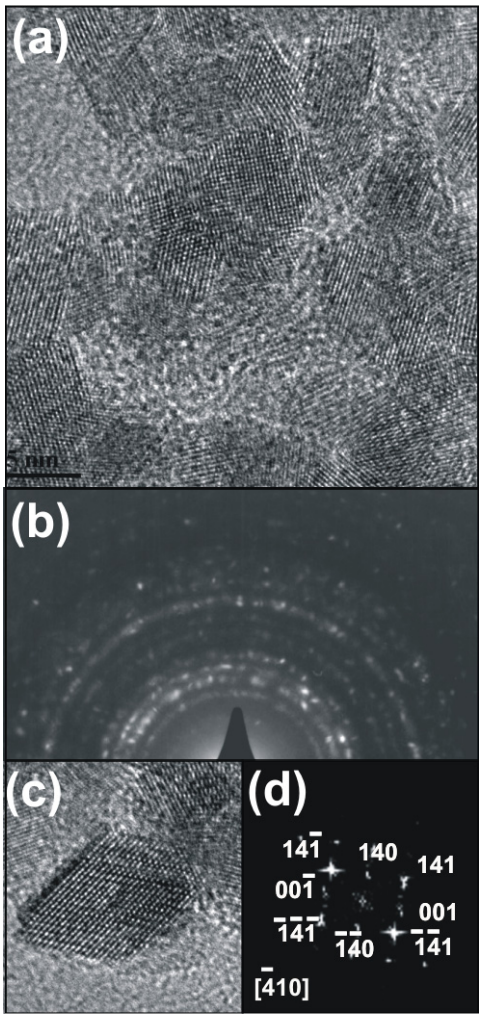

Figure 3.11 a) HRTEM image of as-prepared Ta_2O_5 sample, b) respective SAED pattern, c) HRTEM of an isolated nanoparticle and d) its respective PS.

A closer view on the area with well dispersed particles of tantalum oxide by HRTEM demonstrates that the particle size distribution is in the range of 3 to 7 nm (Figure 3.11a), which is in good agreement with the crystallite sizes calculated by Scherrer equation (5 nm). The particles are not only characterized by a relatively narrow size distribution, but also exhibit a nearly spherical and uniform particle size. Additionally the well-developed lattice fringes are randomly oriented, which proves the high crystallinity of the sample and random orientation of the nanoparticles with respect to each other. The PS of one particle (Figure 3.11d) corresponds to the orientation along the [-410] direction. The SAED pattern (Figure 3.11b) shows diffuse diffraction rings that can be unambigously attributed to the orthorhombic Ta_2O_5 structure.

Nonhydrolitic pathways for transition metal oxides mainly involve the reaction of metal chlorides with either a metal alkoxide or an organic oxygen donor such as an alcohol or an organic ether.[86] A reaction pathway for these kinds of systems is already established and usually involves the condensation between M-Cl and M-OR functions under elimination of alkyl halides, so that M-O-M bridges can be formed. That is the main reason why the reaction mechanism was not studied in more details.

These examples show that the metal halide/alcohol system with its low reaction temperature is particularly useful and versatile in cases in which is really hard to obtain nanoparticles of the respective metal oxides. On the other hand metal halides are a problem when high purity of the product is required, as halide impurities often remain in the final oxidic material, and this contamination is detrimental for applications in catalysis or gas sensing. However we have proven, both with EDX measurements, and elemental analysis, that our samples are halide-free, and we hope that they will find some of the promising applications in the near future.

As a possible application the as-synthesized Nb_2O_5 sample was tested as cathode material for lithium ion batteries. Figure 3.12a shows the first four discharge (Li extraction) / charge (Li insertion) curves for the Nb_2O_5 sample. The first reversible capacity was as high as 290 mA h g^{-1}. After passing via the external circuit to the positive Nb_2O_5 electrode where electrochemical reaction leads to the formation of $Li_xNb_2O_5$ via reduction of Nb_2O_5 with intercalation of Li+ into the oxide, reasonably high discharge capacity of 290 mA h g^{-1}, and charge-discharge cycling between 0 and 2 V vs. Li/Li is achieved. As an important finding, the reversible capacity stabilized after around 15 cycles at values of around 160 mA h g^{-1} (Figure 3.12b), which is significant result for the hexagonal Nb_2O_5 reported so far to the best of our knowledge.[87] Further more columbic efficiency of more then 90% is proving the concept itself and gives rise to further investigations and possible improvements.

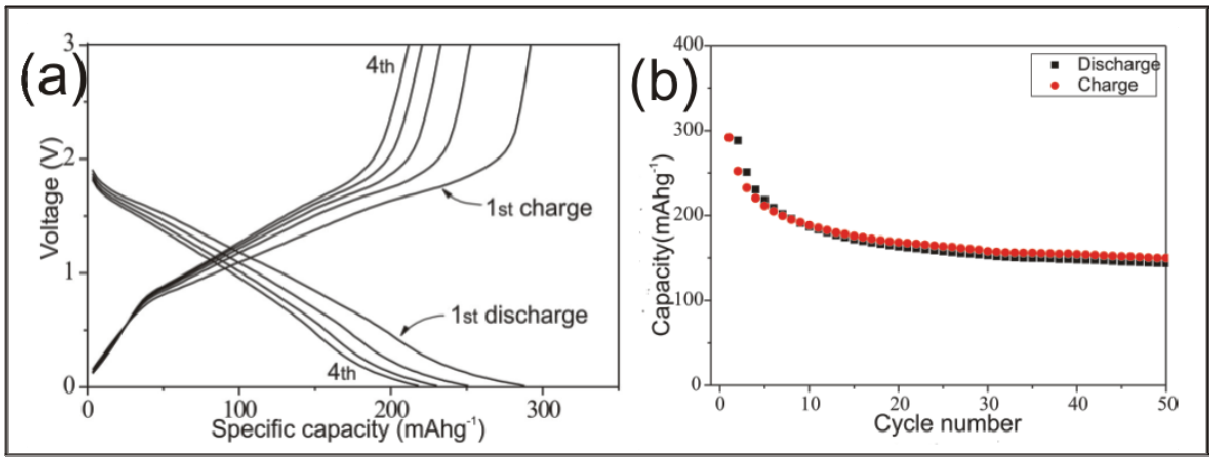

Figure 3.12 a) Galvanostatic discharge (Li extraction, voltage decreases) / charge (Li insertion, voltage increases) curves and b) cycling performance of the as-synthesized sample of Nb_2O_5. The sample was cycled at a rate of C/5.

3.5.4 Conclusions

This part of the work illustrates the successful synthesis of high-quality transition metal oxide nanoparticles via a nonaqueous sol-gel route at low temperatures. The reaction between transition metal chlorides and benzyl alcohol leads to highly crystalline nanoparticles with increasing importance towards application in magnetism by doping in case of HfO_2 or lithium ion batteries in case of Nb_2O_5, which is the research in progress at the moment. Usually the use of the halide precursors or additionally the presence of a large amount of surfactants such as trioctylphosphine oxide and octylamine lead to impurities in the final product and, thus, hamper possible applications in electronic devices. However, this is not the case for our system because it is proved with both EDX measurements and elemental analysis that the samples are halide-free and no surfactant is used in the synthesis procedure. In addition the process itself is simple, allows a scale-up in gram quantities and offers a possibility of making this route even more general.

3.6 References

[1] L. L. Hench, J. K. West, *Chem. Rev.* **1990**, *90*, 33.

[2] B. L. Cushing, V. L. Kolesnichenko, C. J. O'Connor, *Chem. Rev.* **2004**, *104*, 3893.

[3] J. Livage, M. Henry, C. Sanchez, *Prog. Solid State Chem.* **1988**, *18*, 259.

[4] M. Niederberger, G. Garnweitner, N. Pinna, G. Neri, *Prog. Solid State Chem.* **2005**, *33*, 59.

[5] G. Garnweitner, M. Niederberger, *J. Am. Ceram. Soc.* **2006**, *89*, 1801.

[6] Y. W. Jun, J. S. Choi, J. Cheon, *Angew. Chem. Int. Ed.* **2006**, *45*, 3414.

[7] M. Niederberger, G. Garnweitner, *Chem.--Eur. J.* **2006**, *12*, 7282.

[8] T. Hyeon, *Chem. Commun.* **2003**, 927.

[9] C. Wang, Z. Deng, Y. Li, *Inorg. Chem.* **2001**, *40*, 5210.

[10] H. Parala, A. Devi, R. Bhakta, R. A. Fischer, *J. Mater. Chem.* **2002**, *12*, 1625.

[11] G. Wang, G. Li, *Eur. Phys. J. D* **2003**, *24*, 355.

[12] C. S. Kim, B. K. Moon, J. H. Park, S. T. Chung, S. M. Son, *Jour. Cryst. Growth* **2003**, *254*, 405.

[13] Y. W. Jun, M. F. Casula, J. H. Sim, S. Y. Kim, J. Cheon, A. P. Alivisatos, *J. Am. Chem. Soc.* **2003**, *125*, 15981.

[14] J. Joo, T. Yu, Y. W. Kim, H. M. Park, F. X. Wu, J. Z. Zhang, T. Hyeon, *J. Am. Chem. Soc.* **2003**, *125*, 6553.

[15] J. Rockenberger, E. C. Scher, A. P. Alivisatos, *J. Am. Chem. Soc.* **1999**, *121*, 11596.

[16] T. Hyeon, S. S. Lee, J. Park, Y. Chung, H. B. Na, *J. Am. Chem. Soc.* **2001**, *123*, 12798.

[17] S. H. Sun, H. Zeng, *J. Am. Chem. Soc.* **2002**, *124*, 8204.

[18] J. Park, K. An, Y. Hwang, J. G. Park, H. J. Noh, J. Y. Kim, J. H. Park, N. M. Hwang, T. Hyeon, *Nat. Mater.* **2004**, *3*, 891.

[19] M. Niederberger, M. H. Bartl, G. D. Stucky, *J. Am. Chem. Soc.* **2002**, *124*, 13642.

[20] M. Niederberger, M. H. Bartl, G. D. Stucky, *Chem. Mater.* **2002**, *14*, 4364.

[21] W. S. Nam, G. Y. Han, *Korean J. Chem. Eng.* **2003**, *20*, 1149.

[22] G. Eranna, B. C. Joshi, D. P. Runthala, R. P. Gupta, *Crit. Rev. Solid State Mater. Sci.* **2004**, *29*, 111.

[23] N. Pinna, G. Neri, M. Antonietti, M. Niederberger, *Angew. Chem. Int. Ed.* **2004**, *43*, 4345.

[24] G. Neri, A. Bonavita, G. Micali, G. Rizzo, S. Galvagno, M. Niederberger, N. Pinna, *Chem. Commun.* **2005**, *48*, 6032.

[25] J. Park, E. Lee, N.-M. Hwang, M. Kang, S. C. Kim, Y. Hwang, J.-G. Park, H.-J. Noh, J.-Y. Kim, J.-H. Park, T. Hyeon, *Angew. Chem. Int. Ed.* **2005**, *44*, 2872.

[26] G. Garnweitner, M. Antonietti, M. Niederberger, *Chem. Commun.* **2005**, 397.

[27] T. Minami, *Semicond. Sci. Technol.* **2005**, *20*, S35.

[28] J. Ba, D. Fattakhova Rohlfing, A. Feldhoff, T. Brezesinski, I. Djerdj, M. Wark, M. Niederberger, *Chem. Mater.* **2006**, *18*, 2848.

[29] A. B. Djurisic, Y. H. Leung, *Small* **2006**, *2*, 944.

[30] A. Gurlo, M. Ivanovskaya, N. Barsan, M. Schweizer-Berberich, U. Weimar, W. Göpel, A. Dieguez, *Sens. Actuators, B* **1997**, *44*, 327.

[31] W. S. Seo, H. H. Jo, K. Lee, J. T. Park, *Adv. Mater.* **2003**, *15*, 795.

[32] K. Soulantica, L. Erades, M. Sauvan, F. Senocq, A. Maisonnat, B. Chaudret, *Adv. Funct. Mater.* **2003**, *13*, 553.

[33] M. Epifani, P. Siciliano, A. Gurlo, N. Barsan, U. Weimar, *J. Am. Chem. Soc.* **2004**, *126*, 4078.

[34] N. Pinna, G. Garnweitner, M. Antonietti, M. Niederberger, *J. Am. Chem. Soc.* **2005**, *127*, 5608.

[35] M. Epifani, R. Diaz, J. Arbiol, E. Comini, N. Sergent, T. Pagnier, P. Siciliano, G. Faglia, J. R. Morante, *Adv. Funct. Mater.* **2006**, *16*, 1488.

[36] A. Narayanaswamy, H. Xu, N. Pradhan, M. Kim, X. Peng, *J. Am. Chem. Soc.* **2006**, *128*, 10310.

[37] D. Ganguli, *J. Sol-Gel Sci. Tech.* **2006**, *39*, 5.

[38] Z. R. Tian, J. A. Voigt, J. Liu, B. Mckenzie, M. J. Mcdermott, *J. Am. Chem. Soc.* **2002**, *124*, 12954.

[39] P. Gertsel, R. S. Hoffmann, P. Lipowsky, L. P. H. Jeurgens, J. Bill, F. Aldinger, *Chem. Mater.* **2006**, *18*, 179.

[40] L. P. Bauermann, J. Bill, F. Aldinger, *J. Phys. Chem. B* **2006**, *110*, 5182.

[41] Y. Peng, A. W. Xu, B. Deng, M. Antonietti, H. Colfen, *J. Phys. Chem. B* **2006**, *110*, 2988.

[42] T. Kawano, H. Imai, *Cryst. Growth Des.* **2006**, *6*, 1054.

[43] M. M. Demir, R. Munoz-Espi, I. Lieberwirth, G. Wegner, *J. Mater. Chem.* **2006**, *28*, 2940.

[44] M. Monge, M. L. Kahn, A. Maisonnat, B. Chaudret, *Angew. Chem. Int. Ed.* **2003**, *42*, 5321.

[45] González G. B., Cohen J. B., Hwang J-H., Mason Th. O., Hodges J. P., Jorgensen J. D., *J. Appl. Phys.* **2001**, *89*, 2550.

[46] N. Nadaud, N. Lequeux, M. Nanot, J. Jove, T. Roisnel, *J. Solid State Chem.* **1998**, *135*, 140.

[47] S. Busch, U. Schwarz, R. Kniep, *Adv. Funct. Mater.* **2003**, *13*, 189.

[48] H. Cölfen, M. Antonietti, *Angew. Chem. Int. Ed.* **2005**, *44*, 5576.

[49] M. Niederberger, H. Colfen, *Phys. Chem. Chem. Phys.* **2006**, *8*, 3271.

[50] M. Niederberger, F. Krumeich, K. Hegetschweiler, R. Nesper, *Chem. Mater.* **2002**, *14*, 78.

[51] J. Polleux, N. Pinna, M. Antonietti, M. Niederberger, *J. Am. Chem. Soc.* **2005**, *127*, 15595.

[52] T. X. Wang, H. Cölfen, M. Antonietti, *J. Am. Chem. Soc.* **2005**, *127*, 3246.

[53] T. X. Wang, H. Cölfen, M. Antonietti, *Chem.--Eur. J.* **2006**, *12*, 5722.

[54] Z. Zhang, H. Sun, X. Shao, D. Li, H. Yu, M. Han, *Adv. Mater.* **2005**, *17*, 42.

[55] V. R. Calderone, A. Testino, M. T. Buscaglia, M. Bassoli, C. Bottino, M. Viviani, V. Buscaglia, P. Nanni, *Chem. Mater.* **2006**, *18*, 1627.

[56] Y. Liu, X. Huang, K. M. Sulieman, F. Sun, X. He, *J. Phys. Chem. B* **2006**, *110*, 10612.

[57] M. Rousseau, E. Lopez, P. Stempfle, M. Brendle, L. Franke, A. Guette, R. Naslain, X. Bourrat, *Biomaterials* **2005**, *26*, 6254.

[58] Y. Oaki, H. Imai, *Angew. Chem. Int. Ed.* **2005**, *44*, 6571.

[59] Y. Oaki, H. Imai, *Small* **2006**, *2*, 66.

[60] W. S. Seo, H. H. Jo, K. Lee, B. Kim, S. J. Oh, J. T. Park, *Angew. Chem. Int. Ed.* **2004**, *43*, 1115.

[61] Z. B. Zhang, C. C. Wang, R. Zakaria, J. Y. Ying, *J. Phys. Chem. B* **1998**, *102*, 10871.

[62] A. Hagfeldt, M. Gratzel, *Acc. Chem. Res.* **2000**, *33*, 269.

[63] E. W. McFarland, J. Tang, *Nature* **2003**, *421*, 616.

[64] S. U. M. Khan, M. Al-Shahry, W. B. Ingler Jr., *Science* **2002**, *297*, 2243.

[65] M. Ferroni, M. C. Carotta, V. Guidi, G. Martinelli, F. Ronconi, M. Sacerdoti, E. Traversa, *Sens. Actuators, B* **2001**, *77*, 163.

[66] D. G. Shchukin, J. H. Schattka, M. Antonietti, R. A. Caruso, *J. Phys. Chem. B* **2003**, *107*, 952.

[67] A. L. Linsebigler, G. Lu, J. T. Yates, *Chem. Rev.* **1995**, *95*, 735.

[68] P. Arnal, R. J. P. Corriu, D. Leclercq, P. H. Mutin, A. Vioux, *J. Mater. Chem.* **1996**, *6*, 1925.

[69] C. C. Wang, J. Y. Ying, *Chem. Mater.* **1999**, *11*, 3113.

[70] J. Tang, J. Fabbri, R. D. Robinson, Y. M. Zhu, I. P. Herman, M. L. Steigerwald, L. E. Brus, *Chem. Mater.* **2004**, *16*, 1336.

[71] M. Niederberger, G. Garnweitner, F. Krumeich, R. Nesper, H. Cölfen, M. Antonietti, *Chem. Mater.* **2004**, *16*, 1202.

[72] G. Garnweitner, *Dissertation Universität Potsdam* **2005**.

[73] L. Bourget, R. J. P. Corriu, D. Leclercq, P. H. Mutin, A. Vioux, *J. Non-Crystalline Solids* **1998**, *242*, 81.

[74] R. J. P. Corriu, D. Leclercq, P. Lefevre, P. H. Mutin, A. Vioux, *J. Mater. Chem.* **1992**, *2*, 673.

[75] C. Feldmann, H. O. Jungk, *Angew. Chem. Int. Ed.* **2001**, *40*, 359.

[76] N. Uekawa, T. Kudo, F. Mori, Y. J. Wu, K. Kakegawa, *J. Colloid Interface Sci.* **2003**, *264*, 378.

[77] N. Pinna, M. Antonietti, M. Niederberger, *Colloids Surf., A* **2004**, *250*, 211.

[78] K. Kukli, M. Ritala, M. Leskela, *J. Electrochem. Soc.* **2001**, *148*, F35.

[79] M. A. Aegerter, *Sol. Energy Mater. Sol. Cells* **2001**, *68*, 401.

[80] A. Manthiram, J. Kim, *Chem. Mater.* **1998**, *10*, 2895.

[81] J. Livage, D. Ganguli, *Sol. Energy Mater. Sol. Cells* **2001**, *68*, 365.

[82] M. A. Aegerter, C. O. Avellaneda, A. Pawlicka, M. Atik, *J. Sol-Gel Sci. Tech.* **1997**, *8*, 689.

[83] H. Wong, C. V. Kim, V. A. Gritsenko, A. M. Badalyan, T. V. Perevalov, S. B. Erenburg, *J. Appl. Phys.* **2007**, 101.

[84] J. M. D. Coey, M. Venkatesan, P. Stamenov, C. B. Fitzgerald, D. L. S., *Phys. Rev. B* **2005**, *72*.

[85] H. P. a. A. Klug, *X-ray Diffraction Procedures for Polycrystalline and Amorphous Materials*, Wiley Interscience, New York, **1974**.

[86] A. Vioux, *Chem. Mater.* **1997**, *9*, 2292.

[87] R. Kodama, Y. Terada, I. Nakai, S. Komaba, N. Kumagai, *J. Electrochem. Soc.* **2006**, *153*, A583.

4 Syntheses of Metal Nitride Nanoparticles

4.1 Introduction

Metal nitrides are a class of functional materials with increasing importance, complementing metal oxides in many applications. However, reports on metal oxides outnumber nitrides by orders of magnitude, mainly due to the thermodynamic difficulties to make and break the nitrogen triple bond.[1] Similar to metal oxides, metal nitrides are characterized by an intriguing crystal chemistry, which leads to unique chemical and physical properties.[2-5] As a result, metal nitrides found diverse applications ranging from refractory ceramics (AlN, TaN, TiN,..),[6, 7] wear resistant coatings (TiN, ZrN, CrN, (Ti,Al)N, Zr_3N_4),[8-10] industrial catalysts (VN)[11] to semiconductor devices for optoelectronics (GaN, InN).[12, 13]

The size- and shape-dependent physical properties of semiconductors as well as the high surface-to-volume ratio are the major driving forces behind the synthesis of nanomaterials.[14-16] This is also true for metal nitrides, and in the last few years, great efforts have been made to achieve them as nanoparticulate materials. The reported synthesis procedures comprise a wide range of techniques, including hydrazide sol-gel synthesis,[17] microwave assisted combustion,[18] solvothermal routes,[19-25] nitridation or ammonolysis of molecular precursors,[26-31] various metathesis routes,[32-34] and chemical transformation of molecular precursors in solution.[35, 36] In some cases control over crystal growth was achieved by performing the reaction in the nanoconfinement of mesoporous materials like SBA-15[37, 38] or mpg-C_3N_4.[39]

4.2 Nonaqueous Synthesis of Indium Nitride as a Case Study for the Dependence of Particle Size on Precursors and Solvents

4.2.1 Introduction

Because of its properties of potential value in optoelectronic devices and other technologies, indium nitride has attracted increasing importance and attention in the last few years.[40] To avoid agglomeration in synthesis procedures requiring high temperatures, many reports regarding solution routes exist in the literature already. Nanocrystals of InN have been produced by the reaction of $InCl_3$ and Li_3N at 250 °C in xylene, but the obtained material was a mixture of hexagonal and cubic phases.[41] Hexagonal crystals with diameters in the range of 10-30 nm, and an absorption band around 1.9 eV, were obtained by the reaction of In_2S_3 and $NaNH_2$ in anhydrous benzene,[42] whereas they were tuned from 10 to 36 nm by varying the reaction conditions (time and temperature) when InI_3 was used as a precursor instead.[24] After reacting In_2S_3 in an aqueous solution with NH_4Cl at 250 °C 20 nm in size wurtzite InN nanoparticles were obtained.[22] A similar approach was also successful for GaN and AlN when the respective metal sulfide was used as a precursor. A solution-liquid-solid (SLS) process for the decomposition of azido precursors gave InN fibers around 20 nm in diameter, which were polycrystalline.[43] Additionally, Rao and coworkers have reported some solvothermal reactions towards the synthesis of InN in HMDS at 265 °C,[23] GaN from Ga cupferron/$GaCl_3$ in HMDS and/or toluene at 250 °C[44] and group III nitrides in general, starting from single-source precursors $[M(H_2NCONH_2)_6]Cl_3$ under a flow of nitrogen at 800 – 1000 °C.[45] In this subchapter we report solution routes towards the synthesis of nitride nanoparticles, where the size of the hexagonal phase InN nanoparticles from nonaqueous system of InX_3 (X=Cl, Br, I) and MNH_2 (M=Na, Li) was influenced by changing the type of non-oxygen containing anhydrous solvent.

4.2.2 Experimental

All synthesis procedures were carried out in a glovebox (O_2 and H_2O<0.1ppm). In a typical synthesis procedure, InN nanocrystals were prepared in a stainless steel autoclave with following solvents: toluene, mesitylene, xylene, tripehenylmethan (3PhM), p-xylene in ethylbenzene (p-Xyl in EthBenz), ethylbenzene (EthBenz) and diphenylether (DiPhEth). 3 mmol of $InCl_3$ powders were dispersed into 20 ml of the respective solvent and stirred for 20 min, and then stoichometric amount (9 mmol) of nitrogen source, namely $NaNH_2$, was introduced to the system (additionally few experiments with $InBr_3$ and InI_3 instead of $InCl_3$, and with $LiNH_2$ as nitrogen source were done. Most of the experiments are shown in Table 4.1) The mixture was transferred into an autoclave, taken out of the glovebox and finally heated in a furnace at 210 °C for 1 day. The resulting black suspensions were centrifuged in order to separate the precipitate from other undesired products. Excess organic and inorganic impurities were removed by repeated washing steps in ethanol and water, and dried in air at 60 °C.

4.2.3 Results and Discussion

X-Ray diffraction was used to verify the crystal structures and the phase purity of the obtained materials. A typical XRD pattern of the product prepared at 210 °C for 1 day is shown in Figure 4.1. All the peaks of the 100, 002, 101, 102, 110, 103, 112 and 201 reflections can be indexed to the pure hexagonal wurtzite InN with the lattice constants of a=3.537 Å and c=5.704 Å, consistent with the reported values of hexagonal InN (ICDD PDF No. 2-1450). The average crystallite size of the as-prepared nanaopowders, calculated by using Scherrer equation from the line broadening of the (101) diffraction peak (Figure 4.1) is a) 14 nm, b) 20 nm, c) 21 nm and d) 28 nm, respectively. Besides the InN reflections additional peaks appear, suggesting that these samples are not phase pure.

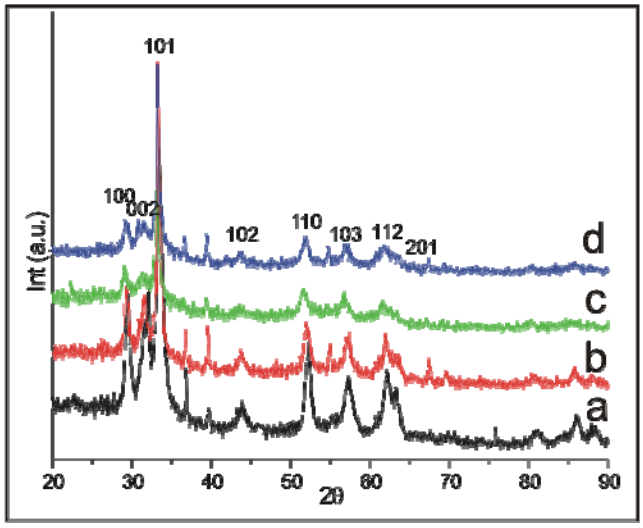

Figure 4.1 XRD patterns of InN nanocrystals synthesized in a) toluene, b) mesitylene, c) xylol and d) mixture of toluene and triphenylmethane.

In order to reveal the other phase in the systems, additional Rietveld refinement calculations were done for all of the samples. In Figure 4.2 Rietveld refinement of the sample obtained in mesitylene as a solvent is presented and provides further details of the structural parameters. A closer look at the difference curve between the experimental and the calculated XRD patterns proves much better agreement when the system was analyzed as a two phase system (Figure 4.2b). In this case numerical values of the weighted residual error (R_{wp}) equals 11.5%, whereas when the system was considered as one phase (Figure 4.2a) an R_{wp} value of 18 % was much higher and the value of goodness-of-fit indicator (GoF) is 1.3, corroborating the high quality of the fit. Weighted fractions of InN and In phases are 88.21 % and 11.79 %, respectively. Some experiments were done in the direction of phase purification in InN/In system, by applying either post-synthetic treatment to remove already formed metallic In (additional washing steps with HCl and HNO_3), or by changing the precursors and solvents to avoid the formation of metallic In. By doing these experiments either InN was not obtained because of the strong reducing agents resulting in only metallic In formation, moreover In_2O_3 was formed if any oxygen containing solvent was used, or we could only influence the size of the nanoparticles, which is the work presented here.

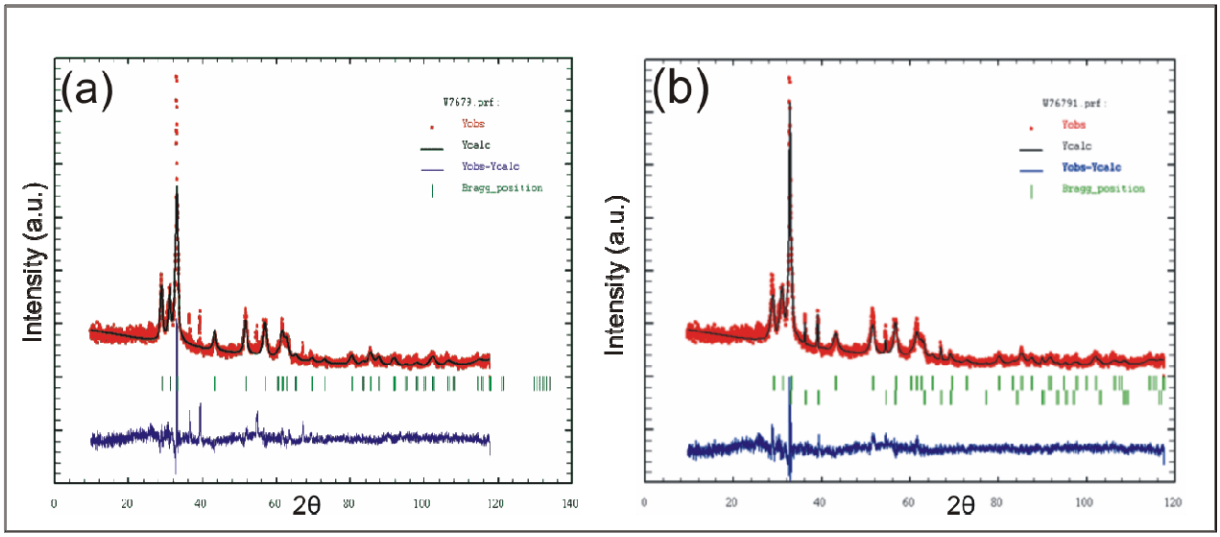

Figure 4.2 Experimental XRD patterns (red), calculated patterns (black) and difference curves (blue) of InN nanoparticles synthesized in mesitylene when the system was analyzed as a) one phase (InN) and b) two phase (InN/In) system. The green short vertical bars correspond to the calculated values of the positions of the Bragg reflections.

Since the samples synthesized in toluene and mesitylene showed the highest crystallinity (Figure 4.1, patterns a) and b)) these two samples were chosen to be studied in more details. EDX, TEM, HRTEM and SAED analyses of the as-synthesized InN nanoparticles are shown in Figure 4.3, for toluene as a solvent, and Figure 4.4, when mesitylene was the organic medium.

To prove that there are no other elements present besides Cu and C from TEM grid, and In and N from two phase InN/In system, EDX measurements were performed for both samples (Figure 4.3a and Figure 4.4a). Additionally, certain amount of oxygen is obtained, supposing due to the oxidation process towards forming of In_2O_3 as a thermodynamically preferred phase at the surface.

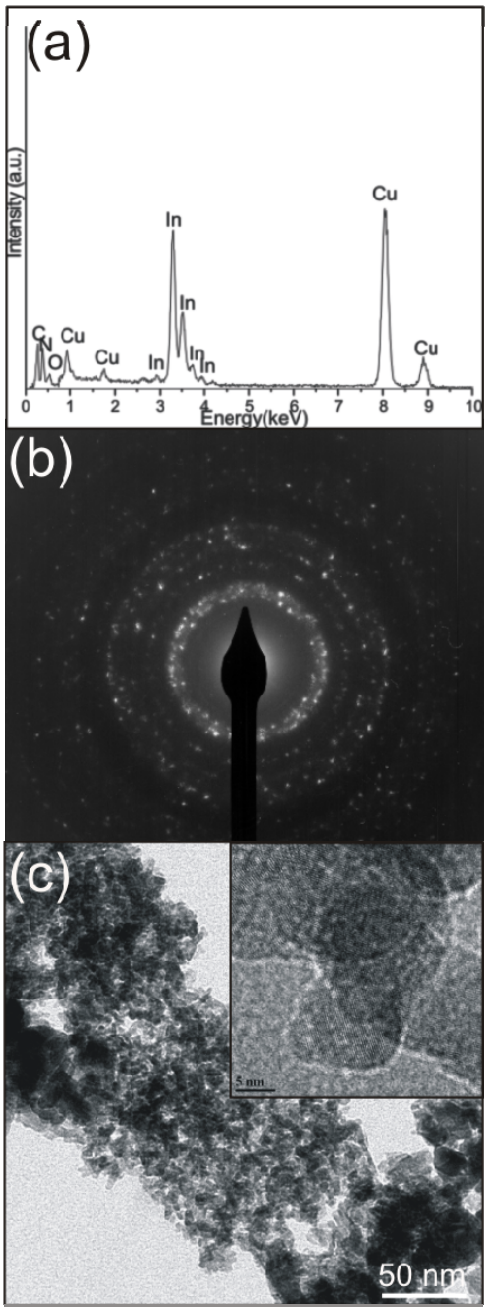

Figure 4.3 a) EDX spectrum, b) SAED pattern, c) TEM image and HRTEM image as inset for InN nanoparticles synthesized in toluene.

The selected area electron diffraction pattern of InN nanoparticles synthesized in toluene (Figure 4.3b) is characterized by Debye-Scherrer rings that are typical of a polycrystalline powder. This is in good agreement with XRD pattern and can be indexed according to the suggested wurtzite structure. Grain boundaries on TEM image (Figure 4.3c) are not well distinguishable due to the lack of the stabilizing agent, but a HRTEM image of such agglomerate shows well developed lattice fringes. (Figure 4.3c, inset).

Figure 4.4b provides a representative TEM overview image of the InN nanoparticles formed in mesitylene. Although the particles are slightly agglomerated, they are clearly distinguishable from each other. They exhibit nearly spherical and rather uniform particle morphology with an average diameter of about 20 nm, agreeing well with the Rietveld data. Transmission electron microscopy image proves that mesitylene as a solvent shows significant improvement regarding dispersibility of the InN nanoparticles achieved in comparison to the sample where toluene was used instead (Figure 4.3c). The HRTEM image in Figure 4.4c shows well-developed lattice fringes randomly oriented, going in all directions. Nevertheless, the lattice fringes of one nanoparticle show high crystallinity, giving rise to sharp spots in the power spectrum (Figure 4.4c, inset).

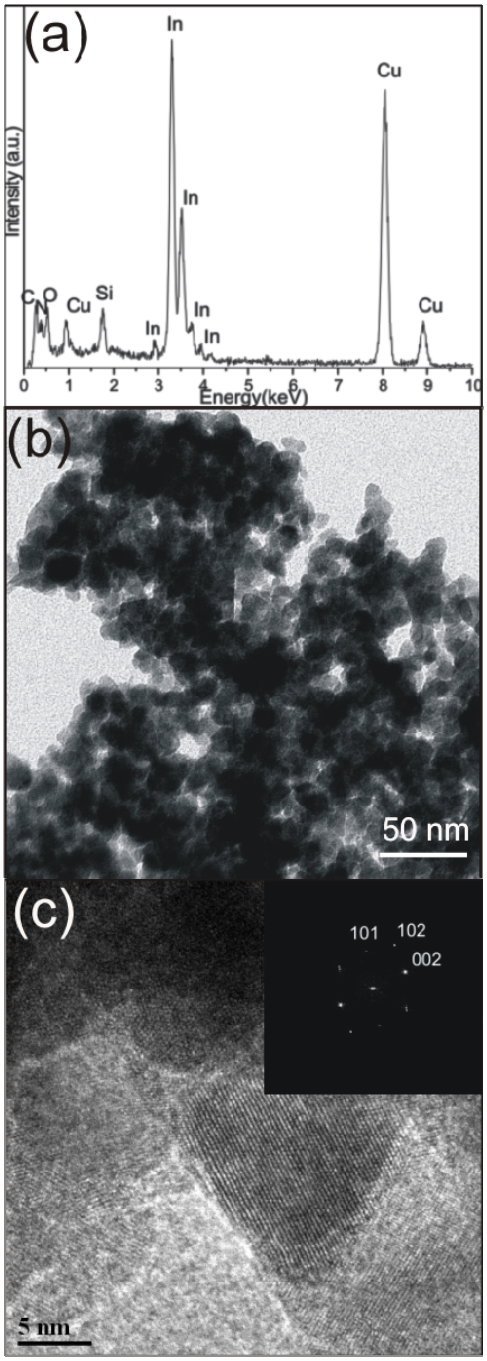

Figure 4.4 a) EDX spectrum, b) TEM image, c) HRTEM image and PS as inset for InN nanoparticles synthesized in mesitylene.

Besides these experiments, additional syntheses were done to study the influence of the solvents and the nitrogen sources, as presented in Table 4.1. Most of them failed completely, or the two phases of InN/In were found. In a few cases, other products were obtained, like in the case of $LiNH_2$ as nitrogen source. As much as solvents are concerned, we found that p-xylene in ethylbenzene (p-Xyl in EthBenz) independent of the precursor or the nitrogen source always resulted in the formation of pure metallic In, probably due to its strong reducing power. On the other hand when oxygen

containing solvents like ethylbenzene (EthBenz) or diphenylether (DiPhEth) were used, no InN was obtained, but only In_2O_3. The stable phase group III oxides are easier to form than their nitrides, even though the concentration of oxygen is undoubtedly much lower than that of nitrogen. It is also worth mentioning that besides the solvents, the precursors were influencing the size of the nanoparticles as well, when the synthesis procedures were successful. If $InBr_3$ was used with $NaNH_2$ in toluene, the size of the InN nanoparticles was increased to 20 nm, whereas when InI_3 was used instead, the average particle size was 25 nm. None of the systems is sensitive on temperature nor on the pressure. The size of the particles remained the same, when the temperature was increased up to 250 °C, and by increasing the amount of the respective solvent up to 70% of total autoclave volume, which was an important parameter in some other synthesis procedures, neither the one that were failures turned to be successful, nor the size of the InN nanoparticles was changed.

Table 4.1 Solvothermal reactions for the InX_3-MNH_2-Solvent System.

	Toluene	**Mesitylene**	**Xylene**	**Toluene +3PhM**	**p-Xyl in EthBenz**	**EthBenz**	**DiPhEth**
$InCl_3$+ $NaNH_2$	InN+In	InN+In	InN+In	InN+In	In	In_2O_3	In_2O_3
$InCl_3$+ $LiNH_2$	In+InN +In_xCl_y	In+InN +In_xCl_y…	In+InN +In_xCl_y	In+InN +In_xCl_y	In	In_2O_3	In_2O_3

A similar strategy was applied for GaX_3-MNH_2-solvent and AlX_3-MNH_2-solvent systems, but unfortunately WAXS measurements proved that none of these experiments were successful. However, our work indicates that at least in the case of gallium there are some indications for the formation of nanocrystalline particles, because powder XRD measurements yielded broad reflections characteristic of nanosized crystalline GaN domains. After 24h of reaction time, only two broad peaks were observed at 35° and 62° 2Theta (2θ). By increasing the tempering time the crystallinity could not be improved. But the obtained patterns resemble closely to the diffraction patterns published for GaN powders from poly(imidogallane).[35, 46, 47] On the other side PL emission from the as-prepared samples at room temperature didn't show any evidence of quantum confinement, neither in the visible range as reported before,[35] nor near the absorption edge.[36] There is still plenty of "space" left for

further exploration of the validity and generality of the solvothermal sol-gel approach for metal nitrides, as for improving the ones that were successful so far. Obviously, the number of reactions that were tried out is negligible in comparison to the possible combinations of many different metal nitride precursors, nitrogen sources and solvents.

4.2.4 Conclusions

This brings us to the conclusion that in the nonaqueous liquid-phase synthesis of metal nitride nanoparticles, similar to the nonaqueous synthesis of metal oxide nanoparticles, organic solvents do not only act as solvents, but they are influencing the size of the particles and their disperisbility. Unfortunately, we did not manage to prove that there might be a case where they could be donors of nitrogen as well, but this is the question of further research in this direction. It is really important to keep in mind that oxidation-reduction processes are crucial, because of the precursors that can be easily reduced to metallic indium. However the synthesis of metal nitride nanoparticles is quite restricted in comparison to the synthesis of metal oxide nanoparticles, because non-oxygen containing precursors and nitrogen sources, as well as solvents are required. Otherwise thermodynamically preferable oxides will be obtained instead. Finally, we did manage to tune the size of the InN nanoparticles by changing the solvents, which was the main goal. General conclusions are hard to draw because each metal system behaves differently and any successful method can not be directly applied for other group III nitrides. Although no solution route was found for the preparation of phase-pure metal nitride nanoparticles, some of the results are promising enough to continue the research in these directions.

4.3 Thermal Transformation of Metal Oxides into Metal Nitrides using Cyanamide, Urea and Melamine as Nitrogen Sources

4.3.1 Introduction

In spite of all the reports, the number and variety of nanocrystalline metal nitrides is still rather restricted, especially when compared to metal oxide nanoparticles. Therefore, it is obvious to use preformed metal oxides as precursors for the preparation of metal nitrides. First results in this direction, although starting from metal halides, were published more than 10 years ago by Kawaguchi et al.[48] The reaction of $AlCl_3$ with $[(C_3N_3)_2(NH)_3]_n$ at 1000 °C yielded AlN. The direct transformation of metal oxides is possible in the carbothermal reduction process.[49-54] In one approach, the metal oxides were reacted with carbon under nitrogen or ammonia.[49-53] The other route involved the reaction of Ga_2O_3 with $C_3N_{3.69}$ at 650 °C in an evacuated ampoule.[54] The GaN nanocrystallites were in the size range of 30-50 nm. Recently, the same authors simplified this reaction approach by exchanging $C_3N_{3.69}$ against melamine as nitrogen source, enabling the transformation of various bulk metal oxides like Ga_2O_3, Cr_2O_3, Al_2O_3, TiO_2, V_2O_5, Nb_2O_5 and Ta_2O_5 into the respective metal nitrides.[55] Depending on the precursor oxide, the reaction temperatures ranged from 650 °C to 1200 °C, and the metal nitrides had crystallite sizes of 20 to 100 nm. Other approaches based on the transformation of metal oxides into metal nitrides include plasma nitridation,[56] ammonolysis,[57-61] cyanonitridation using monomethylamine,[62] thermolysis under nitrogen,[63, 64] or reaction with sodium amide.[65] The process of transformation of metal oxides into metal nitrides can also end with oxynitride as in a case of niobium oxynitride.[66] The latter was prepared by a temperature-programmed synthesis method, consisting of passing NH_3/He over a commercial Nb_2O_5 oxide precursor at temperatures in the range from 1027 to 1173 K.

In this chapter, we report the thermal transformation of various metal oxide nanoparticles into nanocrystalline metal nitrides. Nanosized oxides of titanium, aluminum, gallium, vanadium, niobium, hafnium, tantalum, zirconium, zinc gallate and manganocolumbite were used as precursor materials and cyanamide, urea or melamine as nitrogen sources. The oxidic nanopowders were transformed into the metal nitrides upon heating them together in a crucible at 800 °C under nitrogen

atmosphere. For the first time, a detailed study is presented on the influence of the structural and morphological properties of the starting nanomaterials on the characteristics of the final metal nitrides. To correlate the particle size and shape of the starting metal oxides with the final nitrides we chose the following systems as instructive examples: i) nearly spherical anatase nanoparticles with crystallite sizes of about 5, 10 and 20 nm, respectively; ii) two types of vanadium oxide nanoparticles: isotropic V_2O_3 particles in the size range of 20-50 nm and anisotropic VO_x nanorods 20-50 nm wide and 150-250 nm long; iii) amorphous and crystalline tantalum oxide nanoparticles. Furthermore, the wide applicability of the synthesis approach was proven by the transformation of γ-Al_2O_3 nanocrystals to AlN, γ-Ga_2O_3 nanoparticles to GaN, Nb_2O_5 to $Nb_4N_{3.92}$, HfO_2 to Hf_2ON_2, ZrO_2 to ZrN, $ZnGa_2O_4$ and $MnNb_2O_6$ to respective solid solutions of GaN and NbN. The nitrogen sources were chosen according to literature, where the successful use of urea[45, 67, 68] and melamine[55] for the preparation of several binary and ternary metal nitrides and cyanamide for the synthesis of melem, a precursor for graphitic carbon nitride,[69] and g-C_3N_4 nanoparticles in mesoporous silica[70, 71] have recently been reported.

4.3.2 Experimental

Materials: Cyanamide (99%, Aldrich), urea (puriss, Riedel-de-Haen) and melamine (99%, Alfa Aesar) were used as received. The thermal transformation was performed in Nabertherm Multitherm N 7/H lab furnaces under nitrogen gas flow (4.0, Praxair).

Synthesis: In a typical procedure, 100 mg of the oxidic nanopowders were mixed with 2 g of cyanamide, urea or melamine and reacted at 800°C under nitrogen atmosphere. In selected cases (see main text), the temperature was increased to 900 °C. The oxidic nanopowders were synthesized according to previously reported procedures. 5 nm-sized TiO_2 was obtained from $TiCl_4$ and benzyl alcohol,[72] 10 nm-sized TiO_2 from titanium isopropoxide and acetophenone and 20 nm-sized TiO_2 from titanium isopropoxide and 2-butanone.[73] Ga_2O_3 was obtained from gallium acetylacetonate and either benzylamine, octylamine or a mixture of both solvents,[74] aluminum oxide from aluminum acetylacetonate and benzyl amine,[75] vanadium oxide nanorods from vanadium oxotrichloride and benzyl alchohol,[76] and V_2O_3 from vanadium oxotriisopropoxide and benzyl alcohol.[77] Crystalline tantalum, hafnium and niobium oxide were synthesized from the respective metal chlorides and benzyl

alcohol as reported in Chapter 3, whereas the amorphous tantalum oxide and crystalline hafnia, as well as crystalline niobia were obtained from respective transition metal ethoxide and benzyl alcohol.[78] ZrO_2 nanoparticles were obtained from zirconyl chloride, aqueous NH_3 solution and HNO_3 and used in transparent sol form.[79] Ternary oxides were synthesized from respective acetylacetonates and benzyl amine in case of $ZnGa_2O_4$[80] and from manganese acetylacetonate and niobium chloride in benzyl amine in case of $MnNb_2O_6$.[81]

Detailed synthesis procedures of transformation of metal oxides into metal nitrides:

TiN: 5 nm-sized TiO_2 (anatase, tetragonal, s. g. $I4_1/amd$) was obtained from $TiCl_4$ and benzyl alcohol (Figure 4.5 A, see Ref. 72), 10 and 20 nm-sized TiO_2 from titanium isopropoxide and acetophenone and 2-butanone, respectively (Figure 4.5 B and C, see Ref. 73). In a typical procedure 100 mg of the oxidic nanopowders were mixed with 2 g of cyanamide or urea and reacted at 800 °C for 3h under nitrogen atmosphere.

GaN: The gallium oxide nanoparticles were synthesized according to Ref. 74. The crystallite size was varied by exchange of benzylamine (Figure 4.5 D) against octylamine (Figure 4.5 F) or against a mixture of benzylamine and octylamine (Figure 4.5 E). GaN was obtained by reacting 100 mg of the gallium oxide nanopowders with 2 g cyanamide, urea or melamine at 800°C for 3h under nitrogen.

VN: Vanadium oxide nanorods (crystal structure not yet solved) were prepared from vanadium oxotrichloride and benzyl alcohol (Figure 4.5 M, see Ref. 76) and V_2O_3 (karelianite, trigonal, s. g. $R\text{-}3c$) from vanadium oxotriisopropoxide and benzyl alcohol (Figure 4.5 N, see Ref. 77). To get VN, 100 mg of vanadium oxide was mixed with 2 g of cyanamide, urea or melamine and reacted at 800 °C for 3h under nitrogen atmosphere.

TaN: Crystalline tantalum oxide (orthorhombic, s. g. $P2_12_12$) was synthesized from tantalum chloride and benzyl alcohol at 220 °C (Figure 4.5 L, See Chapter 3), whereas amorphous tantalum oxide was obtained from tantalum ethoxide and benzyl alcohol according to Ref. 78 (Figure 4.5 I). The reaction with urea, cyanamide or melamine was conducted at 900 °C for 6h in nitrogen.

AlN: Aluminum oxide was synthesized from aluminum acetylacetonate and benzylamine at 200 °C (Figure 4.5 O, see Ref. 75). The reaction with urea, cyanamide or melamine was conducted at 900 °C for 6h in nitrogen.

NbN and Hf_2ON_2: Crystalline niobium (TT-Nb_2O_5, hexagonal) and hafnium (monoclinic, s. g. $P2_1c$) oxides were synthesized from the respective chlorides and benzyl alcohol (Figure 4.5 G and H, see Chapter 3), or according to Ref. 78 (Figure 4.5 J and Figure 4.5 K, respectively). The nitrides were obtained by reacting 100 mg of the oxidic nanopowders with 2 g of cyanamide, urea or melamine at 900 °C for 6h under nitrogen.

ZrN: ZrO_2 sol was synthesized from zirconium chloride in NH_3, and treated afterwards with 1.5:1 HNO_3-to-metal ratio (Figure 4.5 R, Ref. 79). To get ZrN, 2 ml of zirconium oxide sol was mixed with 2 g of cyanamide, urea or melamine and reacted at 900 °C for 6h under nitrogen atmosphere.

GaN and NbN solid solutions: $ZnGa_2O_4$ nanoparticles were obtained from zinc and gallium acetylacetonates in benzyl amine at 200 °C (Figure 4.5 P, Ref. 80), whereas $MnNb_2O_6$ nanoparticles were synthesized from manganese acetylacetonate and niobium chloride in benzyl alcohol at 200 °C (Figure 4.5 Q, Ref. 81). To obtain respective alloys, 100 mg of the respective ternary oxide was mixed with 2 g of cynamide, urea or melamine and reacted at 900 °C for 6h under N_2 atmospere.

For all samples, the temperature was raised at a heating rate of 5.3 K/min from room temperature up to the reaction temperature, and kept there for a certain amount of time.

Table 4.2 Thermal transformation of metal oxides into metal nitrides.

	Cyanamide	**Urea**	**Melamine**	Figure 4.5
TiO_2_benzalcohol	TiN	TiN	TiN	**A**
TiO_2_acetophenone	TiN+TiO_2	TiN+TiO_2	TiN+TiO_2	**B**
TiO_2_2butanone	TiN+TiO_2	TiN+TiO_2	TiN+TiO_2	**C**
Ga_2O_3_bam	GaN	GaN	GaN	**D**
Ga_2O_3_bamoam	GaN	GaN	GaN	**E**
Ga_2O_3_oam	GaN	GaN	GaN	**F**
Nb_2O_5_etox	NbN	NbN	NbN+Nb_2O_5	**G**
HfO_2_etox	Hf_2ON_2	HfO_2	HfO_2	**H**
Ta_2O_5_etox	TaN	TaN+Ta_2O_5	TaN+Ta_2O_5	**I**
Nb_2O_5_cl	NbN	NbN	NbN+Nb_2O_5	**J**
HfO_2_cl	Hf_2ON_2	HfO_2	Hf_2ON_2	**K**
Ta_2O_5_cl	TaN+Ta_2O_5	TaN+Ta_2O_5	TaN+Ta_2O_5	**L**
V_2O_3 nanorods	VN	VN	VN	**M**
V_2O_3	VN	VN+V_2O_3	VN+V_2O_3	**N**
Al_2O_3	AlN	AlN	AlN	**O**
$ZnGa_2O_4$	GaN +..	GaN +..	GaN	**P**
$MnNb_2O_6$	NbN	NbN	NbN	**Q**
ZrO_2	ZrN	ZrN+ZrO_2	ZrN+ZrO_2	**R**

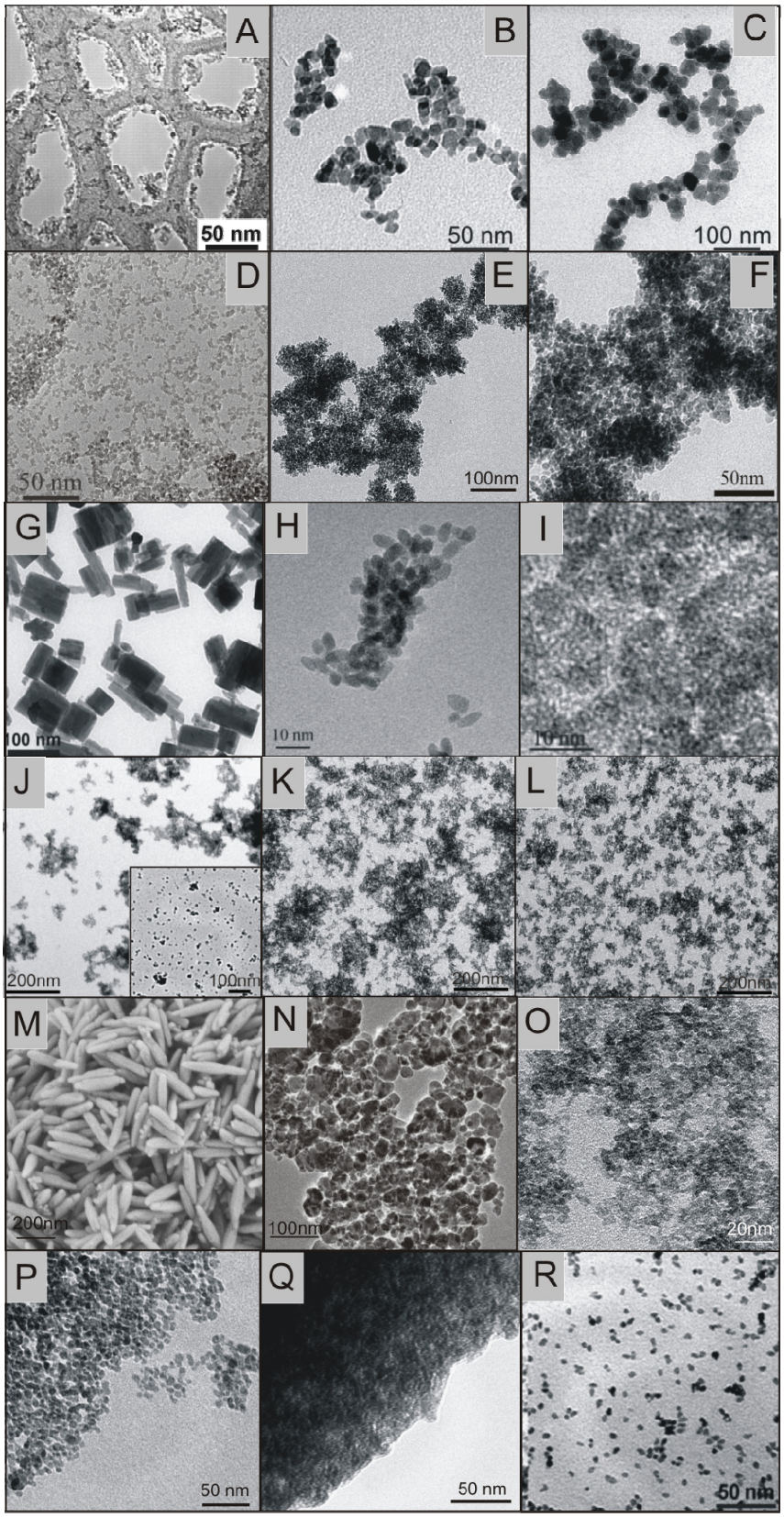

Figure 4.5 Overview of metal oxide nanoparticles used for the further thermal transformation

4.3.3 Results and Discussion

4.3.3.1 Binary oxides as precursors

The thermal transformation of TiO_2 nanoparticles provides a good opportunity to investigate whether there is a direct correlation of the crystallite size of the starting oxidic material with the final metal nitride particles. To achieve this objective, nanopowders consisting of anatase nanoparticles with average crystallite sizes of about 5, 10 and 20 nm were reacted with urea, melamine and cyanamide at 800 °C under nitrogen atmosphere. In general, 100 mg of the oxidic nanopowders were mixed with a large stoichiometric excess of 2 g of cyanamide, urea or melamine in a ceramic crucible. According to powder X-ray diffraction (XRD), only the anatase nanoparticles of 5 nm were completely transformed into TiN. In the case of TiO_2 with larger crystallite sizes of 10 and 20 nm, all nitrogen sources resulted in products with anatase impurities, however without formation of the thermodynamically stable rutile phase.

The large excess of cyanamide, urea or melamine leads to the problem that in addition to the metal nitride also a large amount of amorphous carbon is produced. As a matter of fact, elemental analysis of the TiN samples obtained from 5 nm-sized TiO_2 and cyanamide, urea or melamine showed a carbon content of about 20-25 wt%. This problem can be solved by adjusting the metal oxide-to-nitrogen source ratio. In the case of titanium, the best results, i.e., formation of titanium nitride without any oxidic residues, were achieved by reacting 100 mg anatase nanopowder with a crystallite size of 5 nm with 100.8 mg cyanamide, yielding titanium nitride nanoparticles with carbon content of about 2 wt%. Figure 4.6 gives an overview of the structural and morphological properties of the TiN nanoparticles obtained under these conditions. Figure 4.6a displays the experimental powder X-ray pattern together with the calculated pattern obtained from Rietveld refinement and the difference profile. The TiN nanoparticles are crystalline and the reflections can be indexed according to the cubic structure with the space group *Fm*-3*m* (ICDD PDF No. 38-1420). There is no indication for the presence of any other crystalline phase like remaining oxides. The very broad peak, which appears at around 28°, is an evidence of the presence of amorphous carbon as byproduct. The broad reflections point to small crystallite sizes. According to Rietveld refinement the volume-weighted average crystallite size amounts to 3 nm, which is confirmed by electron microscopy

investigations. Figure 4.6b provides a representative TEM overview image of the TiN nanoparticles. Taking the high temperature of the transformation reaction into account, the TiN nanoparticles are only slightly agglomerated. The TiN particles are quite uniform in morphology. The shape is nearly spherical, and the diameter of the individual nanoparticles is approximately 3 nm (Figure 4.6b, inset upper right). The nanoparticles form agglomerates with diameters of about 50 nm that are embedded in a matrix of amorphous carbon. Selected area electron diffraction of such an agglomerate exhibits Debye-Scherrer diffraction rings that can be indexed according to cubic TiN and that are typical of a polycrystalline powder (Figure 4.6b, lower left). There are no additional rings or spots in the SAED pattern stemming from any crystalline impurities. The crystallinity is further confirmed by HRTEM investigations. The HRTEM micrograph shows well-developed lattice fringes, which are randomly oriented with respect to each other (Figure 4.6c), confirming the SAED results. However, the corresponding power spectrum displayed in the inset of Figure 4.6c indicates, with respect to crystallinity, a two-component character of the TiN sample. The array of discrete spots corresponds to crystalline TiN nanoparticles (the 111 and 200 reflections are denoted), while the diffuse superimposed halo can be assigned to amorphous carbon.

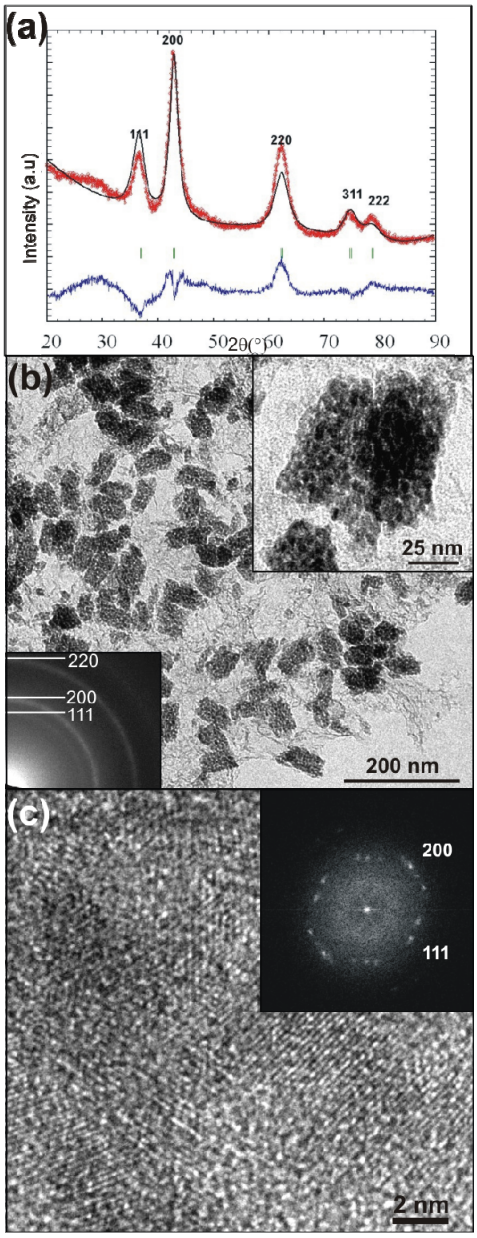

Figure 4.6 Titanium nitride nanoparticles obtained from 5 nm-sized anatase nanoparticles and cyanamide. a) Experimental XRD pattern (red), calculated pattern (black), difference curve (blue) and calculated values of the positions of the Bragg reflections (short green vertical bars). b) TEM overview image, inset upper right: TEM image at higher magnification, inset lower left: corresponding SAED pattern. c) HRTEM image of several nanoparticles together with the corresponding power spectrum as inset.

The transformation of vanadium oxide to vanadium nitride offers the possibility to investigate the influence of the particle morphology of the starting oxide onto the final shape of the nitride. Two different vanadium oxides were studied as vanadium nitride precursors. V_2O_3 is characterized by an isotropic crystallite shape with diameters in the range of 20-50 nm.[77] The second starting component exhibits an anisotropic, rod-like particle morphology with diameters of about 25-50 nm and lengths between

150 and 250 nm.[76] Both oxides were reacted with cyanamide, urea or melamine at 800 °C under nitrogen atmosphere. Whereas in the case of V_2O_3 only cyanamide was able to transform the oxide completely into the nitride, the vanadium oxide nanorods completely reacted to VN with cyanamide as well as with urea or melamine. This observation is rather surprising, as the vanadium oxide nanorods are considerably larger than the V_2O_3 nanoparticles. Obviously the nanorods are much more reactive towards the different nitrogen sources.

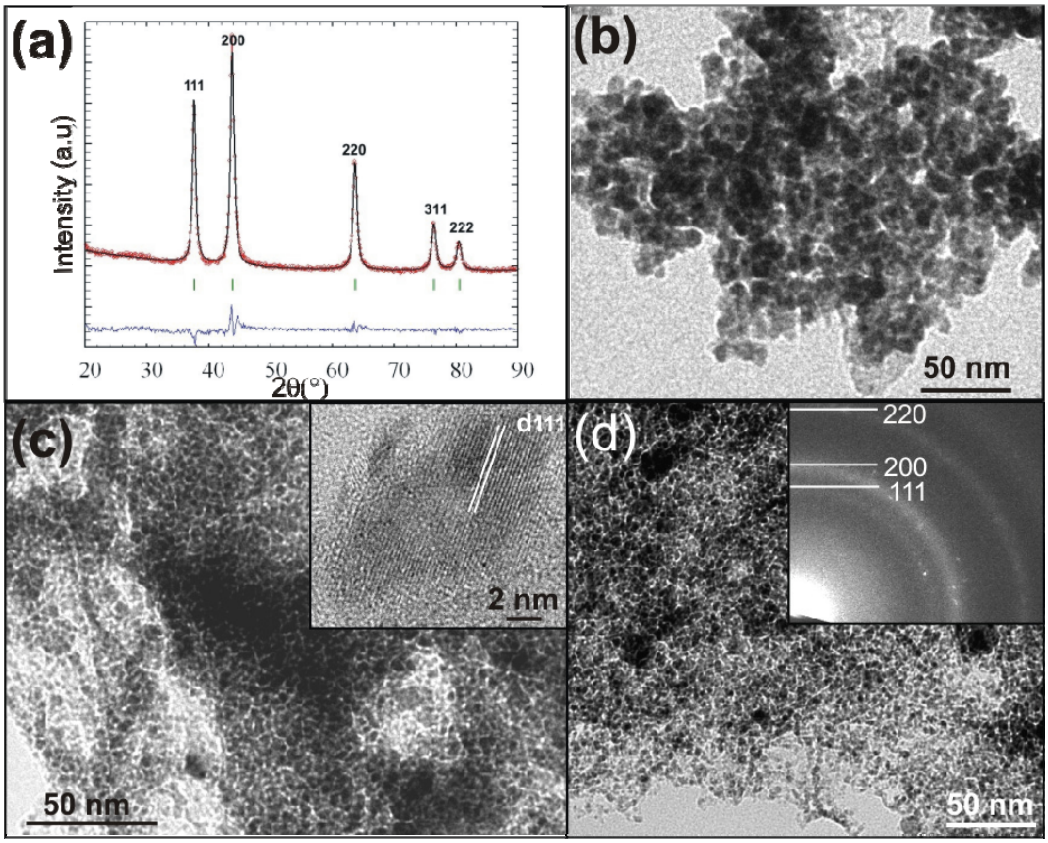

Figure 4.7 Vanadium nitride nanoparticles. a) Representative experimental XRD pattern (red), calculated pattern (black), difference curve (blue) and calculated values of the positions of the Bragg reflections (short green vertical bars). b) TEM overview image. Sample in a) and b) obtained from vanadium oxide nanorods and cyanamide. c) TEM overview image with HRTEM micrograph with the lattice indexing as inset of VN from vanadium oxide nanorods and urea. d) TEM overview image of VN from V_2O_3 and cyanamide with corresponding SAED pattern.

Figure 4.7 summarizes the structural and morphological features of the various vanadium nitride samples. The powder XRD pattern of VN synthesized from the vanadium oxide nanorods and cyanamide in Figure 4.7a proves the high crystallinity. All reflections can be assigned to VN (ICDD PDF No. 35-768) without any indication of other crystalline impurities. According to Rietveld refinement the volume weighted

average crystallite size amounts to 10.3 nm. The difference profile proves the good quality of fit. The crystallite size extracted from the XRD data is confirmed by TEM investigations. Figure 4.7b displays nanoparticles with sizes in the range of 8 to 15 nm. The VN nanoparticles obtained from the vanadium oxide nanorods with urea are considerably smaller. The TEM image in Figure 4.7c shows relatively uniform, nearly spherical particles with diameters of 5-10 nm. The well-developed lattice fringes observed in the HRTEM micrograph (Figure 4.7c, inset) confirm the high crystallinity. Although in these two cases the VN nanoparticles were obtained from an anisotropically shaped precursor, the morphology of the final product is spherical. The shape of the precursor particles is obviously not transferred to the final nanomaterials. If VN is prepared from V_2O_3 as precursor and cyanamide, the particle size is much larger than in the other two cases. The TEM image in Figure 4.7d depicts particles in the size range of 20-30 nm. The larger size of the VN nanoparticles prepared from the smaller precursor is presumably due to a dissolution-recrystallization mechanism, where smaller precursor particles dissolve faster and lead to the recrystallization of larger particles. Also, in the case of VN elemental analysis gave evidence for a carbon content of 15-25 wt% for all samples.

The transformation of tantalum oxides into nitrides was investigated mainly with respect to the role of the crystallinity of the precursor materials. Amorphous as well as nanocrystalline tantalum oxide were reacted with cyanamide, urea or melamine at 900 °C. In comparison to the other nitrides discussed above, tantalum oxides required a higher reaction temperature, and in contrast to all the other metal oxides, only amorphous tantalum oxide could be completely converted into tantalum nitride. In the following TaN nanoparticles prepared from amorphous tantalum oxide and cyanamide are presented. The powder XRD pattern in Figure 4.8a together with the Rietveld refinement illustrates the high crystallinity of the TaN sample. All reflections correspond to Fm-3m space group TaN (ICDD PDF No. 32-1283). The broadness of the peaks points to a small crystallite size, which is confirmed by Rietveld calculations that give a volume-weighted average crystallite size of 2.8 nm. The TEM overview image in Figure 4.8b displays nanoparticles that are rather uniform in size and shape. They are nearly spherical with diameters ranging from 1.7 nm to 6 nm. It seems as if there is no amorphous carbon present in the sample, which is confirmed by elemental analysis. The SAED pattern (Figure 4.8b, inset) shows Debye-Scherrer

diffraction rings typical for a polycrystalline powder. The rings can be assigned to the characteristic reflections (111), (200) and (220) of cubic TaN. The crystallinity is further confirmed by HRTEM investigations. Figure 4.8c shows well-developed lattice fringes. In addition to the crystallinity the type of nitrogen source is important in the case of TaN. Whereas cyanamide is able to transform the amorphous tantalum oxide completely into TaN, the product obtained in the presence of urea or melamine still contained oxidic residues.

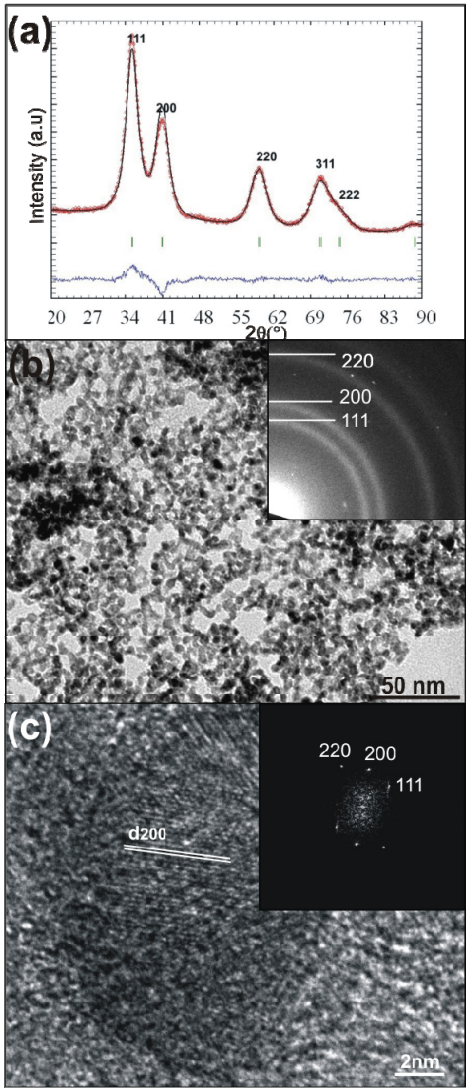

Figure 4.8 Tantalum nitride nanoparticles obtained from amorphous tantalum oxide and cyanamide. a) Experimental XRD pattern (red), calculated pattern (black), difference curve (blue) and calculated values of the positions of the Bragg reflections (short green vertical bars). b) TEM overview image, inset: corresponding SAED pattern. c) HRTEM image together with the corresponding power spectrum as inset and the lattice indexing.

The gallium oxide nanoparticles were obtained from gallium acetylacetonate either in benzyl amine,[74] octylamine or a mixture of both solvents. The crystallite shape of the γ-Ga_2O_3 is nearly spherical and the average crystallite size calculated from the XRD pattern by Scherrer equation varies from 2 nm (benzylamine) to 2.7 nm (benzylamine/octylamine) and 3.5 nm (octylamine). The gallium oxide nanoparticles are reacted with cyanamide, urea or melamine, similar to titania, at 800 °C under nitrogen. In the range of accessible crystallite sizes, all γ-Ga_2O_3 samples were completely transformed into GaN.

In the following, the conversion of 3.5 nm-sized γ-Ga_2O_3 in urea is discussed as representative example. Figure 4.9 displays the experimental X-ray diffraction pattern of GaN together with the calculated pattern obtained from Rietveld refinement and the difference profile. The reflections can be indexed according to the hexagonal phase of GaN (ICDD PDF No. 2-1078). No other crystalline by-products were found in the pattern, indicating that the as-prepared sample was pure GaN. The structural parameters from the Rietveld profile refinement are presented in Table 4.3. The volume weighted average crystallite size was calculated as 3.9 nm. Anisotropy in line broadening was not observed, so that the crystallite size is expected to be spherical. The extracted values of lattice parameters for the GaN nanoparticles are *a* = 3.197Å, *b* = 3.197Å, *c* = 5.198 Å. These values agree well with those obtained from the reported ICDD values for bulk GaN.

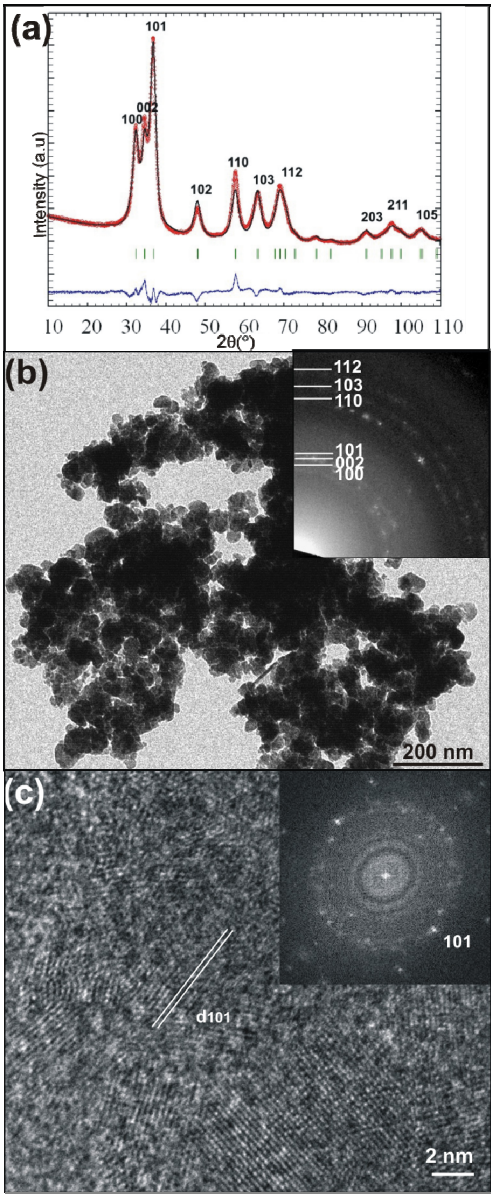

Figure 4.9 Experimental XRD pattern (red), calculated pattern (black) and difference curve (blue) of GaN. The green short vertical bars represent the calculated values of the positions of the Bragg reflections (ICDD PDF No. 2-1078). b) TEM overview image of GaN nanoparticles (inset: corresponding SAED pattern). c) HRTEM image of GaN with the corresponding PS as inset and the lattice indexing.

The morphological characteristics of GaN were investigated by TEM. A representative overview image in Figure 4.9b illustrates that the sample consists of nanosized GaN particles. Taking the reaction temperature of 800 °C into account, it is not surprising that the nanoparticles are agglomerated. Nevertheless, the grain boundaries are not clearly distinguishable, so that the diameter of the nanoparticles cannot be really determined. The HRTEM micrograph in Figure 4.9c presents lattice fringes that prove the crystallinity of the sample.

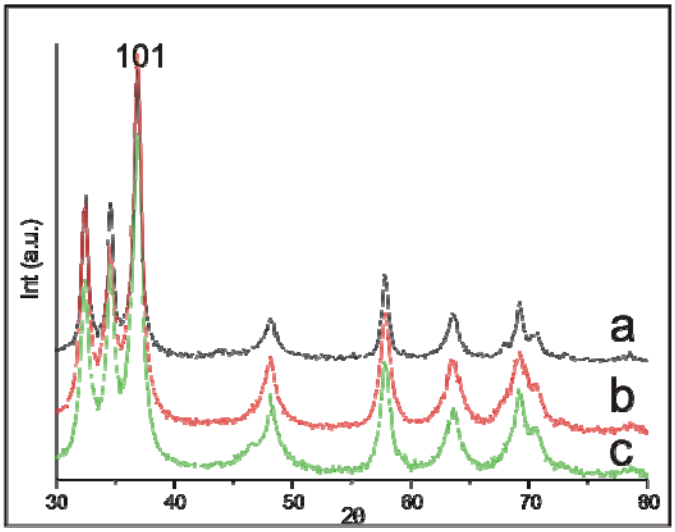

Figure 4.10 XRD patterns of GaN nanoparticles synthesized in Cyanamide starting from Ga_2O_3 nanoparticles synthesized in a) benzylamine, b) benzylamine/octylamine and c) octylamine, respectively

The three GaN samples obtained from the γ-Ga_2O_3 nanopowders with average crystallite size of 2, 2.7 and 3.5 nm, respectively, showed no significant difference in particle morphology. However, the crystallite sizes of GaN calculated from the 101 reflection by the Scherrer equation amounted to about 6, 5 and 4 nm, respectively (Figure 4.10). Similar to VN, the smallest gallium oxide nanocrystallites lead to the formation of the largest GaN crystallites. This observation once again points to a dissolution-recrystallization mechanism. Similar to tantalum nitride, however in contrast to all the other metal nitrides, GaN does not contain any carbon impurities as determined from elemental analysis.

Other metal oxides like aluminum, niobium and hafnium oxide nanoparticles are also suitable precursors for the preparation of the respective metal nitrides. Figure 4.11 provides an overview of some other metal oxides that can be transformed to the metal nitrides in the same way. In all these cases, the mixture of oxidic nanopowders with cyanamide, melamine or urea was heated to 900 °C to yield the respective metal nitrides. Figure 4.11a, c and e display the experimental X-ray diffraction pattern of the metal nitrides together with the calculated pattern obtained from Rietveld refinement and the difference profile. Again no other crystalline by-products were found. The structural parameters from the Rietveld profile refinement are presented in Table 4.3. The reflections can be indexed according to the hexagonal phase of AlN (ICDD PDF No. 44-106), cubic phase of NbN (ICDD PDF No. 76-263) and cubic phase of Hf_2ON_2

(ICDD PDF No. 88-669). According to the SAED pattern (inset Figure 4.11b) the AlN nanoparticles exhibit satisfying crystallinity. The clearly distinguishable grain boundaries make it possible to determine the diameter of the nanoparticles to 5-10 nm, which agrees well with the Rietveld refinement data. In the case of NbN, the crystallite size extracted from the XRD pattern (Figure 4.11c) is about 4 nm. The strongly agglomerated particles on the TEM image in Figure 4.11d do not allow a reasonable determination of the particle size. The SAED pattern (inset in Figure 4.11d) shows the characteristic (111) reflection of cubic NbN at 0.256 nm, in addition to the (200), (220) and (311) reflections. The experimental and calculated XRD patterns of Hf_2ON_2 in Figure 4.11e provide a volume weighted average grain size of 7 nm, which is in good agreement with the particle size observable on the TEM image in Figure 4.11f. The high crystallinity of the powder leads to well-pronounced Debye-Scherrer diffraction rings in the SAED pattern (Figure 4.11f, inset) that can be assigned to the reflections (222), (400), (440) and (622).

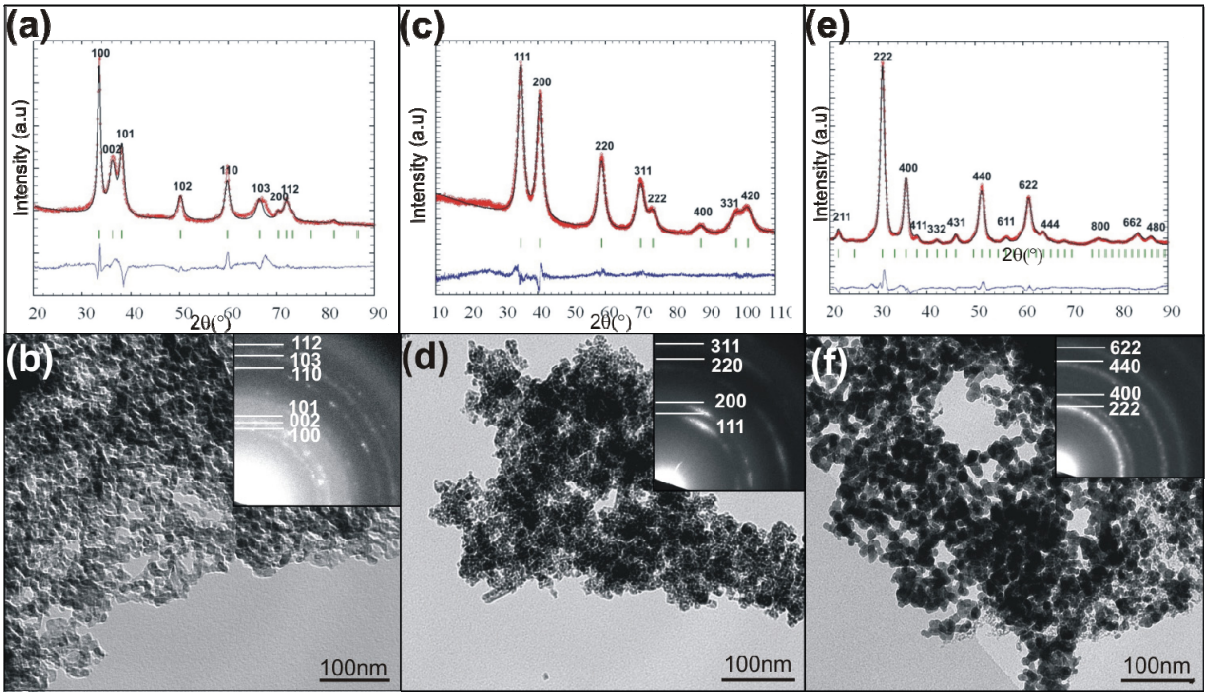

Figure 4.11 Experimental XRD pattern (red), calculated pattern (black) and difference curve (blue) of AlN (a), NbN (c) and Hf_2ON_2 (e), respectively. The green short vertical bars represent the calculated values of the positions of the Bragg reflections. TEM overview images with the corresponding SAED patterns as inset of AlN (b), NbN (d) and Hf_2ON_2 (f), respectively.

Table 4.3 Structural data and refinement parameters for all the nitrides calculated by Rietveld refinement of the experimental XRD powder patterns.

	TiN	***VN***	***TaN***	***GaN***	***AlN***	***NbN***	***Hf_2ON_2***	
Space group	*Fm-3m* (225)	*Fm-3m*	*Fm-3m*	$P6_3mc$	$P6_3mc$	*Fm-3m*	*Ia-3* (206)	
Crystal system	*cubic*	*cubic*	*cubic*	*hexagonal*	*hexagonal*	*cubic*	*cubic*	
Lattice parameter (Å)	4.216(3)	4.135(1)	4.416(1)	*a*=3.197(1) *c*=5.198(1)	*a*=3.095(1) *c*=4.961(2)	4.440(1)	10.060(1)	
Unit-cell volume ($Å^3$)	74.928	70.713	86.129	46.014	41.144	87.548	1018.4(3)	
M	Ti	V	Ta	Ga	Al	Nb	Hf1	Hf2
X	0.5	0.5	0.5	0.333	0.333	0	0	0.278(2)
Y	0.5	0.5	0.5	0.667	0.667	0	0	0
Z	0.5	0.5	0.5	0	0	0	0	0.25
N							N/O	
X	0	0	0	0.333	0.333	0.5	0.362(2)	
Y	0	0	0	0.667	0.667	0.5	0.136(2)	
Z	0	0	0	0.380	0.395	0.5	0.088(1)	
Volume-weighted average crystallite size (nm)	2.8	10.3	2.8	3.9	5.4	3.6	7	
Avarage microstrain e ($\times 10^4$)	7.8	16.1	17.7	9	4.2	10	68.1	
R_{wp} (%)	10.4	10.8	5.3	6.7	11.7	6.1	8.8	
R_B(%)	12.4	8.6	3.7	4.6	10.1	4.1	5.1	
GoF- index	1.3	1.6	1.8	1.5	1.8	1.8	41.7	

In a similar process, a ZrO_2 sol was transformed into ZrN nanoparticles. Powder X-ray diffraction pattern of the obtained zirconium nitride is shown in Figure 4.12a, confirming the pure cubic phase ZrN (ICDD PDF No. 35-753). In this procedure, when reacted with cyanamide as a nitrogen source the pure phase sample was obtained. When urea and melamine were used instead some oxidic residues were present as well. Further morphological characteristics of ZrN were investigated by TEM. A representative overview image in Figure 4.12b illustrates that the sample consists of nanosized ZrN. The lack of any surface protection layers results in some but negligible agglomeration. The average particle size is 15 nm according to TEM measurements, which is in good correlation with the average crystallite size calculated from the XRD pattern by Scherrer equation. In the inset of Figure 4.12b selected area electron diffraction (SAED) is presented. The lattice distances, measured from the diffraction rings, are in perfect agreement with the cubic structure

of ZrN. Figure 4.12c shows a HRTEM image of ZrN nanoparticles where the good crystallinity is once more confirmed. Detailed analysis on the lattice fringes gives an interplanar spacing of 2.6 Å, which matches well the (111) plane separation of the standard bulk cubic ZrN.

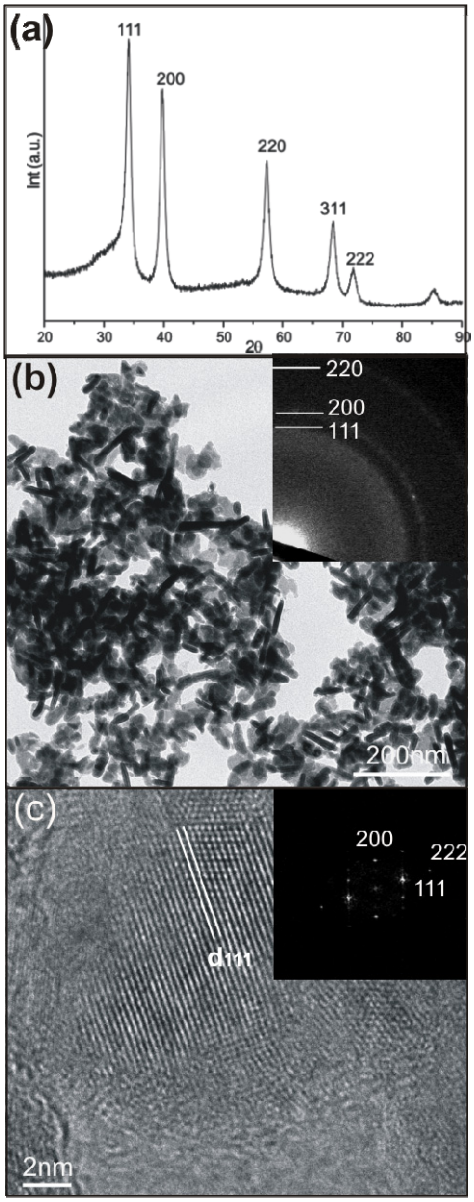

Figure 4.12 Experimental XRD pattern of ZrN (ICDD PDF No. 35-753). b) TEM overview image of ZrN nanoparticles (inset: corresponding SAED pattern). c) HRTEM image of ZrN with the corresponding PS as inset and the lattice indexing.

ZrN has found some interesting applications. At the moment, our material is under investigation in the following two directions:

1) Cu supported on Zr(O, N) materials for methanol chemistry, namely steam reforming to obtain hydrogen. After success with Cu-ZrO_2 and Cu-(Ce, Zr)O_2, now elucidating the effect of substitutions in the anion lattice on activity and selectivity is the goal.
2) Various Zr(O, $N)_2$ materials are known for decomposition of ammonia, or even ammonia synthesis. Employing the bulk catalysts that are capable of providing lattice nitrogen to the catalytic reaction, i.e. the lattice nitrogen migrates from bulk to the surface where it is used for the catalytic reaction.

4.3.3.2 Ternary oxides as precursors

The thermal transformation of zinc gallate ($ZnGa_2O_4$) into GaN solid solution and manganocolumbite ($MnNb_2O_6$) into NbN solid solution extends the thermal transformation route from binary to ternary oxides.

Figure 4.13a presents the XRD pattern of the material investigated after the reaction of $ZnGa_2O_4$ with melamine, whereas Figure 4.14a presents the XRD patterns of the end products obtained by the reaction of $MnNb_2O_6$ with (1) cyanamide, (2) urea and (3) melamine under nitrogen atmosphere as described in the experimental part. Additionally in both figures the XRD patterns of pure GaN (ICDD PDF No. 2-1078) and NbN (ICDD PDF No. 34-337) are presented, respectively, so that comparison to the pure sample of appropriate nitride can be evident (magnification of the comparison of the highest intensity peaks is given in inset). In both cases peaks were shifted in comparison to the pure phase system and EDX measurements proved that besides Ga (Nb), N and O, Zn (Mn) was present to a certain extent. Depending on the nitrogen source that was used the content of manganese ranges from 6 to 10 wt% (7.3 to 11.5 at%). In case of Nb-Mn system additional peaks are noticed, but the expecting oxide or nitride compounds of the respective metals were not revealed. This is simply attributed to the possible impurities.

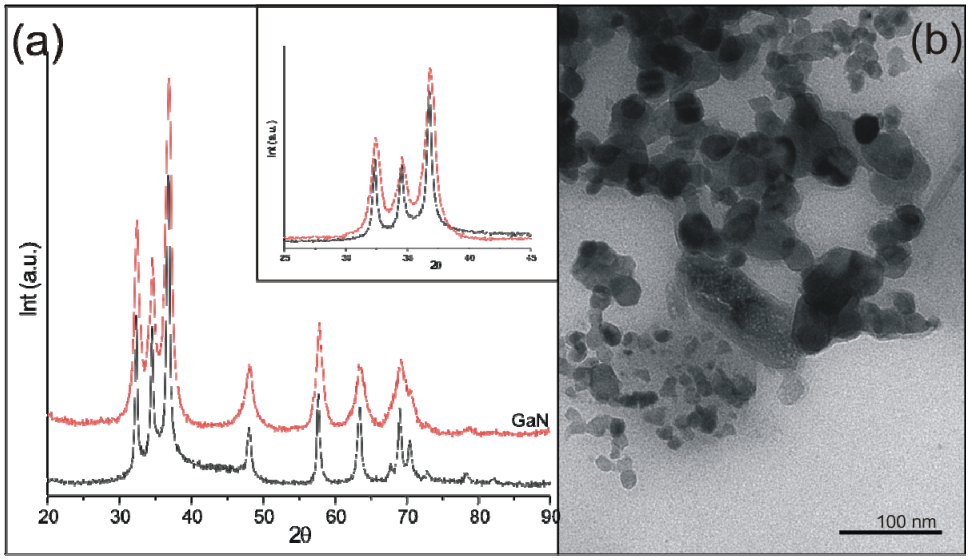

Figure 4.13 a) XRD pattern and b) TEM image of product synthesized by reaction of zinc gallate and melamine.

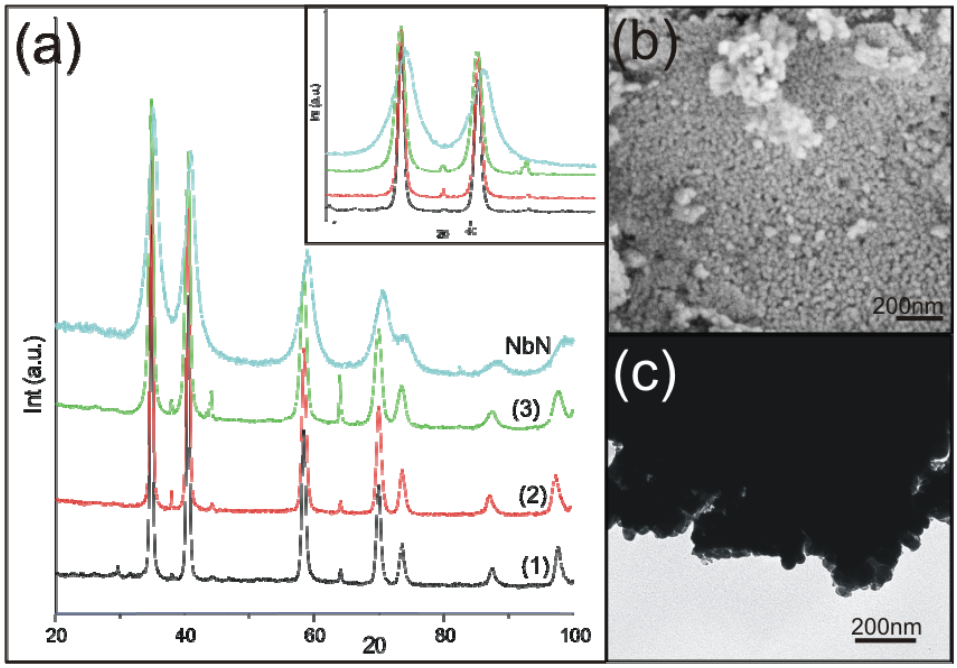

Figure 4.14 a) XRD patterns of products synthesized by reaction of manganocolumbite and (1) cyanamide, (2) urea and (3) melamine. b) SEM and c) TEM image of the sample (2)

Both systems were additionally characterized by electron microscopy techniques. In case of Ga-Zn system, particles were not uniform, but rather inhomogeneous and a small fraction of the sample featured noticeably larger particles, as illustrated in Figure 4.13b. However, grain boundaries were distinguishable and the size estimated to be in range from 8 to 48 nm. On the other hand in case of Nb-Mn system, SEM had to be applied instead (Figure 4.14b) because of the pronounced agglomeration

when TEM was used (Figure 4.14c), and one can realize that the particles are quite uniform in size and shape, being ca. 20 nm in diameter.

The more reactive metals present in ternary oxides (Ga in $ZnGa_2O_4$ and Nb in $MnNb_2O_6$) led towards formation of respective nitrides (GaN and NbN), as it might have been expected. However, the remaining metals (Zn and Mn) stayed in within the samples as confirmed by EDX. Maybe they have changed their structure, being rebuilt in the crystal structure of the obtained materials or they have formed an oxides' layer, but at least they do not show up as additional phase in XRD measurements. If we take in account the dissolution-recrystalization mechanism as it was already proposed in case of thermal transformation of binary oxides, we suggest that thermodynamically and quantitatively favorable nitrides were formed, but building up the less exposed metal inside the crystal structure, therefore shifting the respective peaks. This brings us to preliminary conclusion of solid-solution formation. However, many more characterization techniques have to be applied on presented systems in order to establish the exact crystal structure and composition of the nitrides formed and many more experiments in the field of thermal transformation of ternary oxides have to be done towards conclusions for the generality of the process.

4.3.3.3 Mixed oxides as precursors

After proving that binary as well as ternary oxides can be thermally transformed by using different nitrogen sources, and after concluding that the process is most likely driven by dissolution-recrystallization mechanism, one more possibility was tried out. Two different binary metal oxides were mixed in a proper ratio and a nitrogen source was added in order to obtain possible formation of ternary metal nitrides, oxo-nitrides or metal nitride alloys. Here we present the XRD patterns of two different combinations, namely TiO_2 and V_2O_3 reacted with cyanamide (Figure 4.15a) and a sample obtained by the reaction of Al_2O_3 and Ga_2O_3 with urea with a comparison of the end product with the pure phase GaN and AlN as an inset (Figure 4.15b).

In the case of TiO_2 and V_2O_3, the respective oxides were mixed in 2:1 molar ratio leading to a 1:1 ratio of the metals (the main idea was the formation of the ternary nitride $(Ti,V)N_2$). Unfortunately all these experiments, independent of the nitrogen source used, the combination of two metal oxides as starting materials, and of the

ratio of these oxidic precursors, were leading to two phase systems. In Figure 4.15a we can clearly see peaks of cubic VN (ICDD PDF No. 35-768), marked in black, and TiN (ICDD PDF No. 38-1420), marked in red color.

On the other hand by reacting Al_2O_3 and Ga_2O_3 (1:1 molar ratio) with any nitrogen source, thermodynamically preferable GaN phase was obtained. In the inset of Figure 4.15a comparison to both AlN (ICDD PDF No. 25-1133) and GaN (ICDD PDF No. 2-1078) hexagonal phase is shown, leading to the conclusion that AlN was not formed at all. Additional EDX measurements were done, showing that besides Ga and N, Al is also present, but much less then the ratio expected from the starting mixture. Besides the metals and nitrogen, also traces of oxygen were present, but this was the case for all the nitride compounds synthesized so far by thermal transformation using cyanamide, urea or melamine as nitrogen sources. Presumably, this oxygen is placed only at the surface of the respective samples, because no oxygen compound was detected by XRD. Here we could also assume possible solid solution formation as in the case of the ternary oxides. But in contrast to ternary oxides, the peak shift that was emphasized in the case of Ga-Zn and Nb-Mn systems is negligible here or even not present at all.

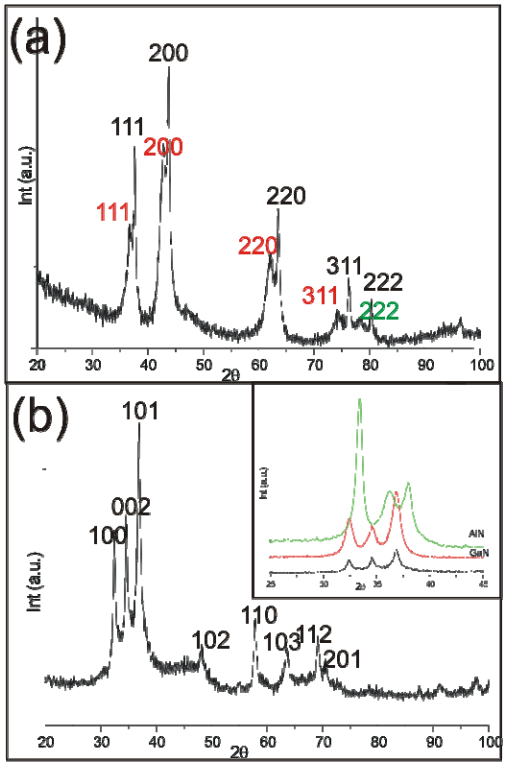

Figure 4.15 a) XRD pattern of sample obtained by reaction of TiO_2 and V_2O_3 with cyanamide. b) XRD pattern of sample obtained by reaction of Al_2O_3 and Ga_2O_3 with urea with comparison to the pure phase GaN and AlN as an inset.

4.3.4 Conclusions

The thermal transformation of metal oxide nanoparticles into metal nitrides was investigated with the focus on finding a correlation between the morphological and structural characteristics of the starting oxide nanoparticles with the final metal nitrides. Metal oxide nanoparticles with different particles sizes, shapes and degree of crystallinity were reacted with cyanamide or urea as nitrogen sources. However, general conclusions are difficult to draw because of the different reactivity of the various metal oxides towards the two nitrogen sources. For example, in the case of titania the upper crystallite size for complete transformation from the oxide to the nitride is less than 10 nm, whereas in the case of vanadium oxide, nanorods with sizes up to hundreds of nanometers react readily to the respective nitride. The degree of crystallinity seems to play a minor role for most of the metal oxides investigated. However, tantalum oxide only reacts to the metal nitride, if an amorphous nanopowder is used as starting material. Whereas, GaN and TaN do not show any indication for carbon impurities, all the other metal nitrides contain carbon in the range of 15-25 wt%. Nevertheless, one important general statement can be

made. In none of the investigated cases the morphology of the oxidic compound was transferred to the metal nitride, which means that the reaction pathway presumably proceeds along a dissolution-recrystallization process. Regarding the transformation of ternary oxides or mixtures of binary oxides more general statements are hard to make, because depending on the system and thermodynamical stability of the desired phase, either both nitrides or only one were formed. For some systems with pronounced shifts in the XRD reflections, strongly indicate the formation of solid solutions. However, this question needs to be addressed again in further investigations.

4.4 Thermal Transformation of Metal Oxides into Metal Nitrides using NH_3 flow

4.4.1 Introduction

Since the development of the first optoelectronic solid state device about 25 years ago there has been a continuous demand for efficient blue and UV light emitting materials. Because of their wide direct band gap, group III nitrides are commonly used in optoelectronic devices, such as high brightness light-emitting diodes[82] and low wavelength laser diodes (LDs),[83] as well as high power/high frequency electronic devices.[84, 85] Additionally, InN has some promising electronic and transport properties. From all the group-III nitrides it has the smallest effective electron mass ($0.07m_0$ and $0.14m_0$), leading to high mobility and high saturation velocity,[86] and a large drift velocity ($4.2x10^7$cm) at room temperature.[84, 85] Therefore, one can say that InN is very promising as a channel material in high-speed and high-frequency electron devices. However, because of its low decomposition temperature (the decomposition start was found consistently at 773K, under 1 bar of nitrogen)[87] and suggested metastable state even below room temperature, the synthesis of crystalline InN-containing materials is still rather challenging.

In contrast to the converging view about the optical properties of high quality films grown by CVD[88-90] or magnetron sputtering;[91] epilayers or nanorods using the most popular growth techniques like plasma-assisted molecular beam epitaxy (MBE)[92, 93] or metalorganic vapor beam epitaxy (MOVBE),[94, 95] where the absorption edge

energy was increased with decreasing film thickness and increasing aging time and annealing temperature[96] but still remaining in the ~0.8eV region, the reports on other InN materials are still controversial. Since it was shown that the sample with the band gap in the region of 1.8-2.1eV contained up to 20% of oxygen[97] previous reports about the 1.9eV band gap need to be reexamined.

Regarding the synthesis of InN nanoparticles, there are many reports based on different approaches as solution routes (see Chapter 4.2.1), decomposition of different precursors[43, 98, 99] or ammonolysis.[57, 59, 100-102] The morphology of oxidic precursors, namely metal oxide nanoparticles, was not transferred via thermal transformation using cyanamide, melamine or urea as nitrogen sources (Chapter 4.3) supposing dissolution-recrystalization process as presumable mechanism. Even if it would be so, because of its low degradation temperature InN could not be formed from In_2O_3 at the first place, because the used nitrogen sources start decomposing and providing the essential nitrogen for metal nitride formation at higher temperatures. On the other hand, solvothermal approach was not completely successful, because besides the InN nanoparticles, metallic indium was formed as additional phase regardless which precursor, nitrogen source or solvent were used (Chapter 4.2). As reported in Chapter 3, we could influence the size and the shape of In_2O_3 nanoparticles by varying the precursors and solvents in our nonaqueous approach. In this section we report their further thermal transformation under ammonia flow at 610 °C.

4.4.2 Experimental

All synthesis procedures of respective indium oxides were carried out as explained in Chapter 3.1. In a typical synthesis procedure, regarding specific reactions of oxide transformation, they were done at 610 °C in a Lenton 2416 Tube Furnace under flowing NH_3 gas (Air Products, anhydrous with < 200 ppm water) at a rate of 3l/min. The gas was further dried by passing it through dried molecular sieves before entering the tube furnace for reaction. The loosely powdered sample of In_2O_3 (less then 100mg) was placed in an alumina boat inside a silica tube furnace with approximately 15 cm hot zone in the middle and heated to 610 °C and kept there for 4h before cooling down to the room temperature.

4.4.3 Results and Discussion

Chemical reactions with ammonia have three main classes:[103]

1) Addition reactions, ”ammoniation” analogous to hydration
2) Substitution reactions, “ammonolysis” analogous to hydrolysis
3) Oxidation-reduction reactions

Ammonia has three H’s that can react to form amides, imides, or nitrides with electropositive metals, depending on the temperature and ammonia partial pressure of the system. To avoid formation of microcrystalline or even amorphous products under normal pressure special designed autoclaves and equipment such as ammonia line and glovebox are employed. It was already demonstrated that nanosized oxide powder was beneficial to the gas solid reaction and much finer powders of TiN and CrN could be obtained when respective nanocrystalline oxides were used as starting materials.[63, 104] Additionally, it was proven that commercially available In_2O_3 and $In(OH)_3$ led to InN quite broad in size distribution which may be a limiting factor towards applications.[100] Taking both remarks into account, two sets of nanocrystalline In_2O_3 samples were utilized in the present investigation and nitridation process is introduced to the system. For the first set, In_2O_3 nanoparticles synthesized from indium acetylacetonate and benzylamine, with crystallite size of 9 nm were used, and for the other one, the ones obtained in the reaction of indium isopropoxide and acetophenone, with average crystallite size of 17 nm were further subjected under ammonolysis (for detailed experimental synthesis of oxide nanoparticles see Chapter 3.2) The resulting powders were further investigated by XRD and TEM as presented below.

Figure 4.16a shows the powder XRD pattern of the In_2O_3 nanoparticles completely converted into hexagonal InN (ICDD PDF No. 2-1450). As we can see from the TEM micrograph of InN sample (Figure 4.16b), the crystallite size of the InN powder prepared by the nitridation of the In_2O_3 nanoparticles (Figure 4.16b, inset) in the stream of NH_3 is widely distributed and not as uniform. Nevertheless, grain boundaries are still distinguishable and the average size can be evaluated from 5 to 25 nm, whereas the average crystallite size from the (101) peak broadening was established to be 17 nm.

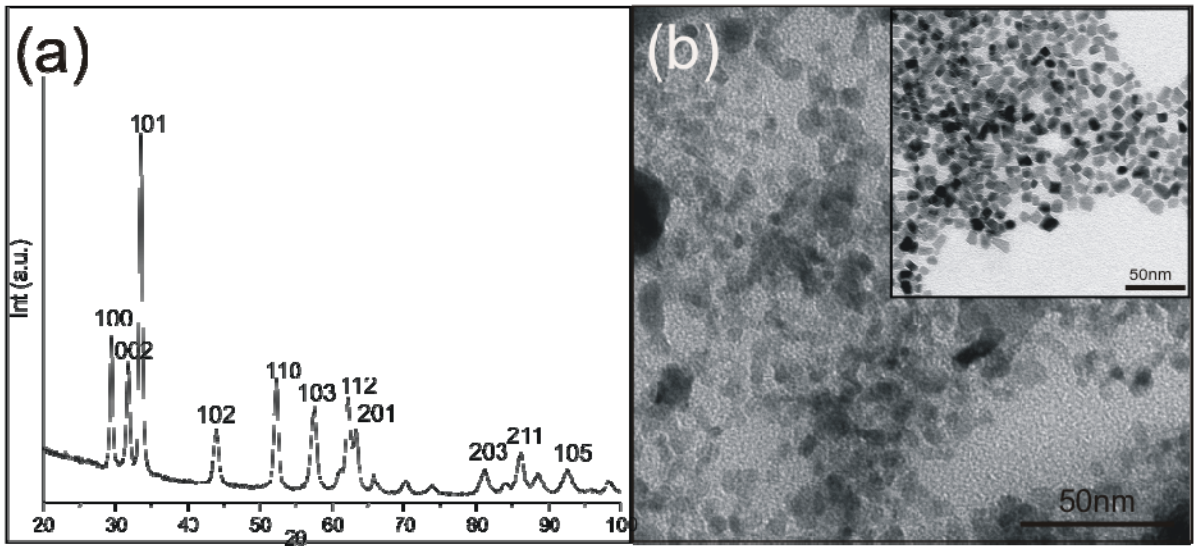

Figure 4.16 a) XRD pattern and b) TEM image of InN nanoparticles obtained by ammonolysis of In_2O_3 nanoparticles (inset) synthesized in benzyl amine

The conversion of In_2O_3 to InN is very sensitive to the nitridation temperature and reaction time. Considering previous reports where it was stated that the pure sample can be prepared only in a relatively narrow temperature range (580-620 °C), and if the temperature was higher the droplets of metallic indium were observed, both samples were transformed at 610 °C. However an additional effect is also the size of the starting oxidic nanopowder. After transforming In_2O_3 nanoparticles synthesized in acetophenone (average crystallite size of 17 nm), and noticeably bigger than the In_2O_3 nanoparticles synthesized in benzylamine (9 nm), the resulting product was pure phase tetragonal metallic indium (ICDD PDF No. 5-642). We assume that the complete reaction mechanism can be expressed as follows:

(1) $In_2O_3 + 2NH_3 = 2InN + 3H_2O$

Possible reaction mechanism is presented stepwise as follows:

(2) $In_2O_3 + 3H_2 = 2In + 3H_2O$

(3) $2In + N_2 = 2InN$

In case of the smaller In_2O_3 nanoparticles (Figure 4.16b, inset) they are faster reduced (2) and completely transformed (3) into InN. On the other side when the starting nanoparticles are bigger (Figure 4.17b, inset), the second step (3) of the nitridation process does not occur at all. Presumably, by increasing tempering time or temperature, the transformation towards nitride formation would happen at least to the certain extent. This is questioning of the future investigation in this direction, hopefully leading to more general conclusions. As we can see from the TEM of metallic indium sample (Figure 4.17b), the particles are quite nicely dispersed without

any agglomeration, and even spherical morphology is transformed from the starting indium oxide material (Figure 4.17b, inset). These discrete spherical particles are estimated from TEM image to be in the range from 25 to 80 nm. This is in reasonable good correlation with the results calculated from the (101) peak broadening using Scherrer equation, where the average crystallite size was estimated to be 62 nm.

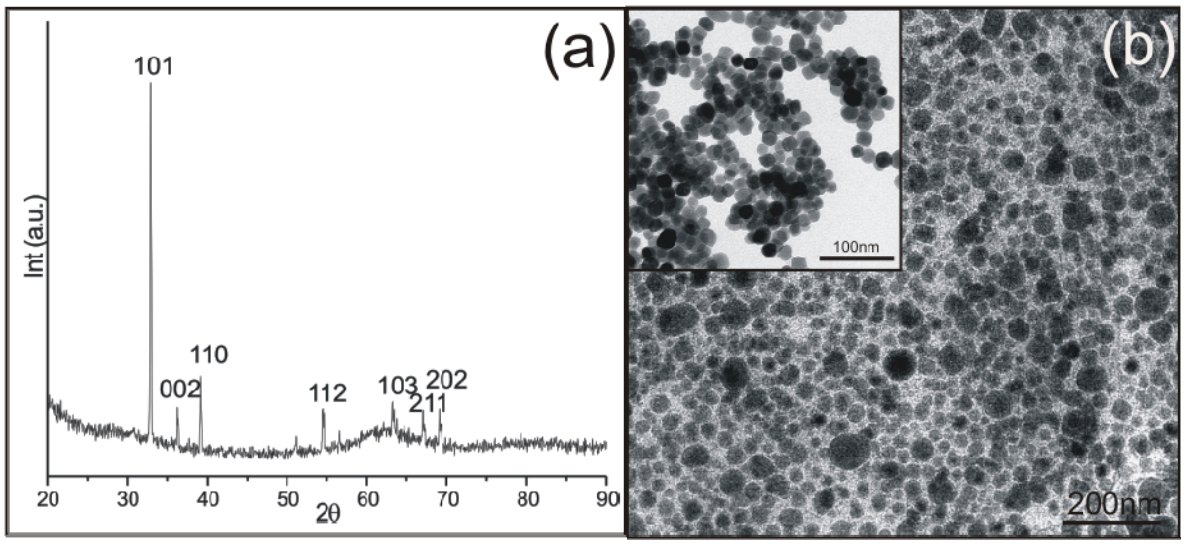

Figure 4.17 a) XRD pattern and b) TEM image of In nanoparticles obtained by ammonolysis of In_2O_3 nanoparticles (inset) synthesized in acetophenone

4.4.4 Conclusions

In this subchapter two samples of In_2O_3 were chosen and further transformed under ammonia flow in order to obtain pure phase InN nanoparticles. However, one of them led to pure phase metallic indium, but the other one was pure phase hexagonal InN. These experimental results demonstrate that the approach of nitriding In_2O_3 powders in situ is feasible for the synthesis of high-purity InN nanoparticles with good reproducibility and without catalyst materials. This is just a starting investigation concerning metal oxide nanoparticles synthesized via non-aqueous sol gel chemistry as starting materials, opening access to future work in the direction of their further transformation. Moreover, the presented strategy can probably also be applied to the synthesis of ternary group III-nitrides as well as InN in film form.

4.5 References

[1] D. H. Gregory, *J. Chem. Soc., Dalton Trans.* **1999**, *259*.

[2] N. E. Breese, M. O'Keeffe, *Structure and Bonding* **1992**, *Crystal Chemistry of Inorganic Nitrides, Springer*.

[3] R. Niewa, F. J. DiSalvo, *Chem. Mater.* **1998**, *10*, 2733.

[4] M. S. Miao, P. Lukashev, A. Herwadkar, W. R. L. Lambrecht, *Phys. Stat. Sol. C* **2005**, *2*, 2516.

[5] W. T. Zheng, C. Q. Sun, *Prog. Solid State Chem.* **2006**, *34*, 1.

[6] N. B. Dahotre, P. Kadolkar, S. Shah, *Surf. Interface Anal.* **2001**, *31*, 659.

[7] R. Schlesser, R. Dalmau, D. Zhuang, R. Collazo, Z. Sitar, *Jour. Cryst. Growth* **2005**, *281*, 75.

[8] I. Milosev, H.-H. Strehblow, B. Navinsek, *Thin Solid Films* **1997**, *303*, 245.

[9] S. PalDey, S. C. Deevi, *Mater. Sci. Eng., A* **2003**, *361*, 1.

[10] A. Zerr, R. Riedel, T. Sekine, J. E. Lowther, W.-Y. Ching, I. Tanaka, *Adv. Mater.* **2006**, *18*, 2933.

[11] S. T. Oyama, *Catal. Today* **1992**, *15*, 179.

[12] O. Ambacher, *J. Phys. D: Appl. Phys* **1998**, *31*, 2653.

[13] A. G. Bhuiyan, A. Hashimoto, A. Yamamoto, *J. Appl. Phys.* **2003**, *94*.

[14] A. Henglein, *Chem. Rev.* **1989**, *89*, 1861.

[15] M. L. Steigerwald, L. E. Brus, *Acc. Chem. Res.* **1990**, *23*, 183.

[16] A. P. Alivisatos, *J. Phys. Chem.* **1996**, *100*, 13226.

[17] I. Kim, P. N. Kumta, *J. Mater. Chem.* **2003**, *13*, 2028.

[18] B. Vaidhyanathan, D. K. Agrawal, R. Roy, *J. Mater. Res.* **2000**, *15*, 974.

[19] L. Grocholl, J. Wang, E. G. Gillian, *Chem. Mater.* **2001**, *13*, 4290.

[20] J. Xiao, Y. Xie, R. Tang, W. Luo, *Inorg. Chem.* **2003**, *42*, 107.

[21] S. Desmoulins-Krawiec, C. Aymonier, A. Loppinet-Serani, F. Weill, S. Gorsse, J. Etourneau, F. Cansell, *J. Mater. Chem.* **2004**, *14*, 228.

[22] Y. Xiong, Y. Xie, Z. Li, X. Li, R. Zhang, *New. J. Chem.* **2004**, *28*, 214.

[23] K. Sardar, C. N. R. Rao, F. L. Deepak, A. Govindaraj, M. M. Seikh, *Small* **2005**, *1*, 91.

[24] C. Wu, Y. Xie, T. Li, L. Lei, S. Hu, Y. Liu, *New. J. Chem.* **2005**, *29*, 1610.

[25] J. Choi, E. G. Gillian, *J. Mater. Chem.* **2006**, *16*, 3774.

[26] S. T. Barry, D. S. Richeson, *Chem. Mater.* **1994**, *6*, 2220.

[27] S. Kaskel, K. Schlichte, G. Chaplais, M. Khanna, *J. Mater. Chem.* **2003**, *13*, 1496.

[28] B. Schwenzer, C. Meier, O. Masala, R. Seshadri, S. P. DenBaars, U. K. Mishra, *J. Mater. Chem.* **2005**, *15*, 1891.

[29] A. W. Jackson, O. Shebanova, A. L. Hector, P. F. McMillan, *J. Sol. State Chem.* **2006**, *179*, 1383.

[30] D. Choi, G. E. Blomgren, P. N. Kumta, *Adv. Mater.* **2006**, *18*, 1178.

[31] M. G. Barker, M. G. Francesconi, P. M. O'Meara, C. F. Baker, *J. Alloys Comp.* **2001**, *317-318*, 186.

[32] J. Wang, L. Grocholl, E. G. Gillian, *Nano Lett.* **2002**, *2*, 899.

[33] L. Chen, Y. Gu, L. Shi, Z. Yang, J. Ma, Y. Qian, *Solid State Commun.* **2004**, *132*, 343.

[34] U. A. Joshi, S. H. Chung, J. S. Lee, *J. Sol. State Chem.* **2005**, *178*, 755.

[35] O. I. Micic, S. P. Ahrenkiel, D. Bertram, A. J. Nozik, *Appl. Phys. Lett.* **1999**, *75*, 478.

[36] G. Pan, M. E. Kordesch, P. G. Van Patten, *Chem. Mater.* **2006**, *18*, 5392.

[37] H. S. Hsueh, C. T. Yang, J. I. Zink, M. H. Huang, *J. Phys. Chem. B* **2005**, *109*, 4404.

[38] C. T. Yang, M. H. Huang, *J. Phys. Chem. B* **2005**, *109*, 17842.

[39] A. Fischer, M. Antonietti, A. Thomas, *Adv. Mater.* **2007**, *19*, 264.

[40] F. A. Ponce, D. P. Bour, *Nature* **1997**, *386*, 351.

[41] Y. J. Bai, X. G. X. Liu, D. L. Cui, X. P. Hao, X. Feng, Q. L. Wang, *J. Cryst. Growth* **2002**, *241*, 189.

[42] Y. Xie, Y. Qian, W. Wang, S. Zhang, Y. Zhang, *Science* **1996**, *272*, 1926.

[43] S. D. Dingman, N. P. Rath, P. D. Markowitz, P. C. Gibbons, W. E. Buhro, *Angew. Chem. Int. Ed.* **2000**, *39*, 8.

[44] K. Sardar, C. N. R. Rao, *Adv. Mater.* **2004**, *16*, 425.

[45] K. Sardar, C. N. R. Rao, M. Dan, B. Schwenzer, *J. Mater. Chem.* **2005**, *15*, 2175.

[46] J. F. Janik, R. L. Wells, *Chem. Mater.* **1996**, *8*, 2708.

[47] K. E. Gonsalves, S. P. Rangarajan, G. Carison, J. Kumar, K. Yang, M. Benaissa, M. Jose-Yacaman, *Appl. Phys. Lett.* **1997**, *71*, 2175.

[48] M. Kawaguchi, K. Nozaki, *Chem. Mater.* **1995**, *7*, 257.

[49] G. V. White, K. J. D. Mackenzie, J. H. Johnston, *J. Mater. Sci.* **1992**, *27*, 4287.

[50] G. V. White, K. J. D. Mackenzie, I. W. M. Brown, M. E. Bowden, J. H. Johnston, *J. Mater. Sci.* **1992**, *27*, 4294.

[51] G. V. White, K. J. D. Mackenzie, I. W. M. Brown, J. H. Johnston, *J. Mater. Sci.* **1992**, *27*, 4300.

[52] B. Vaidhyanathan, K. J. Rao, *Chem. Mater.* **1997**, *9*, 1196.

[53] X. Sun, Y. W. Zhang, R. Si, C. H. Yan, *Small* **2005**, *1*, 1081.

[54] H. Zhao, X. Chen, M. Lei, X. Yang, J. Jian, *J. Am. Chem. Soc.* **2005**, *127*, 15722.

[55] H. Zhao, X. Chen, M. Lei, W. Tang, *J. Mater. Chem.* **2006**, *16*, 4407.

[56] J. D. Houmes, H. C. Loye, *Chem. Mater.* **1996**, *8*, 2551.

[57] B. Schwenzer, L. Loeffler, R. Seshadri, S. Keller, F. L. Lange, S. P. DenBaars, U. K. Mishra, *J. Mater. Chem.* **2004**, *14*, 637.

[58] B. Schwenzer, J. Hu, R. Seshadri, S. Keller, S. P. DenBaars, U. K. Mishra, *Chem. Mater.* **2004**, *16*, 5088.

[59] S. D. Luo, W. Zhou, Z. Zhang, L. Liu, X. Dou, J. Wang, Z. Xiaowei, D. Liu, Y. Gao, L. Song, Y. Xiang, J. Zhou, S. Xie, *Small* **2005**, *1*, 1004.

[60] S. J. Henderson, A. L. Hector, *J. Solid State Chem.* **2006**, *179*, 3518.

[61] H. Chen, A. Nambu, W. Wen, J. Graciani, Z. Zhong, J. C. Hanson, E. Fujita, J. A. Rodriguez, *J. Phys. Chem. C* **2007**, *111*, 1366.

[62] F. Clement, P. Bastians, P. Grange, *Solid State Ionics* **1997**, *171*, 101.

[63] J. Li, L. Gao, J. Sun, Q. Zhang, J. Guo, D. Yan, *J. Am. Ceram. Soc.* **2001**, *84*, 3045.

[64] C. L. Dezelah, O. M. El-Kadri, M. J. Heeg, C. H. Winter, *J. Mater. Chem.* **2004**, *14*, 3167.

[65] Y. Huang, Y. Gu, M. Zheng, Z. Xu, W. Zeng, Y. Liu, *Mater. Lett.* **2006**.

[66] V. Schwartz, S. T. Oyama, *Chem. Mater.* **1997**, *9*, 3052.

[67] A. Gomathi, C. N. R. Rao, *Mater. Res. Bull.* **2006**, *41*, 941.

[68] A. Gomathi, *Mater. Res. Bull.* **2007**, *42*, 870.

[69] B. Jurgens, E. Irran, J. Senker, P. Kroll, H. Muller, W. Schnick, *J. Am. Chem. Soc.* **2003**, *125*, 10288.

[70] M. Groenewolt, M. Antonietti, *Adv. Mater.* **2005**, *17*, 1789.

[71] F. Goettmann, A. Fischer, M. Antonietti, A. Thomas, *Angew. Chem. Int. Ed.* **2006**, *45*, 4467.

[72] M. Niederberger, M. H. Bartl, G. D. Stucky, *Chem. Mater.* **2002**, *14*, 4364.

[73] G. Garnweitner, M. Antonietti, M. Niederberger, *Chem. Commun.* **2005**, 397.

[74] N. Pinna, G. Garnweitner, M. Antonietti, M. Niederberger, *J. Am. Chem. Soc.* **2005**, *127*, 5608.

[75] S. Zhou, M. Antonietti, M. Niederberger, *Small* **2007**, *3*, 763.

[76] M. Niederberger, M. H. Bartl, G. D. Stucky, *J. Am. Chem. Soc.* **2002**, *124*, 13642.

[77] N. Pinna, M. Antonietti, M. Niederberger, *Colloids Surf., A* **2004**, *250*, 211.

[78] N. Pinna, G. Garnweitner, M. Antonietti, M. Niederberger, *Adv. Mater.* **2004**, *16*, 2196.

[79] A. S. Deshpande, N. Pinna, P. Beato, M. Antonietti, M. Niederberger, *Chem. Mater.* **2004**, *16*, 2599.

[80] M. Cao, I. Djerdj, M. Antonietti, M. Niederberger, *Chem. Mater.* **2007**, *19*, 5830.

[81] L. Zhang, G. Garnweitner, I. Djerdj, M. Antonietti, M. Niederberger, *Asian J. Chem. submitted* **2007**.

[82] Y. C. Shen, J. J. Wierer, M. R. Krames, M. J. Ludowise, M. S. Misra, F. Ahmed, A. Y. Kim, G. O. Mueller, J. C. Bhat, S. A. Stockman, P. S. Martin, *Appl. Phys. Lett.* **2003**, *82*, 2221.

[83] S. Nagahama, T. Yanamoto, M. Sano, T. Mukai, *Appl. Phys. Lett.* **2001**, *79*, 1948.

[84] S. K. O'Leary, B. E. Foutz, M. S. Shur, U. V. Bhapkar, L. F. Eastman, *J. Appl. Phys.* **1997**, *83*, 826.

[85] E. Bellotri, B. K. Doshi, K. F. Brennan, J. D. Albrecht, P. P. Ruden, *J. Appl. Phys.* **1999**, *85*, 916.

[86] S. N. Mohammad, H. Morkoc, *Prog. Quantum Electron* **1996**, *20*, 361.

[87] B. Onderka, J. Unland, R. S. Fetzer, *J. Mater. Res.* **2002**, *17*, 3065.

[88] H. Wang, Y. Huang, Q. Sun, J. Chen, J. J. Zhu, L. L. Wang, Y. T. Wang, H. Yang, M. F. Wu, Y. H. Qu, D. S. Jiang, *Mater. Lett.* **2007**, *61*, 516.

[89] S. C. Shi, C. F. Chen, G. M. Hsu, J. S. Hwang, S. Chattopadhyay, Z. H. Lan, K. H. Chen, L. C. Chen, *Appl. Phys. Lett.* **2005**, *87*.

[90] J. W. Yoon, S. S. Kim, H. Cheong, H. C. Seo, S. Y. Kwon, H. J. Kim, Y. Shin, E. Yoon, Y. S. Park, *Semicond. Sci. Technol.* **2005**, *20*, 1068.

[91] X. D. Pu, Z. Shen, Z. Q. Zhang, *Appl. Phys. Lett.* **2006**, *88*.

[92] S.-H. Shen, H.-Y. Chen, H.-W. LIn, S. Gwo, A. A. Klochikhin, V. Y. Davydov, *Appl. Phys. Lett.* **2006**, *88*.

[93] G. Shikata, S. Hirano, T. Inoue, M. Orihara, Y. Hijikata, H. Yaguchi, H. Yoshida, *Jour. Cryst. Growth* **2007**, *301-302*, 517.

[94] A. Yamamoto, K. Sugita, H. Takatsuka, A. Hashimoto, V. Y. Davydov, *Jour. Cryst. Growth* **2004**, *261*, 275.

[95] T. Matsuoka, H. Okamoto, M. Nakao, H. Harima, E. Kurimoto, *Appl. Phys. Lett.* **2002**, *81*, 1246.

[96] Motlan, E. M. Goldys, T. L. Tansley, *Jour. Cryst. Growth* **2002**, *241*, 165.

[97] V. Y. Davydov, *Phys. Stat. Sol. B* **2002**, *234*, 787.

[98] P. S. Schofield, W. Zhou, P. Wood, I. D. W. Samuel, D. J. Cole-Hamilton, *J. Mater. Chem.* **2004**, *14*, 3124.

[99] R. A. Fischer, H. Sussek, A. MIehr, H. Pritzkow, E. Herdtweck, *J. Organomet. Chem.* **1997**, *548*, 73.

[100] L. Gao, Q. Zhang, J. Li, *J. Mater. Chem.* **2003**, *13*, 154.

[101] J. Zhang, L. Zhang, X. Peng, X. Wang, *J. Mater. Chem.* **2002**, *12*, 802.

[102] R. Garcia, G. A. Hirata, M. H. Farias, J. McKittrick, *Mater. Sci. Eng., B* **2002**, *90*, 7.

[103] B. Wang, M. Callahan, *Cryst. Growth Des.* **2006**, *6*, 1227.

[104] Y. Li, L. Gao, J. Li, D. Yan, *J. Am. Ceram. Soc.* **2002**, *85*, 1294.

5 Conclusions and Outlook

In the present thesis, the concept of fabricating metal oxide and metal nitride nanoparticles by nonaqueous synthesis approach was subjected to a systematic investigation. The nanosized materials of particles sizes in the range between 3 nm to 80 nm were achieved using different precursors, solvents and synthesis procedures.

In the first part of this work, our studies demonstrated that particle size can be tuned like in case In_2O_3 where various combinations of metallic precursors and organic solvents at the same synthesis conditions were leading towards the formation of cubic indium oxide nanoparticles not only tuned in size, but also with different morphology. On the other hand, when acetonitrile was used as non-oxygen containing solvent it induced mesocrystal assembly in case of ZnO, although the underlying details of the process and mechanism behavior are difficult to assess. The success in case of TiO_2 nanoparticles formation once more proves generality of the process itself, indicating that the solvent can be even solid at room temperature, and at the same time opening access to many more possible further combinations. Hence the general avoiding of metal halides as precursors, we did manage to synthesize high quality transition metal oxides and prove that there are no halide impurities that might hamper possible applications. Based on these experimental results it can be concluded that the present study also provided more insights into fine details of sol-gel synthesis of metal oxide nanoparticles in general and well dispersibility of the as synthesized powders as well as self-assembly in case of ZnO. As seen by the nonaqueous sol-gel approach, observed in the present and previous studies, the successful fabrication of metal oxide nanoparticles cannot be regarded as a simple

procedure, but needs a fine balance of various parameters such as type and purity of starting materials, temperature, tempering time etc.

Regarding the accurate characterization, we obtained a comprehensive and accurate particles size analysis over the complete spectra of samples. The particle size distributions calculated by using Scherrer equation were in good agreement with the TEM results in general. Further studies such as effect of the mechanism on the formation of different particle size and shape would be possible by studying so far not investigated systems and probably will be together with already investigated ones a topic of a future work.

The second part of the thesis was dedicated to the generation of metal nitride nanoparticles. This part is divided into few subsections:

- nonaqeuous sol-gel approach,
- thermal transformation of metal oxides under N_2 flow using cyanamide, urea and melamine as nitrogen sources, and
- thermal transformation of metal oxides under NH_3 flow.

First strategy was chosen according to the findings of first part on corresponding powder materials to obtain materials which would be more advantageous in application-wise. The synthesis of metal nitride nanoparticles is quite restricted in comparison to the one towards synthesis of metal oxide nanoparticles because non-oxygen containing precursors, nitrogen sources as well as organic mediums are required. System is sensitive, because otherwise thermodynamically preferable oxides will be formed instead. However we did manage to tune size of InN nanoparticles by changing solvents and prove that organic solvents play role not only as synthesis media, but influencing size of the formed nanoparticles and their dispersibility. On the other hand, as a main advantage compared to previous studies, the advanced thermal transformation shows generality of the approach in case when different nitrogen sources were used and morphology transformation when NH_3 flow was used instead. Diverse characterization techniques confirmed metal nitride formation. More importantly, thermal transformation using different nitrogen sources enabled to study possible formation mechanism and draw crucial and advantageous conclusions. Although more detailed studies are required, these preliminary ones

resulted suggest that “dissolution-recrystalization mechanism” for nanoparticles formation. On the opposite, when NH_3 flow was used InN was obtained and access to further investigations is opened because most probably it is possible to transfer morphology of the starting oxide nanoparticles. These results clearly demonstrate that the “connectivity” of complex systems bears more subtleties than the mere geometric description. Furthermore, the presented methods are allowing even choosing an appropriate synthetic route depending on the final requirements.

The aim is to combine the properties of crystalline material and enhanced properties that small size of the nanoparticles would bring to the material. It was shown that preparation of metal nitride nanoparticles requires combination of comprehensive knowledge on the formation of such structures, oxygen free synthesis conditions and as well as the properties of that particular crystalline material i.e., crystallization behavior. Thus, probably it is difficult to get a general picture how to achieve crystalline metal oxide and metal nitride nanoparticles since almost each metal has its own crystallization behavior with respect towards oxide/nitride formation and procedures should be optimized accordingly. Nevertheless, such materials could prove themselves useful in outnumbered applications. Related to that topic, a further work can involve the preparation of other metal oxides and metal nitrides with emphasis on their possible applications. Such studies might be useful in combining omnipresent properties of metal oxides and metal nitrides and that these approaches do not solely lead to well dispersed particles but are actually advantageous in terms of applications.

Symbols and Abbreviations

Analytical and Synthetic Methods

XRD.....X-Ray Diffraction
WAXS……..Wide Angle X-Ray Scattering
TEM.....Transmission-Electron Microscopy
HRTEM.....High Resolution Transmission-Electron Microscopy
SEM.....Scanning-Electron Microscopy
STEM.....Scanning-Transmission Electron Microscopy
EDX……...Energy Dispersive X-Ray Spectroscopy
EA……...Elemental Analysis
SAED……Selected Area Electron Diffraction
GC-MS.....Gas Chromatography Mass Spectrometry
NMR.....Nuclear Magnetic Resonance Spectroscopy
CCD.....Charged Coupled Device
EELS.....Energy-Loss Spectroscopy

Physical and Mathematical Symbols

d.....perpendicular spacing
θ .....angle of incidence (Bragg angle)
λ.....wavelength
n .....integer

Δx.....min detectable distance
λ.....wavelength of the electromagnetic radiation
n…….....refractive index of the medium
α.....angle of the incident beam with the objective
h.....Planck's constant
m.....rest mass of the particle, m_e=9.109x10^{-31}kg
v.....velocity of the particle
e.....charge on electron=1.602x10^{-19}C
U.....acceleration voltage

s.....period
f.....focal length
λ.....wavelength of light in the specimen plane
Φ.....angle between the lens axis and the diffracted wave

$\psi(x, y)$.....transmitted wave function
θ .....scattering angle
$\psi(u)$.....Fourier transform of the wave ψ(r)
C_s.....spherical abberation coefficient
Δf.....lens defocus
λ.....electron wavelength
⊗.....convolution calculation of (x, y), $t_{obj}(x,y)$ is the inverse Fourier transform of the phase function $exp[i\chi(u)]$
GoF.....goodness-of-fit indicator
R_{wp}……weighted residual error

Chemicals and Materials

3PhM.....triphenylmethane
p-Xyl.....p-xylene
EthBenz.....ethylbenzene
DiPhEth.....diphenylether

List of Publications

Metal Oxide Nanocrystals: Building Blocks for Mesosturctures and Precursors for Metal Nitrides; M. Niederberger, J. Buha, I. Djerdj, MRS Proceeding, Spring Meeting 2007

Thermal Transformation of Metal Oxide Nanoparticles into Nanocrystalline Metal Nitrides Using Cyanamide and Urea as Nitrogen Source; J. Buha, I. Djerdj, M. Antonietti, M. Niederberger; Chem. Mater., 2007, 19, 3499

Nonaqueous synthesis of nanocrystalline indium oxide and zinc oxide in the oxygen-free solvent acetonitrile; J. Buha, I. Djerdj, M. Niederberger; Cryst. Growth Des., 2007, 7, 113

Nonaqueous synthesis of metal oxide nanoparticles: Review and indium oxide as case study for the dependence of particle morphology on precursors and solvents; M. Niederberger, G. Garnweitner, J. Buha, J. Polleux, J. Ba, N. Pinna; J. Sol-Gel Sci. Tech., 2005, 40, 259

Acknowledgments

First of all, I would like to thank to Prof. Dr. Markus Antonietti, for giving me an opportunity to do my PhD at one of the most prestigious institutes not only in Germany but worldwide. Thank You for believing in me since the very beginning.

Second of all, I would like to thank to my supervisor, Prof. Dr. Markus Niederberger, for directing my daily work, teaching me many things, correcting the thesis, for numerous both scientific and non-scientific discussions, for his kindness and keeping promises, for the long phone calls, for making me believe that there are still some real scientists being able to accomplish so many things simultaneously, for hosting me in Switzerland... Thank You for being what you are no mater where and on which position. Thank you for believing in me till the very end!

Dr. Baishakhi Mazumder is gratefully acknowledged for performing experiments under NH_3 flow, and for further eventual collaboration in this direction.

Further on I would like to thank to Dr. Hartmann for giving me the “TEM driving license” and to all the technicians that have been more then helpful during my everyday work. Here, special thanks goes to Regina Rothe for making our lab organized no mater what, Ingrid Zenke for being so patient with us - “XRD maniacs”, Rona Pitschke for showing me all the tricks in the TEM lab and Sylvia Pirok for so many elemental analysis measurements.

Completely differently I would like to thank to my friends and colleges who made my life in Berlin interesting not only at the institute. I hope we will keep in touch! One big thanks goes for: Magda for immense support, Jong not only for the corrections; Farnoosh, Pantea, Zofia, Mattijs, Miles, Michael, Laem and Saroj for the great time in our coffee corner with Ovca’s adventures; ein grosses *Dankeshcoen* geht an: Philipp, Helena, Nicole, Julia, Denis, Jens H., Jens W., Andreas, Kirstin, Munish, Silke, Georg, Evgenia, Olessia, Esther, Kiril, Julia, Johan; *Merci*: Sebastien, Pierre, Erwan, Philippe, Frederic, Cecile, Audree; *Grazie*: Antonio, Davide & Palmira, Marco, Simone; *Gracias*: Elena, Pedro, Ruben; *Tesekkur ederim*: Ozlem, Rezan, Mehmed, Emre, Engin; special *Obrigada* to my portugese gang: Ana S., Ana T., Ana Q., Ana

G., Manuel….. and special *Hvala* to my ex-yu gang here in Berlin: *mojoj šacilajn Dani, preduzimaču Dači, dragom Zverku, dedi Milanu, mojim hercegovkama Tanji i Ljerki, carici Leoni, kralju Igoru i mnogim mnogim drugima.....*
While living abroad I learned to value independence. I came to appreciate the courage needed in order to travel alone through unknown cities. I also grew to respect the determination necessary in order to emerge from the journey tempered, independent, and emotionally mature. This time that I have spent abroad has shaped my ideas in many ways. I have learned to cherish courage, independence, and intellectual freedom, reaching the level of more experienced and thoughtful person.

For the speical time, long skype talks and neverending support in the last 2 years one big *hvala* to my boyfriend and my best friend Srdjan. *Nadam se da će konačno doći kraj našoj vezi na daljinu...*

The most special thanks goes to my family for being there for me, and for the biggest support in bad and good times during this period. *Dragi mama, tata i seko, hvala vam povrh svega što nikada niste prestali da verujete u mene! Svesnost da sam vaša činila me je najjačom kada sam bila najslabija!*

Još jedno hvala svima onima koje nisam pomenula, a koji su mi bili krma pri najjačim burama.